3D Magnetic Resonance Microscopy of Dehydrated Biological Specimens

Dissertation

zur Erlangung des Grades

des Doktors der Naturwissenschaften

der Naturwissenschaftlich-Technischen Fakultät II

– Physik und Mechatronik –

der Universität des Saarlandes

vorgelegt

von

Daniel Mietchen

Saarbrücken

2006

Fraunhofer Institute for Biomedical Engineering
– Magnetic Resonance Group –
and
University of the Saarland
– Faculty of Physics and Mechatronics –

3D Magnetic Resonance Microscopy of Dehydrated Biological Specimens

Daniel Mietchen
Thesis submitted for the degree of Doctor rerum naturalium
Supervisor: Prof. Dr. Günter R. Fuhr
© 2006

Declaration

I hereby declare that this thesis is the result of my own independent investigation and that all contributions from other sources are duely acknowledged. No part of this thesis was previously submitted for a degree at this or any other university. I agree that the Library may lend or copy the thesis upon request.

Hiermit versichere ich an Eides statt, dass ich die vorliegende Arbeit selbständig und ohne Benutzung anderer als der angegebenen Hilfsmittel angefertigt habe. Die aus anderen Quellen oder indirekt übernommenen Daten und Konzepte sind unter Angabe der Quelle gekennzeichnet.

Die Arbeit wurde bisher weder im In- noch im Ausland in gleicher oder ähnlicher Form in einem Verfahren zur Erlangung eines akademischen Grades vorgelegt.

Ich erkläre mich einverstanden, dass die Bibliothek diese Arbeit auf Nachfrage verleihen und kopieren darf.

Daniel Mietchen

Saarbrücken, 22nd February 2006

Abstract

Objectives   The major theme of this thesis is the evaluation of the potential of Magnetic Resonance Microscopy (MRM) for branches of the life sciences that have previously seen few or no applications of this non-invasive methodology, particularly for cell biology, palaeontology and cryobiotechnology. An emphasis will be put on the role of liquid water whose multiple biological functions – as a solvent, structural element and metabolite – render it essential for life as we know it.

Background   Dehydration beyond a critical threshold poses a serious threat to most organisms in their active state, and mechanisms helping to cope with draught stress present an evolutionary advantage in environments lacking permanent access to liquid water. From a biotechnological point of view, mastering the reversible transition between hydrated and dehydrated states of biological material would allow their long-term storage and facilitate a continuous supply, especially in cases where cell and tissue culture are impossible or not desirable. One of the ways to achieve this is cryopreservation, an arsenal of methods designed to store biological materials for long terms at biologically low temperatures to minimise degradation. In recent years, a trend has developed towards freezing of small cell clusters or even single cells, as opposed to large chunks of tissue. This creates an increased demand for miniaturised cryopreservation systems, and the reduced amount of material raises the need for high-resolution non-invasive supervision of the cryoprocessing.

Method   Magnetic Resonance (MR) techniques have become famous precisely for their non-invasiveness and their sensitivity to liquid water, yet microscopic MR applications to dehydrated samples have been scarce, mainly because (i) the signal-to-noise ratio decreases upon dehydration – even dramatically so upon freezing – and (ii) high spatial resolutions translate into a considerable reduction of the already low signal intensity. The primary goals of this study were, therefore, to determine whether these two major barriers can be overcome individually as well as in combination and to evaluate whether the strong magnetic fields necessary for such experiments could interfer with cellular physiology.

Results   Microscopic MR image series allowed the non-invasive assessment of the morphology within a well-hydrated cell biological model system (oocytes and embryos of the frog *Xenopus laevis*), in extreme examples of long-term preservation and dehydration (fossil remains of invertebrate, vertebrate and plant species) and in cryobiological samples ranging from tumor cell spheroids to larvae of cold-hardy insects. Cell division and embryogenesis could be observed in MRM images of *Xenopus* embryos, and spatially localised MR spectra from subcellular compartments delivered biochemical information about *Xenopus* oocytes in their normal state and upon uptake of an externally applied drug. A previously described apparent magnetic field effect on *Xenopus* embryos could be shown not to depend on the magnetic field, as opposed to a new effect found in oocytes artificially deprived of their jelly coat. MRM data allowed the diagnosis of pathological alterations in fossils and the monitoring of cryoprotectant effects in frozen or supercooled insects.

Conclusions   These experiments demonstrate that, from a technical perspective, MRM indeed has the potential to become a tool for cell biology, palaeontology as well as cryo-biotechnology and that side effects of the methodology, though detectable under unphysiological conditions, do not prevent that.

Zusammenfassung

Zielsetzung Hauptthema dieser Dissertation ist die Auslotung der Analysemöglich-keiten, welche die Magnetresonanzmikroskopie (MRM) in Bereichen der Lebenswis-senschaften bietet, die bisher keine oder wenige Anwendungen dieser nicht-invasiven Methodik erfahren haben, insbesondere Zellbiologie, Paläontologie und Kryobiotechno-logie. Ein Schwerpunkt wird auf die Rolle flüssigen Wassers gelegt, das aufgrund seiner vielfältigen biologischen Funktionen – als Lösungsmittel, Struktur- und Stoffwechselele-ment – eine der wichtigsten Grundvoraussetzungen für Leben darstellt.

Hintergrund Dehydrierung über ein bestimmtes Maß hinaus birgt für die aktiven Sta-dien der meisten Organismen eine ernste Gefahr. Demzufolge stellen Mechanismen zur Bewältigung von Wassermangel einen deutlichen evolutionären Vorteil in einer Umge-bung dar, wo permanenter Zugang zu flüssigem Wasser fehlt. Aus biotechnologischer Sicht ist die Beherrschung eines reversiblen Überganges biologischer Materialien vom hy-drierten in den dehydrierten Zustand von Interesse, würde dies doch deren Langzeitaufbe-wahrung und eine prinzipiell permanente Verfügbarkeit ermöglichen, besonders in Fällen, in denen Zell- und Gewebekultur unmöglich oder nicht erwünscht sind. Dieses Ziel kann auf unterschiedlichen Wegen erreicht werden. Einer davon ist die Kryokonservierung – ein Arsenal von Methoden, welche darauf abzielen, biologisches Material langfristig bei biologisch tiefen Temperaturen zu lagern, wodurch Stoffwechselprozesse sehr stark ver-langsamt werden oder ganz zum Erliegen kommen. Gegenwärtig gibt es einen Trend weg vom Einfrieren großer Gewebestücke und hin zu kleinen Zellhaufen oder sogar einzelnen Zellen. Damit einher geht eine zunehmende Nachfrage nach miniaturisierten Kryokonser-vierungssystemen, und der verringerte Umfang einzelner Gefrierproben verlangt zudem nach einer hochauflösenden und zunehmend nicht-invasiven Überwachung der Kryopro-zessierung.

Methode Kernspin- bzw. Magnetresonanztechniken (MR) verdanken ihre Popularität vor allem ihrer nicht-invasiven Natur und ihrer Empfindlichkeit gegenüber flüssigem Wasser, jedoch blieben mikroskopische Anwendungen dieser Technik an dehydrierten Proben bisher rar. Die Hauptgründe dafür sind, dass (i) das Signal-Rausch-Verhältnis mit der Dehydrierung abnimmt – beim Gefrieren sogar dramatisch – und (ii) die geforderte hohe räumliche Auflösung eine beträchtlichen Verringerung der ohnehin geringen Signalintensität bedeutet. Das erste Ziel der vorliegenden Studie war daher festzustellen, ob diese zwei grundlegenden Hindernisse zunächst einzeln, aber auch in Kombination überwunden werden können und abzuschätzen, inwiefern die starken magnetischen Felder, die für solche Experimente nötig sind, die zelluläre Physiologie beeinflussen könnten.

Ergebnisse Anhand mikroskopischer MR-Bildreihen konnte die interne Morphologie eines wasserreichen zell- und entwicklungsbiologischen Modellsystems (Oozyten und Embryos des Frosches *Xenopus laevis*) nicht-invasiv bestimmt werden. Dies gelang ebenso in extrem langzeitkonservierten wasserarmen Proben (Fossilien von Wirbellosen, Wirbeltieren und Pflanzen) wie in kryobiologischen Systemen, die von Tumorzell-Sphäroiden bis zu Larven kälteresistenter Insekten reichten. Zellteilung und Embryogenese konnten mit MRM-Bildserien sich entwickelnder *Xenopus*-Embryonen verfolgt werden, und ortsspezifische MR-Spektren von subzellulären Kompartimenten lieferten biochemische Informationen über *Xenopus*-Oozyten unter physiologischen Bedingungen sowie nach Verabreichung einer pharmakologischen Testsubstanz. Darüberhinaus konnte gezeigt werden, dass ein zuvor beschriebener scheinbarer Magnetfeldeffekt auf *Xenopus*-Embryonen ganz unabhängig vom Magnetfeld auftritt und vielmehr auf die künstliche Entfernung der Gallerthülle, welche Amphibien-Eier umgibt, zurückzuführen ist, während in unbefruchteten Eizellen – ohne Gallerthülle – tatsächlich eine magnetfeldinduzierte Pigmentverschiebung beobachtet werden kann. Des Weiteren lieferten MRM-Daten pathologische Befunde aus dem Inneren intakter Fossilien und umfassende Einsichten in Gefrierschutzmechanismen gefrorener sowie unterkühlter Insektenlarven.

Schlussfolgerungen Diese Experimente zeigen, dass MRM vielfältig als analytische, diagnostische oder Prozesskontrolltechnik in Zellbiologie, Paläontologie und Kryobiotechnologie angewendet werden kann und dass nachweisbare, jedoch nur unter nichtphysiologischen Bedingungen auftretende methodenbedingte Nebenwirkungen dem nicht im Wege stehen.

Acknowledgements

This thesis has greatly benefited from the experience, patience and scholarliness of several individuals and of some groups of people: First and foremostly, I would like to thank Prof. Günter Fuhr and PD Dr. Frank Volke for hosting me in the Magnetic Resonance Department at the Fraunhofer Institute for Biomedical Engineering (IBMT) in St. Ingbert and for providing a continuous flow of motivation, inspiration and criticism in numerous discussions on the subjects of my thesis and way beyond. I also thank Prof. Manfred Lücke (Saarbrücken) for encourageing me to embark on this endeavour and Prof. Jürgen Hüttermann (Homburg) for helping me to home in on it.

Furthermore, I wish to bow in front of my colleagues at the Korea Basic Science Institute (KBSI) in Daejeon, namely Prof. Chaejoon Cheong and Dr. Seung-Cheol Lee under whose guidance I started to explore $\vec{k}$-space and who tuned my senses to the peculiarities of microscopic MR. For most of the remaining time, Dr. Bertram Manz (at IBMT) helped me tremendously to fill the gaps in my MR knowledge systematically with a consistent structure. Besides the help of members of the Magnetic Resonance Teams at IBMT and KBSI, I have profited in multiple ways from support by the cryobiophysics, biohybrids and laser systems groups at IBMT, most notably by Dr. Alisa Katsen-Globa and Friederike Ehrhart who provided me with cryosamples.

My thanks extend to Jörg Jakobi (Gießen) and to Prof. Hans-Peter Richter (Homburg) who teamed up with me to investigate the cellular magnetic field effects. I thank Prof. Helmut Keupp, Prof. Martin Aberhan, PD Dr. Oliver Hampe, Dr. Barbara Mohr, Dr. Christian Neumann (all in Berlin) as well as Dr. Eva-Maria Geigl (Paris), Dr. Yolanda Fernández-Jalvo (Madrid), Virginia Correia (Madrid and Paris), Prof. Andrew H. Knoll (Boston), Prof. Pierre Albrecht and Dr. Armelle Charrié (both in Strasbourg) for exciting discussions about the molecular aspects of fossils and evolution. I am also grateful to Prof. Thomas Koop (Bielefeld) for valuable insights into ice nucleation and to Dr. Stefan Hetz (Berlin), Dr. Brent Sinclair (Las Vegas) and Prof. Kenneth Storey (Ottawa) for sharing with me their expertise on insect physiology and cold hardiness.

Finally, I happily thank my friends, flat mates, band members and family who provided me with the environment to enjoy my research without forgetting the world beyond it.

Contents

List of Abbreviations

abbr.	expanded abbreviation	remark
CT	Computed Tomography	
DMEM	Dulbecco/Vogt's Modified Eagle's Medium . . .	used for cell culture
DMSO	Dimethylsulfoxide [$(CH_3)_2SO$]	cryoprotectant
FCS	Foetal calf serum	used for cell culture
Fig.	figure	*plural:* Figs.
FT	Fourier transform	
GE	gradient echo	MR pulse sequence
HEPES	4-2-hydroxyethyl-1-piperazineethanesulfonic acid	buffer solution
hpf	hours post fertilisation	
IBMT	Fraunhofer Institute for Biomedical Engineering	host for most of this thesis
IR	infrared	
KBSI	Korea Basic Science Institute	host for part of this thesis
MAS	Magic Angle Spinning	solid-state MRS technique
MBM	Modified Barth's Medium	for frog oocyte cultivation
MR	Magnetic Resonance	as in "MR techniques"
MRI	Magnetic Resonance Imaging	
MRM	Magnetic Resonance Microscopy	
MRS	Magnetic Resonance Spectroscopy	
MSME	Multi-slice multi-echo	MR pulse sequence
NMR	Nuclear Magnetic Resonance	
PRESS	Point-Resolved Spectroscopy	MR pulse sequence
RARE	Rapid Acquisition and Relaxation Enhancement	MR pulse sequence
RPMI	Roswell Park Memorial Institue Medium	used for cell culture
SE	spin echo	MR pulse sequence
rf	radio frequency	
SNR	signal-to-noise ratio	
TAG	triacylglycerol	
TBE	Tennis Ball Effect	in dejellied eggs
TMS	Tetramethylsilane [$Si(CH_3)_4$]	MRS reference substance

List of Figures

List of Tables

Chapter 1. Introduction

Water in its liquid state defines the chemical environment of life, at least on our planet, and although many organisms are capable of long-term survival in dehydrated states, none is known to spot a life cycle entirely devoid of liquid water. Consequently, water phase transitions define not only the temperature scales used by many human populations but also some of the most fundamental boundary conditions for life in general (Keilin, 1959; Wettlaufer, 1999; Ball, 2000; Bada, 2004).

There is more to life than water, and properties of other molecular species contribute significantly to the fine-tuning characteristic of animated matter (for an overview, see Lodish et al., 2000): Cellular membranes throughout the kingdoms of life consist of a complex mixture of lipids with overlapping melting points, proteins form three-dimensional structural networks that determine the shape and catalytic activity of cells and tissues, while ribonucleic acids store the information and sugars the energy necessary to control and execute all these processes.

Closer inspection of this simplified picture quickly reveals that proteins also contribute to the structure of membranes, ribonucleic acids to the metabolic activity, and sugars to the structure of proteins. If investigated on the molecular level, the apparent complexity of these interactions rises even further but their limits, ultimately, are always defined by the properties of the neighbouring water molecules.

This equally applies to the methods used in biomedical investigations: Water or aqueous solutions provide their main anchor, and water phase transitions often determine their limits of applicability. Magnetic Resonance (MR) techniques are not an exemption to this rule of thumb but they come in variants which together allow to investigate liquid, solid and intermediate states of organic and inorganic matter. This versatility and their non-invasiveness render them very appealing for applications to samples that are to be conserved over long time spans – be it in traditional museums or in cryobanks, arguably the museums of the future.

1.1. Dehydration in biology

Dehydration is a common label for all processes involving the loss of water from a given system. Throughout this thesis, more specifically, dehydration is to be understood as a loss of *liquid* water by any means. Phase transitions – namely evaporation, freezing and sublimation – represent one class of such mechanisms but osmotic, metabolic and other processes frequently contribute to dehydration in biological specimens.

Dehydration can be reversible if the loss of water can, at the cellular level, be compensated such that vital structures do not experience serious damage, and it can easily be irreversible and thus lethal if this challenging precondition is not met. Therefore, habitats with rare incidences of liquid water exert evolutionary pressures on species to develop mechanisms that can cope with the water loss such that rehydration allows the return to a vital state.

Examples of such habitats include, of course, the deserts but also polar, high-altitude and hypersaline environments as well as beaches, moss and other microhabitats (for reviews, see Keilin, 1959; Crowe et al., 1992; Potts, 1999; Alpert, 2000; Clegg, 2001; Storey and Storey, 2004b). Amber, too, was proposed as such an environment (Cano and Borucki, 1995) but the evidence so far remains disputed (Fischman, 1995; Priest, 1995; Beckenbach, 1995; Cano, 1995) and can not easily be reproduced, since fossil samples are unique in many aspects. The uniqueness issue could be coped with if non-invasive methods were available, and since fossils represent an extreme state of dehydration of organic matter, Chapter 4 has been devoted to their study. The focus of this thesis, however, is on living specimens, on keeping them alive and on investigating them non-invasively.

The adaptations an organism has to undergo in order to survive water loss are manyfold but can be summarised as follows: The structural and metabolic functions of water in cellular and extracellular biochemistry – especially with respect to macromolecules – have either to be taken over by other molecules still available or readily synthesisable and somewhat similar to water, or they have to be downregulated in a very controlled way (Crowe et al., 1998; Clegg, 2001; Feofilova, 2003). Candidate molecules for water replacement in the stabilisation of macromolecular structure include, most prominently, other molecular species with high proportions of hydroxy groups, such as polyalcohols and sugars, and perhaps proteins such as chaperones. Metabolic replacement of water, though, is difficult and generally circumvented by shutting down the metabolism to a minimum.

Once a low-water state – commonly termed anhydrobiosis, which represents one aspect of cryptobiosis, the temporary cessation of observable signs of life – is achieved, further details of the stress the organism is subjected to essentially loose their importance

(Hinton, 1968; Clegg, 2001): Although specialisations for specific stressants can be observed, many species capable of anhydrobiosis can not only endure water loss but also tolerate heat and cold, elevated levels of salinity, radiation or the deprivation of food or oxygen to an extent that can not be explained with adaptations to their natural habitat. An extreme example for this is the larva of the fly *Polypedilum vanderplanki* which normally lives in shallow water pools in East African arid environments but can revive and undergo normal metamorphosis after several minutes of immersion in liquid Helium (i.e. at a temperature of 3 K, or -270°C, Hinton, 1960).

At 3 K, the activation energy for chemical reactions is much higher than thermal noise, and so whatever remained of a cellular metabolism comes to a complete rest. This condition, however, still holds true at higher temperatures, and for the melting temperature of the cheaper Nitrogen (77 K, or -196°C), it has been estimated that a given chemical reaction would (if at all sterically possible in the solidified state 56 K below the glass transition temperature) proceed at a rate about seven orders of magnitude slower than at room temperature (293 K, or 20°C Keilin, 1959). Consequently, low temperature regimes provide an interesting option for the long-term storage of biological material with minimum decay, as long as the viability can be kept, and cryopreservation thus represents the focus of the *in vivo* part of this thesis.

Since this is generally not as easily achieved as with *Polypedilum*, much research effort has been placed in elucidating the mechanisms that contribute to cold tolerance and could hence find cryobiotechnological applications. One such mechanism is the avoidance of ice nucleation (reviewed in Zachariassen and Kristiansen, 2000; Koop, 2004): Water, like many liquids, can be supercooled below its melting point, and ice crystals only form around so-called nuclei whose molecular structure is closed to that of ice. In the absence of such nuclei, water remains liquid until the reduced thermal energy upon cooling restricts the motion of water molecules that much that they aggregate even closer and eventually form clusters that act as a nucleus and initiate crystallisation. The number of molecules required for such a nucleus composed entirely of water molecules decreases strongly with temperature and is about $4.5 \cdot 10^4$ at -5°C and about 70 at -40°C. At around -42°C (under atmospheric pressure), only two molecules are sufficient to initiate nucleation, and the liquid phase can not persist any further.

In nature, supercooled water is rare, as ice nucleators are generally present or randomly generated by agitation of the water reservoir but water drops in clouds provide such a rare example (Sassen et al., 1985) and have have indeed been found to be populated by bacteria for which the nucleated state, however, provides an advantage in terms of dispersal, and so they rather initiate ice nucleation than avoiding it (Sattler et al., 2001). Other organisms actively create favourable conditions for supercooling, namely by synthesising the

above-mentioned cryoprotective polyols or sugars that can replace water molecules, or with proteins dedicated to bind potential ice nucleators, while still others allow extracellular freezing and use a mixture of cryoprotectant synthesis, ice nucleation and (extracellular) ice binding proteins to avoid cellular damage by the extracellular ice (reviewed in Storey and Storey, 2004a). Finally, recent evidence suggests that controlled *i*ntracellular ice formation might also be a cryoprotective mechanism (Acker and McGann, 2003).

Cold hardyness has been found in a broad distribution of taxa ranging from prokaryotes to plants to nematodes to insects to fish but it also occasionally occures in amphibians or reptiles (for an overview, see Storey and Storey, 2004a). A general trend exists for cold tolerance strategies to correlate with habitat – across taxa – but this is not mandatory, as examplified by the freeze-avoiding gall moth *Epiblema scudderiana* and the freeze-tolerant gall fly *Eurosta solidaginis* whose larvae both overwinter in the same habitat – in plant stems of the goldenrod genus *Solidago* (Storey and Storey, 2004a).

While the residual metabolic activity in supercooled water obviously is an advantage for organisms striving to avoid cold-induced damage, it is not desirable for cryopreservation, as it does not prevent cellular ageing and decay. Therefore, other strategies have to be explored, and these mainly include vitrification techniques where the sample is cooled such that a glassy phase is reached in which the lack of crystal structures avoids lethal damage to the cell membrane. Here, the polyhydroxylic disaccharid trehalose has received particular attention, as its high glass transition temperature of 383 K (110°C) is above the upper limit for the vast majority of active life forms which could thus, at least in principle, readily be vitrified if sufficient trehalose could be provided (Crowe et al., 1998).

In view of potential biomedical applications of such vitrification strategies, model systems have to be developed that allow to estimate the cryobiological characteristics of biomedical cell and tissue samples. Tumor spheroids fit these criteria, as their three-dimensional growth patterns provide a more realistic proxy for *in vivo* tissue growth than do conventional two-dimensional culture techniques (Mueller-Klieser, 1997; Nelson et al., 2005).

Visualisation of three-dimensional culture and cryopreservation conditions, in turn, requires equally three-dimensional techniques. For cellular applications, optical methods have long been the modality of choice (e.g. Huisken et al., 2004) but due to the opaqueness of crystal and even glassy ice, their use is limited to observations of the liquid phase. Similarly, ultrasound does not penetrate well into ice (cf. Gilbert et al., 1997), and x-ray techniques (Larabell and Le Gros, 2004) cause cell damage, the avoidance of which is at the core of any cryopreservation endeavour.

A solution to part of these problems could be provided by Magnetic Resonance (MR) microscopic imaging techniques. They can deliver three-dimensional representations of a sample non-invasively and have previously demonstrated their potential for the investigation of de- and re-hydration processes in systems as diverse as sea ice (Eicken et al., 2000), rocks (Borgia et al., 2000), and desiccation tolerant plants (Manz et al., 2003).

However, cellular properties can not yet readily be investigated with MR Microscopy (MRM). Therefore, the limits of MRM for cellular applications will be tested in Chapter 2. As high-resolution MRM exposes the samples to strong static magnetic fields, their effect on cellular physiology will be studied in Chapter 3 before the combined insights from these two *in vivo* chapters and from the *in saxo* (i.e. in stone) investigations of Chapter 4 will be applied *in glacie* (i.e. in ice) in Chapter 5. For better visualisation of the results, ten of the image slices presented here will be supplemented by movies that either illustrate the temporal evolution of the sample (cf. Chapter 2) or its three-dimensional morphology (Chapters 4 and 5). The movies are numbered identical to the figures they belong to, and their existence will be indicated by the sign Ⓜ both in the figure legend and in the list of figures.

Some parts of this thesis describe findings that entered manuscripts in preparation or currently under review or that have already been published, as detailed in Appendix A.

1.2. Magnetic Resonance Microscopy (MRM)

In short, magnetic resonance is the absorption of electromagnetic energy by a subpopulation of atomic nuclei in an external static magnetic field when irradiated at an isotopespecific resonance frequency directly proportional to the local magnetic field strength. When the absorbed energy is released upon return to the thermal equilibrium, an inductive signal can be observed which contains chemical and – under special conditions – spatial information about the molecular composition of the irradiated sample. The concept has repeatedly found comprehensive treatment elsewhere – see, e.g., Abragam (1961) or Slichter (1978) for spectroscopy and Callaghan (1991) or Blümich and Kuhn (1992) for imaging – and will therefore only briefly be sketched here.

Atoms exposed to an external magnetic field B_0 experience a Zeeman splitting of their energy levels such that the magnetic quantum number m can take on all integer values between $+I$ and $-I$, the extremal values of the spin quantum number I, provided that $I \neq 0$. The latter condition is not fulfilled by atoms with even numbers of both protons and neutrons because the individual spins of identical nucleons cancel out. For the nucleus most commonly employed in MR studies and also in this thesis, ^{1}H, $I = 1/2$.

The Zeeman energy difference $\Delta E = E_i - E_j$ between adjacent ($\Delta m = 1$) energy levels E_i and E_j (with $E_i < E_j$) can then be expressed as

$$\Delta E = -\frac{h}{2\pi}\gamma B_0 \,, \qquad (1.1)$$

where γ is the gyromagnetic constant of the isotope ($2.67522 \cdot 10^8$ s^{-1} T^{-1} for ^{1}H), and $h = 6.62607 \cdot 10^{-34}$ J s the Planck constant.

The equilibrium populations of both energy states follow a Maxwell-Boltzmann distribution:

$$N_i/N_j = e^{-\Delta E/kT} \,, \qquad (1.2)$$

with $N_{i,j}$ representing the number of nuclear spins in state i or j with the respective energy level, $k = 1.38065 \cdot 10^{-23}$ J/K the Boltzmann constant and T the temperature. For ^{1}H in a magnetic field of 9.4 T and a temperature of 300 K, this translates into a population difference $\Delta N = N_i - N_j$ of about three spins out of one million, which severely restricts the sensitivity of the method.

As a consequence of the population difference, a net magnetisation M_0 can be observed along the axis (usually named z) of the static field B_0. The equilibrium distribution can be disturbed by supplying $\Delta E = h\nu_0$ via radiofrequency (rf) pulses oscillating at a frequency ν_0 around an axis perpendicular to z, which creates an additional magnetic field B_1. With equ. (1.1), the resonance condition for the absorption of this pulse is given by the Larmor

relation

$$\omega_0 = 2\pi\nu_0 = -\gamma B_0 \qquad (1.3)$$

between the angular frequency ω_0 of the rf pulse and the local magnetic field. Such a rf pulse will stimulate transitions from the lower to the higher energy state (as long as $\Delta N > 0$), thereby flipping the net magnetisation in the sample by the flip angle

$$\theta = \gamma B_1 t_{flip} \,, \qquad (1.4)$$

where t_{flip} is the pulse duration.

When the spins relax by releasing the absorbed energy, a so-called free induction decay (or FID) induces a signal S in a receiver coil. For the typical case of a spin echo pulse sequence (two pulses corresponding to flip angles of $\pi/2$ and π, separated by an echo time T_E), the generated signal $S(t)$ is of the form:

$$S(t) = C\,\rho\,\left(1 - e^{T_R/T_1}\right)\,e^{-T_E/T_2} \,, \qquad (1.5)$$

where C is a constant for a given sample, while ρ represents the spin density in the sample, T_R the repetition time (i.e. the intervall between the onset of two consecutive rf pulse sequences), T_1 the longitudinal relaxation time (i.e. the time constant of the magnetisation decay perpendicular to the static magnetic field, also known as spin-lattice relaxation time), T_E the echo time (i.e. the time between the onset of rf pulsing and the beginning of signal acquisition) and T_2 the transverse relaxation time (i.e. the time constant of the magnetisation decay perpendicular to the static magnetic field, also known as spin-spin relaxation time). It should be noted that the refocusing function of the second pulse at $\theta = \pi$ can alternatively be fulfilled by the administration of appropriate field gradients. Such schemes are known as gradient-echo sequences which show the same signal decay as described by equ. 1.5, except that T_2 has to be replaced by the apparent relaxation time T_2^* which is shorter than T_2, as the loss of transverse magnetisation in gradient-echo sequences arises not only from the microscopic spin-spin interactions causing T_2 decay but also from macroscopic magnetic field inhomogeneities.

Fourier transformation of the time domain signal described by 1.5 generates a spectrum in the frequency domain where the position, form and ratio of the peaks give information about the molecular composition of the sample in terms of the employed isotope. This is the basis of MR spectroscopy (MRS).

Typically, at least in the life sciences, MRS is performed in aqueous samples but methods have also been developed to investigate solids. Such a variant is called Magic Angle Spinning (MAS) because the sample is quickly spun around an axis inclined to the static magnetic field by the "magic angle" (about 54.7°) where spatial magnetic dipolar interactions between spin pairs are effectively averaged out (Andrew, 1981).

A further implication of equ. (1.3) is that the magnetic field can be modulated in time and space by manipulating radiofrequency pulses such that they create space-dependent magnetic field gradients $\vec{G}(\vec{r})$ supplementary to the static magnetic field:

$$\vec{G}(\vec{r}) = \left(\frac{\partial B_z}{\partial x}, \frac{\partial B_z}{\partial y}, \frac{\partial B_z}{\partial z} \right). \tag{1.6}$$

In practice, this is achieved by employing a dedicated spatial arrangement of gradient coils that send gradient pulses each time an rf pulse sequence is applied. If the time that the gradient remains on is varied between consecutive rf pulses but its amplitude is kept constant, this regime is referred to as frequency encoding. Conversely, phase encoding depicts the concept of varying the gradient amplitudes and keeping them on for a constant period.

To account for such variations of the field, the Larmor condition (cf. equ. 1.3) has to be modified accordingly:

$$\omega_0(\vec{r}) = -\gamma \left[|\vec{B_0}| + \vec{G}(\vec{r}) \cdot \vec{r} \right]. \tag{1.7}$$

The combined application of several gradients (typically one with frequency encoding and two with phase encoding) then allows to define virtual slices and volume elements (voxels) whose serial concatenation results in a three-dimensional representation of the sample under investigation This is the basis of MR imaging. As equ. (1.5) now generally applies to each voxel individually (details depend on the exact pulse sequence employed), spatial maps reflecting the spin density or the relaxation constants T_1 and T_2 can be constructed, and the loss of labeled spins from a given voxel during the time interval between the excitation pulse and signal acquisition can serve to create maps where each image element reflects the diffusion, flow or derived parameters such as the shear rate in the corresponding volume element.

Since it is inconvenient and time-consuming to acquire a set of gradient-dependent signals for many individual frequencies, a Fourier technique is commonly employed that transforms real space into a virtual matrix. This so-called $\vec{k}$-space can be defined in terms of the MR gradients employed:

$$\vec{k} = -\frac{\gamma}{2\pi} \int_0^{t_{\mathrm{on}}} \vec{G}(t)\,\mathrm{d}t \tag{1.8}$$

$$= -\frac{\gamma}{2\pi} \vec{G} \cdot t_{\mathrm{on}}. \tag{1.9}$$

Here, t_{on} represents the period during which the respective gradient is on. The dimension of $\vec{k}$-space is $N_R \times N_P$, where N_R and N_P are the number of points acquired in Read direction (i.e. the direction in which frequency encoding is used) and Phase direction (i.e. the phase-encoded direction), respectively.

The distance Δk of two points in $\vec{k}$-space defines the field of view (FOV) that the MR image covers in real space:

$$\text{FOV} = \frac{1}{\Delta k}, \tag{1.10}$$

from where the spatial resolution $\Delta \vec{r}$ of a MR image – equal to the unit size of individual volume elements (also known as voxels) – can be defined as

$$\Delta \vec{r} = \frac{\text{FOV}}{dim(\vec{k})}, \tag{1.11}$$

with $dim(\vec{k})$ representing the number of real points (the frequency-encoded signal is complex) acquired in the respective dimension of $\vec{k}$-space (e.g. $N_R/2$ and N_P). In the experimental chapters, $dim(\vec{k})$ will be expressed in terms of the matrix size (MTX), i.e. the number of pixels in the individual directions (e.g. $128{\times}128{\times}256$).

Note that the philosophy behind this MR definition of spatial resolution differs fundamentally from the one behind its counterparts in optical or electron microscopy, and it can be adjusted independently for each direction. Microscopic resolution in MR could thus also be defined in terms of FOV and $dim(\vec{k})$ but here, MR terminology follows the common convention that microscopic resolution means the ability to distinguish structures equal to or smaller than the optical resolution of the human eye (i.e. about $100~\mu$m).

Contrast in MR images can in principle be generated with any of the spectroscopic contrast parameters and additionally with spin density, diffusion or flow, depending on the application. Chemical information contained in peaks of an MR spectrum, for instance, can be incorporated into an MR image by selectively exciting the frequencies covered by these peaks. This can be achieved, for instance, by modulating the broad excitation pulse with a narrow sinc function ($\text{sinc}(x) = sin(x)/x$) whose Fourier transform is a good approximation of a rectangle, resulting in a rectangular window being selected in the corresponding spectrum. Similarly, selected frequency bands can be suppressed during MR signal acquisition by using sinc pulses and deliberately spoiling gradient pulses. In particular, the suppression of the water signal within a sample thus represents a possibility to mimic dehydration in hydrated samples.

It should be noted that chemical and spatial information can not only be combined in MR images but also in MR spectra. This method is known as localised MRS and typically uses just one voxel (thereby avoiding the loss of spectral information due to signal distribution in $\vec{k}$-space) whose position can otherwise be defined as for single voxels within MR images of a larger matrix size.

The signal-to-noise ratio (SNR) of an MR experiment shows – both in the time and the frequency domains – a very complex dependence on the characteristics of the static field, the rf circuitry, the signal acquisition and transformation techniques (the latter only

applies to frequency domain SNR) and, of course, the sample (Hoult and Richards, 1976). For the purposes of this thesis, the most important relationships can be summarised as follows:

$$\text{SNR} \propto \frac{V_s \cdot \omega_0^{7/4}}{T_s \cdot T_c^{1/2}} \; , \tag{1.12}$$

where V_s is the sample volume, while T_s and T_c represent the temperatures of the sample and the rf coil, respectively, whose inverse relationships with SNR are good news for cryoapplications, as they can partly compensate for the impact of low temperatures on the population difference (cf. equ. 1.2).

The increase of SNR with increasing ω_0 is the main rationale behind the quest for ever-increasing field strengths of MR magnets, especially for spectroscopic applications and medical imaging (e.g. Chakeres et al., 2003). Nonetheless, it should be stressed that the multiparametric nature of MR also brings about negative effects of higer field strengths (e.g. eddy currents) or positive effects at lower field strength (e.g. line narrowing) on the quality of MR data (e.g. Gruetter et al., 1996; Darrasse and Ginefri, 2003, cf. also Section 2.2) and that NMR at Earth's field strength is possible (e.g. Callaghan and Eccles, 1996).

Chapter 2. Subcellular *in vivo* MR

2.1. Summary

Objectives   The main purpose of the experiments in this chapter was to test the resolution limits of three-dimensional *in vivo* MRI and *in vivo* localised MRS in view of future biological applications at the cell and tissue level, especially to samples before, during and after cryopreservation.

Methods   To this end, a combination of high field strength, a high sensitivity probe and strong magnetic field gradients was employed to record MR images from embryos and localised MR spectra from oocytes of the frog *Xenopus laevis*, a model system popular in many branches of the lide sciences. Furthermore, drug uptake into the oocyte and its compartments was monitored after application of the trypanocide diminazene aceturate to the culture medium.

Results   The *in vivo* microscopic MR imaging series revealed intracellular dynamic rearrangements during mitotic cleavages, visualised nuclear division and allowed to follow cell migration as well as tissue and organ formation during embryogenesis. All these processes have been observed in detail before but the non-invasive approach taken here now allows to monitor the entire embryological development in individual *Xenopus* frogs whose opaqueness represents a major obstacle for optical methods. The localised *in vivo* MR spectra obtained from the subcellular compartments of *Xenopus* oocytes clearly show differences between the nucleus and the two cytoplasmic regions in terms of both lipid contents and drug uptake.

Conclusions   Both MRI and localised MRS are capable of monitoring intracellular processes in large single cells. Given the appeal of their non-invasiveness for biological investigations and taking into account ongoing technological developments, it appears plausible that they both could eventually become a routine tool for studies of tissues, cell agglomerations and possibly even single cells, at least in the hydrated state.

2.2. Review of previous studies

Developmental biology has spurred – and in parallel profited from – technological developments providing the means to observe how the zygote divides, proliferates and transforms in the course of embryogenesis from a single cell into a complex multicellular network of differentiated cells (Gilbert, 2003). Many of these tools have reached reference status – fate maps, for example, now exist for all major model organisms or parts thereof and helped tremendously in providing fascinating new insights into developmental processes (e.g. Clarke and Tickle, 1999). Nonetheless, as the vast majority of the currently prevailing techniques are invasive – i.e. potentially disturbing wild-type cellular processes in a method-specific way (Clarke and Tickle, 1999; Gilbert, 2003; Keller et al., 2003; Cherry, 2004) – the availability of non-invasive alternatives or complements for the observation of developmental processes becomes crucial (cf. Schatten and Donovan, 2004). This is especially true in light of accumulating evidence which strongly suggests that investigations of cellular properties have to take into account the native physiological environment of the cells, including their three-dimensional interactions with neighbouring cells and extracellular structures (Wang et al., 1998; Beemster et al., 2003; Alcaraz et al., 2004; Zelenka, 2004; Sepich et al., 2005; Nelson et al., 2005).

In this framework, opaque system like the model frog *Xenopus laevis* pose considerable challenges, and transparency, therefore, traditionally was an important prerequisite for species to become model systems in developmental biology (Elinson, 1997). Consequently, previous studies in *Xenopus* have employed various strategies to work around the opaqueness by employing classical histological techniques (Nieuwkoop and Faber, 1956; Hausen and Riebesell, 1991), surface techniques (Keller, 1978; Concha and Adams, 1998), fluorescence staining (Alarcón and Elinson, 2001; Chalmers et al., 2002, 2003; Huisken et al., 2004), albinos (Keating and Cork, 1994) or cell extracts (Wignall et al., 2003). Incidentally, one of the features responsible for the popularity of *Xenopus* amongst experimental biologists – the large oocytes of about 1.2 mm in diameter – also renders it an ideal test system for subcellular MR imaging and spectroscopy: intracellular structures basically scale with cell size, MR signal intensity with voxel dimension, and SNR with sample volume (cf. equ. 1.12) as well as – for many-turn solenoid microcoils – inversely with the square root of the coil diameter (Peck et al., 1995). For current microimaging technology, *Xenopus* oocytes provide the necessary balance between these different constraints.

MR microscopy was previous performed on mouse (Smith et al., 1994; Dhenain et al., 2001) and even human embryos (Smith, 1999) fixed at different stages, which delivered information-rich and beautiful three-dimensional image series. In *Xenopus* embryos, successful *in vivo* attempts to follow cell lineages (Jacobs and Fraser, 1994; Ahrens et al., 1998) and even gene expression (Louie et al., 2000; Bell and Taylor-Robinson, 2000)

during development have been reported, though in these studies, the injection of contrast agents did not allow image acquisition to start before the 32-cell stage.

As the first microscopic MR images of a single cell (Aguayo et al., 1986) were acquired from unfertilised *Xenopus* oocytes, an observational gap hence existed between the single-cell and later embryonic stages. To close this gap was the first aim of the experiments presented in this chapter.

With localised MRS, only limited success has been achieved on a cellular scale before: Posse and Aue (1989) reported lipid peaks from 250 μm MR slices of *Xenopus* oocytes but they were unresolved with respect to the different intracellular contributions, such that the spectrum of the slice through the nucleus contained cytoplasmic signal. Grant et al. (2000) recorded a MR spectrum from a $(220\ \mu\text{m})^3$ voxel within an *Aplysia californica* neuron. However, as the voxel barely fit inside the cell, intracellular structures could not be distinguished.

Minard and Wind (2002) used chemical shift imaging and reported spectra from multiple voxels positioned in a *Xenopus* globule, a translucent sphere of about 100 μm diameter obtained from a juvenile's ovary. The different voxels, however, delivered indistinguishable spectra. Besides, as these globules have no germinal vesicle and do not stain for DNA, they can not be considered realistic model cells.

Diffusion-weighted MRS draws on intracellular molecules having smaller diffusion coefficients than extracellular molecules because intracellular and compartmental boundaries restrict diffusion, and this has successfully been exploited to differentiate between intracellular and extracellular ^{1}H signal contributions of non-water molecules (van Zijl et al., 1991; Pfeuffer et al., 2000). Different intracelluar regions, however, can not be distinguished this way.

Some other nuclei, e.g. ^{133}Cs and ^{31}P, exhibit observable chemical shift differences in different environments, which can serve to discriminate between an intra- and extracellular location (Wellard et al., 1994; McCoy et al., 1995). Using ^{31}P chemical shift differences or lineshape analysis of ^{14}N ammonium, cytoplasmic and vacuolar regions in maize root tissue could be distinguished (Lee et al., 1990; Lee and Ratcliffe, 1991). Neither of these methods, though, is voxel-selective, nor do they employ ^{1}H, the dominant nucleus in cellular biochemistry.

To achieve subcellular non-water ^{1}H MR spectroscopy, the MR setup has to be highly sensitive, invoking the need for a strong static magnetic field, strong gradients and micro rf coils. A $(2\ \mu\text{m})^2$ in-plane resolution has previously been achieved in ^{1}H MR water

Table 2.1.: Displacement errors for voxels of 200 μm unit length.

Pulse width	Pulse length[a]	Magnetic field strength			
		1.5 T	9.4 T	14.1 T	18.8 T
2.75 kHz	2 ms	11.8 %	72.9 %	109.1 %	146.3 %
5.5 kHz	1 ms	5.9 %	36.4 %	54.5 %	73.2 %
11 kHz	0.5 ms	2.9 %	18.2 %	27.3 %	36.6 %

[a]length of the respective sinc3 pulses (Bruker Biospin)

images of 50 μm thickness from cylindrical plant cells that have a planar diameter of tens of microns (Lee et al., 2001). But ^{1}H non-water MRS voxels can currently not be scaled down that much, mainly because the ^{1}H signal from non-water metabolites naturally is very low. This is also an issue with the observation of drug delivery and metabolism, for which non-localised MRS of a number of nuclei has proven effective in model systems or in conjunction with contrast agents (Malet-Martino and Martino, 1992).

The smallest voxel dimension realistically achievable was estimated to be about 200 μm, which is small enough for a voxel to be placed selectively in the animal or vegetal cytoplasm or in the nucleus of *Xenopus laevis* oocytes arrested in the prophase I (a phase in the cell cycle where the cell has a nucleus). The large cell size required a correspondingly large rf coil and resulted in SNR loss with respect to possible smaller rf coil dimensions but this effect could be compensated by the relatively high magnetic field of 14.1 T.

In strong magnetic fields, however, chemical shifts can cause a significant displacement error in MRS (Gruetter et al., 1996). Table 2.1 shows the displacement errors at different rf pulse bandwidths and static magnetic field strengths for the chemical shift span of 5 ppm, the range which covers most of the signals relevant for *in vivo* 1H MR spectroscopy. They were calculated by dividing 5 ppm by the chemical shift span corresponding to the specified rf bandwith and the magnetic field. The displacement error increases with magnetic field strength and decreases with rf pulse bandwidth. Experiments with a voxel size of about 200 μm would thus require a much higher rf bandwidth (11 kHz) and a shorter rf pulse (0.5 ms) than usual. Even under these conditions, the theoretical displacement error is 27.3 % at 14.1 T. The large bandwidth, in turn, requires a large magnetic field gradient. Table 2.2 shows the required gradient field strengths for the respective voxel size and rf bandwidth. They increase with rf pulse bandwidth and decrease with voxel size. At $(200 \ \mu m)^3$, a gradient field strength of 1.35 T/m is required.

Table 2.2.: Gradient fields required by rf bandwidth and voxel size at 14.1 T.

Pulse width	Voxel size		
	$(200 \; \mu\text{m})^3$	$(100 \; \mu\text{m})^3$	$(50 \; \mu\text{m})^3$
5.5 kHz (1 ms)	0.67 T/m	1.35 T/m	2.7 T/m
11 kHz (0.5 ms)	1.35 T/m	2.7 T/m	5.4 T/m

The capacity of the gradient coil employed here allows still higher gradient strengths but these cause larger eddy currents and possibly also signal distortions in MRS experiments (Lee et al., 2001).

Obtaining non-water ^{1}H spectra from cellular compartments of the *Xenopus* oocyte in the natural state and upon drug delivery was the second aim of the experiments reported in this chapter. The selected drug is an antitrypanosomal agent: diminazene aceturate (also referred to as berenil), the diminazene component of which is known to strongly bind to nucleic acid duplexes by forming hydrogen bonds (Pilch et al., 1995). Thus, MR spectra obtained with sufficient SNR from the nucleus can be expected to reflect both the transport into the nucleus and the DNA binding of the drug.

2.3. Experimental approach

2.3.1. Oocyte and embryo preparation

Sexually mature *Xenopus laevis* frogs were purchased from Xenopus I (Michigan, USA) or Xenopus Express (Haute-Loire, France). Stage VI oocytes arrested in prophase I were surgically harvested from ice-anesthetised females, defolliculated by treatment with 0.2 % collagenase (Sigma, type I, St. Louis, USA) in $0.33\times$ modified Ringer's solution (33 mM NaCl, 0.6 mM KCl, 0.66 mM $CaCl_2$, 0.33 mM $MgCl_2$, 1.7 mM HEPES, pH 7.4) and stored in oocyte Ringer (OR_2) buffer (82.5 mM NaCl, 2.5 mM KCl, 1 mM $CaCl_2$, 1 mM $MgCl_2$, 1 mM Na_2HPO_4, 5 mM HEPES, pH 7.6). The temperature throughout the experiments in this chapter was kept at $(21 \pm 1)°$C if not mentioned otherwise.

For the drug uptake experiments, the oocytes were immersed in an aqueous solution of 250 mM diminaze aceturate (Sigma, St. Louis, USA) and inserted into the MR tube containing the same solution. The relatively high drug concentration resulted in noticeable osmotic swelling (up to 6 % in diameter, i.e. a fractional volume change of about 20 %) but did not seem to affect the overall state of the oocytes, which appeared normal.

Fertilised embryos were prepared using *in vitro* fertilisation procedures (Kay and Peng, 1991; Sive et al., 2000). In brief, metaphase II oocytes were obtained from females injected with 600 to 800 IU (according to body size) of human chorionic gonadotropin (HCG, Daesung microbiological labs Ltd., Korea) into the dorsal lymphatic sac to induce ovulation, then fertilised with sperm from a macerated testis, dejellied by gently swirling in 2 % cysteine solution (pH 7.8) and cultured in $0.33\times$ modified Ringer's solution. All experiments described in this chapter were performed at KBSI, all frogs used were healthy, and all handling and manipulation of the animals was performed in accordance with the ethical guidelines at KBSI.

2.3.2. Parameters for subcellular MR experiments

Imaging

A homemade custom-built MR microscopy probe with a maximum gradient of 10 T/m (Lee et al., 2001) has been used on a Bruker DMX 600 spectrometer with standard microimaging equipment (Bruker Biospin, Rheinstetten, Germany) installed at the Korea Basic Science Institute (KBSI) in Daejoen, Republic of Korea.

The rf coil was prepared by winding six turns of enamel-coated copper wire of 0.5 mm outer diameter around a capillary NMR glass tube (Wilmad-LabGlass, Gardiner, USA). A tube of 1.7 mm outer diameter and 1.3 mm inner diameter was used to image the early developmental stages, and 1.9 mm outer and 1.5 mm inner diameter to monitor complete embryonic development, which allowed the embryos to develop more freely. To restrict evaporation during the long-term experiments, while at the same time allowing for sufficient gas exchange, both ends of the glass tube were given a parafilm seal into which two to three pinholes were pierced.

The images were acquired using a spin-echo sequence (MSME routine, Bruker Biospin, Rheinstetten, Germany) with lipid suppression using three chemical shift-selective pulses and spoiling gradients. The echo time has been set to 10 ms, which yielded the best contrast in the embryonic images. A fast spin-echo sequence employing multiple echoes was tested but did not give sufficient contrast. Each embryo was placed in the magnet before the first cell division, and MR images were recorded continuously until the tailbud stage. At that time, the embryos were removed from the magnet and released to a rearing solution where they grew to normal tadpoles without obvious malformations or abnormal behaviour.

Spectroscopy

For subcellular MRS, pilot images were acquired with a spin-echo sequence and simultaneous suppression of the lipid peaks between 0 and 3 ppm by three succesive sinc3 pulses of 3 ms length and 2070 Hz bandwidth centered at 1.5 ppm. The methine peak at 5.3 ppm, however, could not be reached this way.

For single voxel spectrosocpy, one 90° pulse of 0.5 ms and two 180° pulses of 0.4 ms were applied in a Point REsolved Spectroscopy Sequence (PRESS) (Bottomley, 1987) along with spoiling gradients of 1 ms and 100 mT/m between pulses, which led to a minimum echo time of 6.5 ms. For water suppression, three successive sinc3 pulses of 19 ms were applied along with spoiling gradients of 6 ms and 120 mT/m. To minimise localisation errors, a rf bandwidth of 11 kHz was chosen, which required gradients of up to 1.5 T/m for a voxel of 180 mm unit length (cf. Table 2.2).

The acquisition parameters were: T_R = 2000 ms, SW = 10 kHz, acquisition size = 4096, NA = 256, T_{exp} = 8.5 min, exponential filter width = 20 Hz, temperature = 18°C. T_E = 8.4 ms was used for $(180 \text{ mm})^3$ voxel spectra, and 6.5 ms for $(200 \text{ mm})^3$ voxel spectra. For lipid T_2 measurements in the cytoplasm, localised spectroscopy with $(200 \text{ mm})^3$ voxels was employed with 10 different echo times in intervals of 4 ms, starting at 6.5 ms. The measurement was repeated on five individual oocytes. For magic angle spinning experiments, an indirect detection PFG nano HX probe (4 mm) was used in a Varian UNITY INOVA 500 NMR Spectrometer. Four stage VI oocytes were placed in the 40 ml MAS sample tube with 90 % H_2O / 10 % D_2O, and spun at 2.8 kHz. For signal acquisition, a simple pulse-and-collect method was used. Water suppression was achieved by a weak pre-saturation pulse of 2.0 s. A 90° flip angle of 14.3 ms and a repetition time of 2.05 s were employed.

2.3.3. Partition coefficient calculation

The partition coefficient P is a measure of a molecule's hydrophobicity. It attains high values for hydrophobic substances and is low for hydrophilic ones. P was calculated for both diminazene and aceturate by two independent methods – with the ClogP program (available at http://www.biobyte.com, developed by BioByte Corp., Claremont, USA) employing the method of Hansch and Leo (1995) and with the KOWWIN program (available at http://www.syrres.com/esc/kowwin.htm, developed by Syracuse Research Corp., Syracuse, USA) based on the method of Meylan and Howard (1995).

2.4. Results

2.4.1. *In vivo* MRM of cell division

Figure 2.1 shows MR images of the interior of a zygote during the first embryonic cell division. The images (taken at intervals of 9 min) are part of multi-slice images captured every 2.2 min between 1.5 hpf and 2.8 hpf. The complete image sequence until 3.2 hpf is given in Movie 2.1. Note that these quick first cell divisions have been slowed down in the experiment by lowering the temperature to $(15 \pm 1)^{\circ}$C in order to allow for the cytoplasmic movements to be followed nearly in real time.

The first image in Fig. 2.1 shows the cell before the onset of cleavage furrowing. From images 2 to 4, the first cleavage furrow progresses and the interface between animal and vegetal cytoplasm temporarily flattens before it exhibits differential motion again in
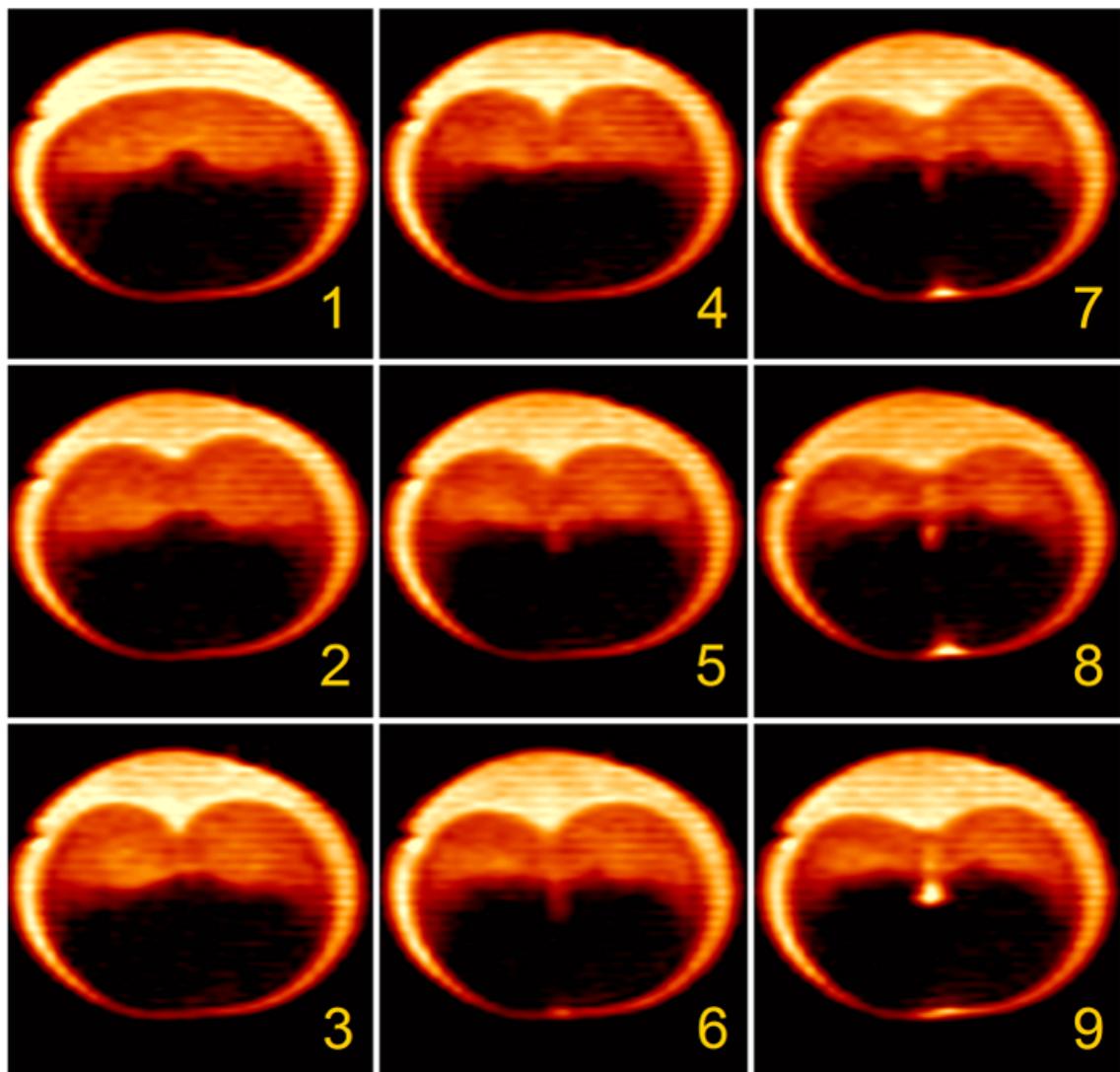
Figure 2.1.: MR images of cytoplasmic rearrangement during initial cell divisions. Nine *in vivo* MR images of a developing embryo recorded during 1.5 - 2.8 hpf at 9 min intervals, taken out of a sequence of images acquired at 2.2 min intervals which is provided as Movie 2.1 Ⓜ. Animal and vegetal cytoplasmic rearrangements accompanying with the progression of cell cycle are readily visible: Slice thickness = 200 μm, pixel size = 23 μm $\times$ 46 μm, imaging time per slice = 2 min.

images 5 to 9. Furrow progression at the vegetal pole of the embryo can also be observed. These dynamic cytoplasmic rearrangements within the cleaving zygote match very well with image data previously obtained from series of embryos by histological sections (Hausen and Riebesell, 1991; Danilchik and Denegre, 1991) but here, they were obtained *in vivo* from continuous observation of one and the same individual.

The image intensity mainly reflects local changes in the yolk platelet concentration, and the bright regions in the animal cytoplasm – best to discern in image 8 – correspond to a low yolk platelet density. This is in excellent agreement with histologically observed spatial distributions of yolk platelets in the animal cytoplasm (Hausen and Riebesell, 1991). The bright central region of the embryo in images 8 and 9 indicates blastocoel formation as the second cleavage furrow progresses.

Obviously, such internal movements within individuals cannot be followed by traditional fixation and physical sectioning methods (Hausen and Riebesell, 1991; Sive et al., 2000; Chalmers et al., 2003), nor by computed tomography, as long as it requires cryofixation (Larabell and Le Gros, 2004). This is especially relevant since the actual timing and extent of the cytoplasmic rearrangements varied between individuals.

Figure 2.2 shows MR images of a different embryo undergoing cell divisions from shortly after fertilisation up to the 6th cleavage. Temperature was kept at (18 ± 1)°C to speed up development with respect to the previous experiments (cf. Fig. 2.1). From a sagittal slice image, the positions of two axial slices – one in the animal and the other in the vegetal cytoplasm – were chosen (Fig. 2.2A) and MR images acquired continuously every four minutes (Fig. 2.2B; see also Movie 2.2).

The image sequence clearly reveals intracellular topological and chronological details of the cleavage process *in vivo*. The difference in brightness between the animal and vegetal slices recorded at 0.8 hpf can be attributed to large yolk platelets which are unevenly distributed from the beginning – with the vast majority in the vegetal hemisphere – and only reach out to the animal pole in a swirl due to cortical rotation (Danilchik and Denegre, 1991), which also specifies the embryo's dorso-ventral axis (Elinson and Rowning, 1988).

The slices at 1.5 hpf show that the first cleavage furrow has already passed through the animal but not the vegetal hemisphere (as in Fig. 2.1, image 6), while the densification towards the cleavage furrows of the dark structures in the vegetal slice at 2 hpf, together with the neighboring frames in Movie 2.2, probably reflect yolk platelets assembled along the path of the cleavage furrow (cf. Byers and Armstrong, 1986, Fig. 7b).
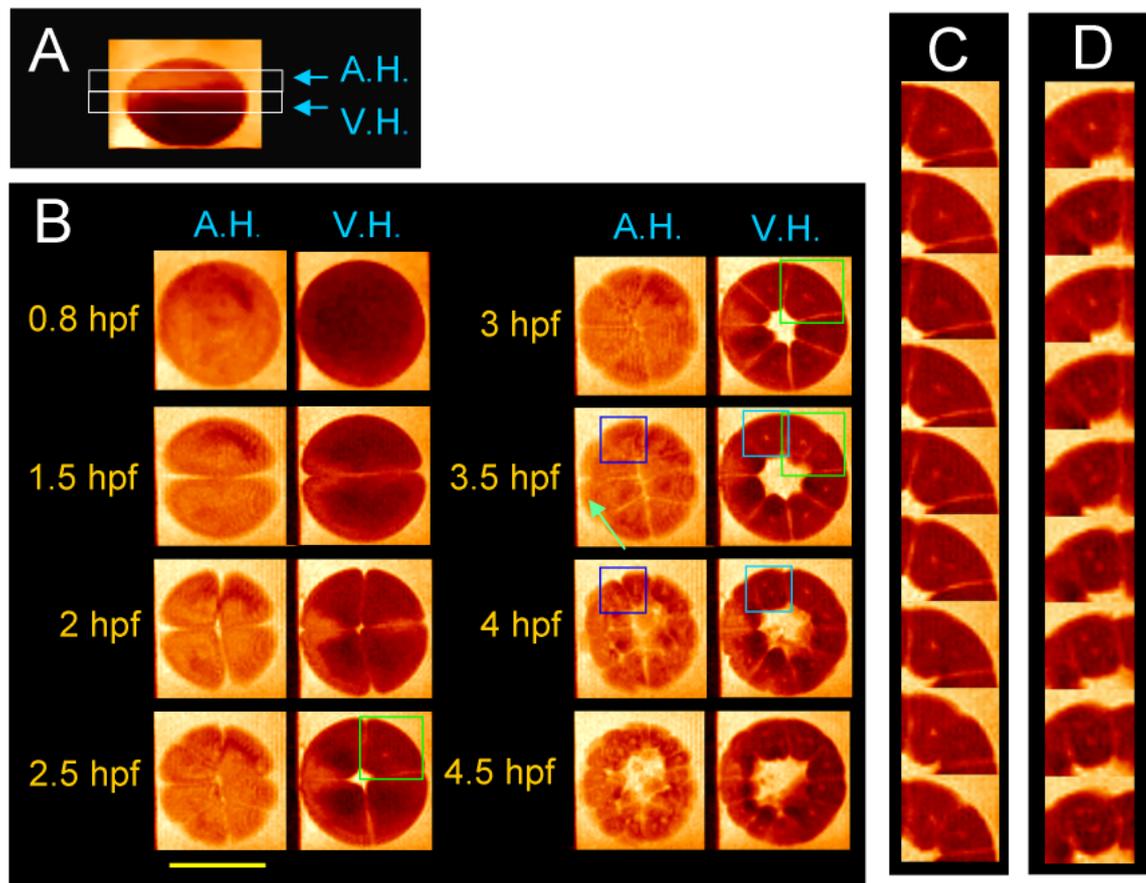
Figure 2.2.: Temporal series of MR images taken during the early stages of *Xenopus laevis* embryonic development. (A) Sagittal slice image of the zygote. Two slices for axial sections are indicated in their position and thickness. The upper part is the animal region, and the lower part is the vegetal region. (B) Axial slice images from the zygote to the blastula stage. A.H.: animal hemisphere (the hemisphere closer to the nucleus), V.H.: vegetal hemisphere. The cells boxed in blue (animal half) and light blue (vegetal half), respectively, in the images taken at 3.5 hpf and 4 hpf are dividing at right angles to one another, thereby producing either two superficial cells (detailed in Fig. 2.1C) or one superficial and one deep cell (detailed in Fig. 2.1D). Scale bar = 1 mm. (C) Close-up of the cell divisions occuring in the green-box during 2.8 - 3.4 hpf, recorded with 4-minute intervals. (D) Cell divisions in the light blue-box during 3.5 - 4.1 hpf. The images were obtained from an original FOV = 3 mm, MTX = 128×128 pxl^3, pixel size = 23 μm × 23 μm, slice thickness = 200 μm, no gap; SW = 25 kHz, T_E = 10 ms, T_R = 2000 ms, NA = 1, temporal resolution = 4 min.

Compared to normal development as described in the *Xenopu laevis* Normal Table (Nieuwkoop and Faber, 1956), the embryo depicted in Fig. 2.2 had altered cleavage directions from the third cell division on. Similar phenomena are frequently observed during initial cleavages (Black and Vincent, 1988) but since these reorientations had been suggested to exhibit a dependence upon strong magnetic fields (Denegre et al., 1998), they will be described here in detail: If v is to represent vertical cleavages parallel to the animal-vegetal (AV) axis and h horizontal cleavages perpendicular to the AV axis, the normal cleavage sequence (Nieuwkoop and Faber, 1956) is v (first cleavage, resulting in 2 cells) – v (second, 4 cells) – h (third, 8 cells) – v (fourth, 16 cells) – h (fifth, 32 cells) – v (sixth, 64 cells). During the MRI experiments described here, cleavage always occurred in the order v (first) – v (second) – v (third) – h (fourth) – v (fifth, 32 cells), i.e. the third and later cleavages were orthogonal with respect to the normal sequence.

The altered divisions correlated with changes in the first occurrence of a deep cell. In normal development, all divided cells until the 5th cleavage (or 32-cell stage) are superficial (i.e. epithelial) cells, and the first deep (and thus nonepithelial) cell appears with the 6th cleavage, at the 64-cell stage (Keller, 1991; Chalmers et al., 2003), while the first deep cell appeared with the 5th cleavage (32-cell stage) in the embryos that subjected to MRI (Fig. 2.2B, 4 hpf.).

The horizontal fourth cleavage is not easily noticeable with the given slice orientation in Fig. 2.2B, but nonetheless left its traces in the image sequence: In the image taken at 4 hpf and in the corresponding frames of Movie 2.2, a cell in the animal half (blue-boxed) and another one in the vegetal half (boxed in light blue) are dividing at orthogonal directions with respect to each other. This clearly indicates that they must have been separated before by a horizontal cleavage. In the image at 3.5 hpf, an arrow points at a line (corresponding to an outer cell membrane) separating a brighter region (left) from a darker one, hinting again at a horizontal cleavage, as the culture medium (with high signal intensity) flows into the progressing furrow in the indicated region of the image slice.

Third cleavages did not always occur synchronously, although they frequently did. One cell (green-boxed) finished division about 30 min later than the other cells. Thus, during the third cleavage of one cell, fourth cleavages (horizontal) have been progressing in other cells at the same time. The phenomenon is, however, not limited to embryos exposed to a magnetic field. Some of the embryos grown outside the magnet also underwent asynchronous cleavages, and similar observations have been made by others (Black and Vincent, 1988). Neglecting these asynchronies, the cells divide at nearly constant time intervals (determined mainly by temperature) until the mid-blastula transition (Gilbert, 2003), and the image series obtained here give a cleavage period of about 40 min.

Nuclear divisions for two cells (boxed in green and light blue, respectively) are shown in detail in Figure 2.2C-D. From the series, the velocity at which the two daughters of nuclei separate during cleavage could be deduced. In Figure 2.2C, a nuclear separation of 230 μm in surface-parallel direction (terminology according to Chalmers et al., 2003) occurs during 36 min, which equals 6.4 μm/min on average. In Figure 2.2D, the displacement is 65 μm during 26 min in surface-perpendicular direction, i.e. 2.5 μm/min. Subsequent images (cf. also Movie 2.2) allow to observe an increasing number of segregated nuclei and dividing cells.

2.4.2. *In vivo* **MRM of embryogenesis**

Taking advantage of high temporal and spatial resolution achieved in the above-mentioned experiments, the next undertaking was to observe all embryological stages in one and the same *Xenopus* embryo *in vivo*, as visualised in Movie 2.3.
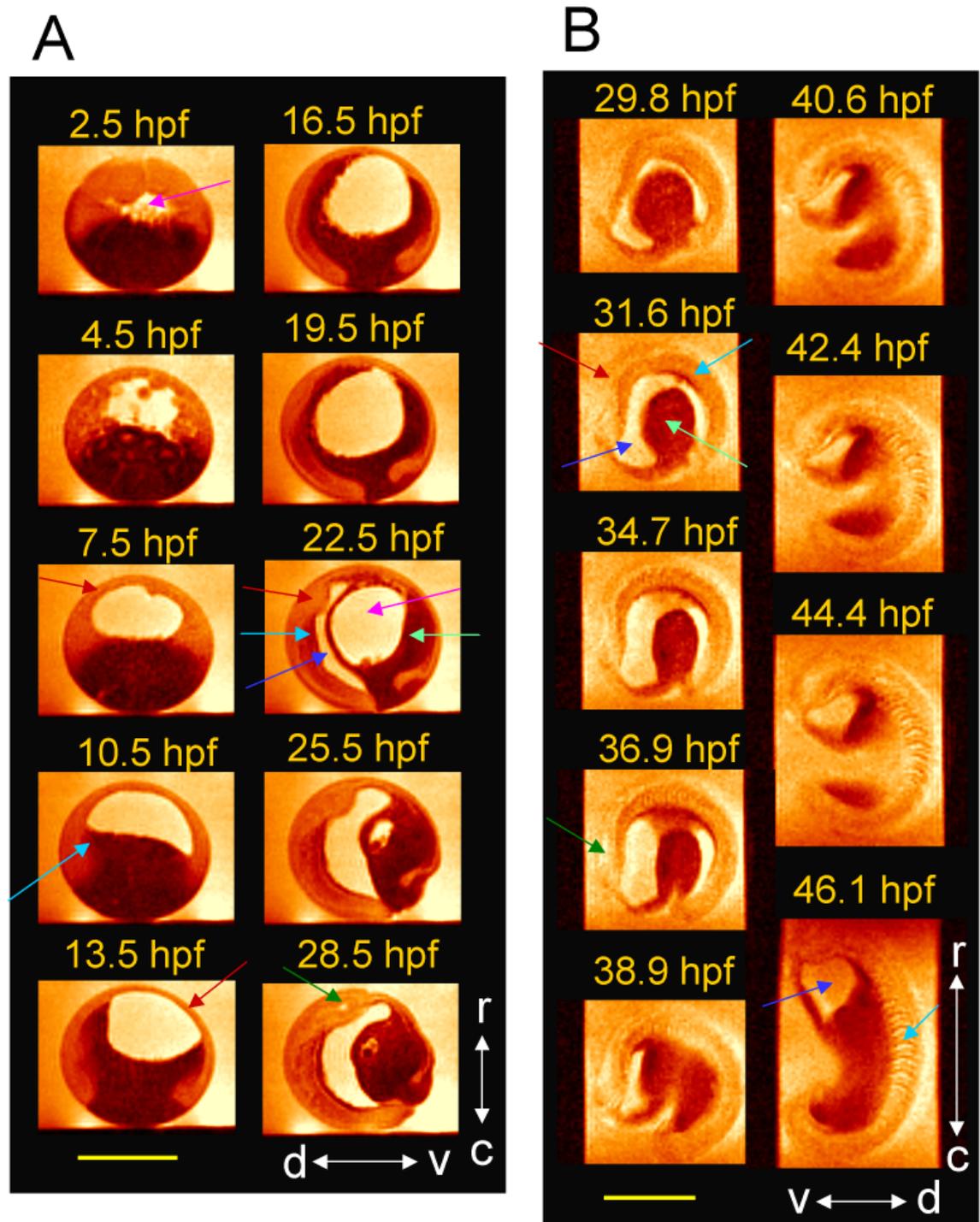
Figure 2.3.: Temporal series covering the complete embryonic development of *Xenopus laevis*. (A) Sagittal images from the initial cleavages to the mid-neurula stage. The parameters were: Original FOV = 3 mm, MTX = 128×128 pxl^3, pixel size = 23 μm × 23 μm, slice thickness = 200 μm, SW = 25 kHz, T$_E$ = 10 ms, T$_R$ = 3000 ms. NA = 2, T$_{exp}$ = 12 min for images at 2.5 hpf and 4.5 hpf, and NA = 4, T$_{exp}$ = 24 min for the image at 7.5 hpf and thereafter, in accordance with the slowdown of the cell division cycle at the midblastula transition when large-scale transcription starts. Arrows indicate: magenta, blastocoel; dark red, ectoderm; light blue, mesoderm; blue, archenteron; light green, endorderm; dark green, brain ventricle. r: rostral, c: caudal; d: dorsal, v: ventral. Scale bar = 1 mm. (B) Axial images from the mid-neurula stage to the tailbud stage. Axis labels, scale bar and arrows as in A. Blue at 46.1 hpf, foregut; light blue, somites. The parameters were originally FOV = 3 mm, pixel size = 23 μm × 23 μm, slice thickness = 200 μm, SW = 50 kHz, MTX = 128×128 pxl^3, T$_E$ = 10 ms, T$_R$ = 2000 ms, NA = 2, T$_{exp}$ = 8 min.

Ten slices from this sequence have been assembled in Figure 2.3A and show an individual's 8-cell (2.5 hpf), blastulation (4.5 hpf - 7.5 hpf), gastrulation (10.5 hpf - 22.5 hpf) and neurulation (22.5 hpf - 28.5 hpf) stages. The temperature was kept at $(20 \pm 1)°$C to speed up the development relative to the previous experiments.

Blastocoel growth can be observed until 10.5 hpf, as can gradual differentiation of the cells into the three germ layers and beyond. Equally discernable is epibolic movement during gastrulation, along with the flattening of the blastocoel roof, the reshaping of the blastocoel and the involution of mesodermal material. Also visible in Movie 2.3 (and highlighted in Fig. 2.4) is the invagination of bottle cells which originated from marginal mesoderm, drive the archenteron formation and will later become part of the foregut. During neurulation, the newly formed archenteron displaced the blastocoel, thereby pronouncing dorso-ventral asymmetry, and the neural tube containing the brain ventricle has formed (28.5 hpf). Replaying the image sequence in reverse order allows the creation of fate maps – e.g. the brain ventricle and the somites (precursors of vertebrae and skeletal muscles) can be traced back to their mesodermal origin.

From a different perspective, Figure 2.3B depicts the development of another individual from the mid-neurula to the early tailbud stage, with neurulation (29.8 hpf - 31.6 hpf) and organogenesis (34.7 hpf - 46.1 hpf) readily traceable in these images. At 31.6 hpf, the neural tube, the archenteron, somitogenic mesoderm and yolk-rich endoderm are easily identified. In the following, the originally spherical embryo started to open ventrally, with the anterior region moving, while the tail remained relatively fixed. The subsequent images visualise further changes the embryo undergoes on its way to a straightened tailbud – somites form, and the archenteron gradually reduces to the foregut.

In an attempt to quantitatively assess characteristic parameters of morphogenetic biomechanics inside a developing embryo, the epibolic movement during gastrulation was then observed more closely, as illustrated in Figure 2.4. The position of the dorsal blastopore lip was recorded in each image. From the serial images, velocity vectors were calculated at each time point, and acceleration vectors from the velocity series. The accelerations of the blastopore lip are represented with magnitude and direction in Fig. 2.5.

Assuming that the mass of the blastopore lip remains constant (which is probably not true but a good approximation), the calculated accelerations are proportional to the time-dependent biomechanical net forces exerted on it. With the spatial and temporal resolution in these images being 23 μm and 48 min, respectively, the errors resulting from pixel size are within 0.5 μm/min for the velocities and within 10 nm/min^2 for the accelerations.
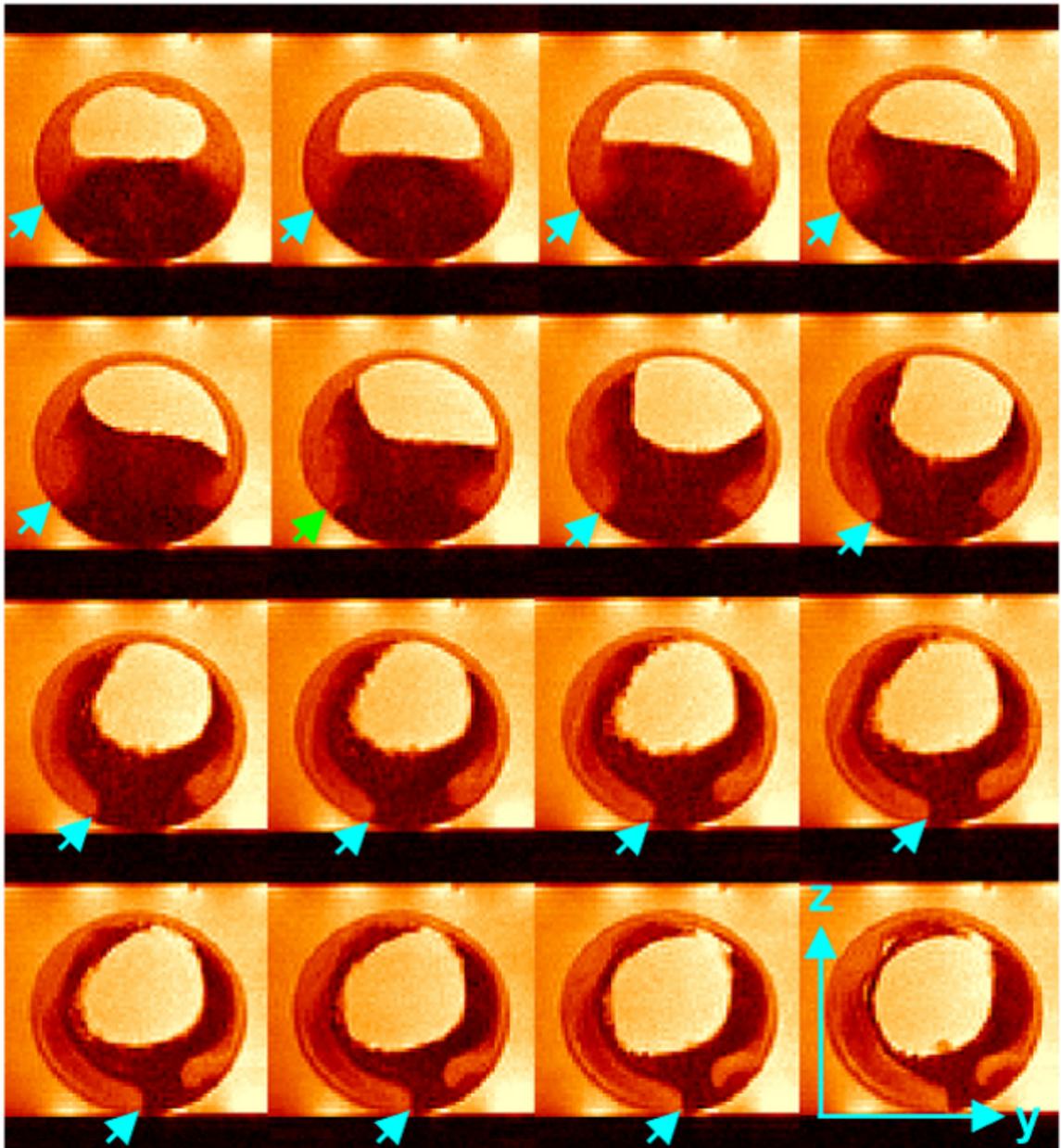
Figure 2.4.: Detailed time-lapse image sequence of gastrulation. Consecutive images taken at intervals of 48 min, starting at 8 hpf. The arrows indicate the moving cell front of the dorsal blastopore lip, with the green one in the second row pointing at the bottle cells. Coordinate axes were introduced to quantify epiboly biomechanics (cf. Fig. 2.5), with y corresponding to the ventral-dorsal direction, z to rostral-caudal. The imaging parameters were identical to those after 7.5 hpf in Fig. 2.3A. The complete sequence is provided as Movie 2.4 Ⓜ.
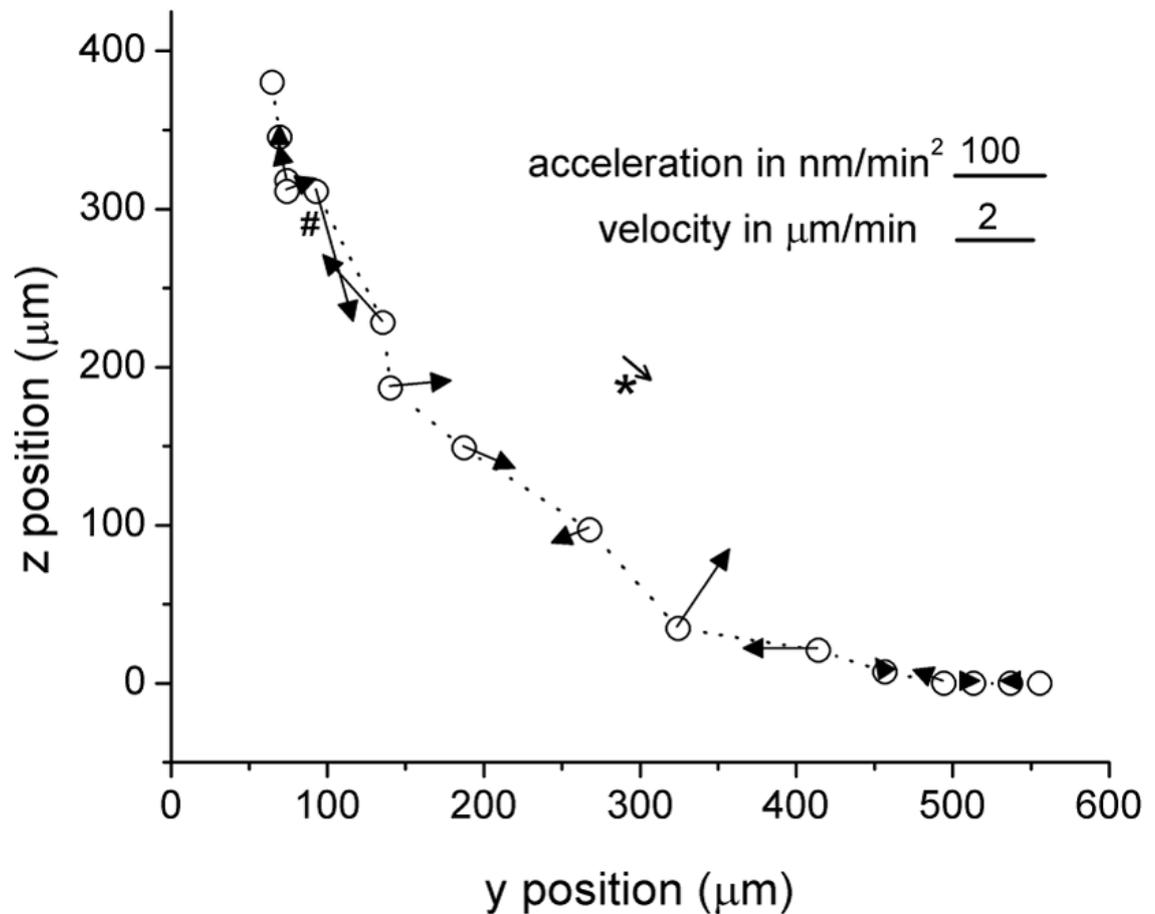
Figure 2.5.: Acceleration vectors during epibolic movement. The open black circles represent the location of the front of the epibolic movement at constant intervals of 48 min, as indicated in Fig. 2.4. Arrows represent the acceleration vectors calculated as the difference between two adjacent velocity vectors, divided by time. The velocity vectors – not depicted here, for clarity reasons (except for the average vector, marked by an asterisk) – had been obtained from the spatial displacement between two neighboring time points (represented by black circles, initial points on the top left, final ones at bottom right) divided by the time interval between subsequent images. The scale bars indicate the absolute velocity and acceleration values in the y-z plane. The largest value measured was 150 nm/min^2 (hash-marked arrow).

2.4.3. *In vivo* **subcellular MRS**

Figure 2.6A shows the ^{1}H MR pilot image of a single cell, a stage VI *Xenopus laevis* oocyte arrested in prophase I. It comprises of three major compartments – the nucleus as well as the animal and vegetal cytoplasm – which are clearly distinguished by intrinsic MRI contrast arising from the compartment-specific spin-spin relaxation times (T_2) of water, concordant with previously recorded water T_2 maps (12). The three cubes in the image indicate the actual position and width selected for the recording of localised spectra from isotropic voxels of $(180 \; \mu m)^3$ in each compartment.
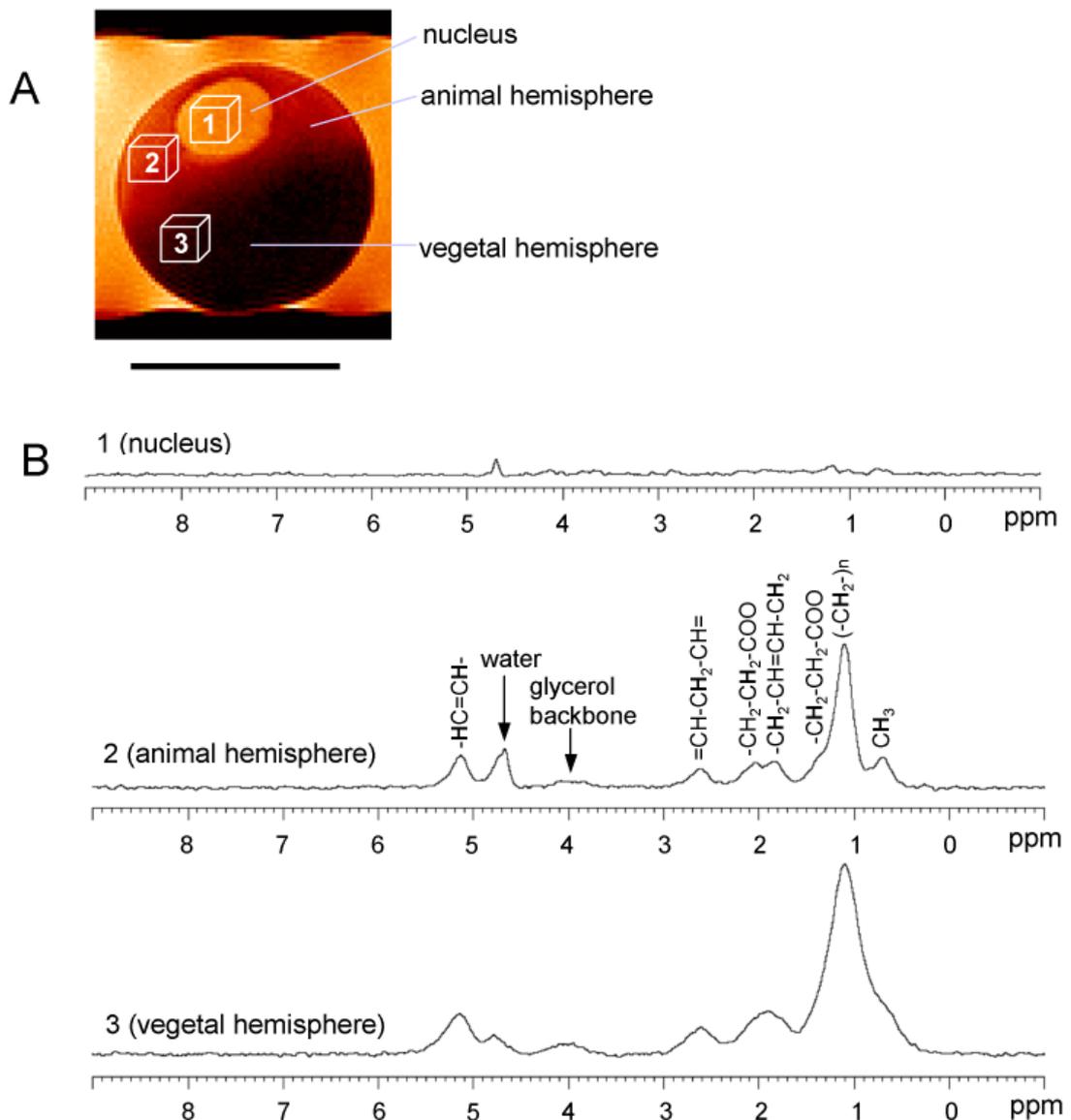
 Figure 2.6.: *In vivo* MR spectra from intracellular compartments of a *Xenopus laevis* oocyte. (A) High resolution image of a stage VI (prophase I-arrested) oocyte. Scale bar = 1 mm. Isotropic voxels of $(180 \; \mu m)^3$ were selected for localised spectroscopy of the nucleus as well as the animal and vegetal cytoplasm and are indicated by location and size of the boxes. (B) Localised spectra of the voxels indicated in (A). TAG resonances and contributing protons are indicated Szczepaniak et al. (assigned after 1999). Water peak (w) is referenced to 4.7 ppm. Note the absence of bleed over from the strong cytosolic lipid signals into the nucleus.

Figure 2.6B shows ^{1}H MR spectra obtained from these voxels, exhibiting notable differences: In the nucleus, the non-water signal was very low, while large peaks typical of triglycerides could be observed in the animal and vegetal cytoplasm – they represent methine, the glycerol backbone, methylene, and methyl residues, as indicated in the figure. The MR characteristics in the animal and vegetal cytoplasm also differed from each other: At identical voxel size, the integral of the triglyceride peaks in the vegetal cytoplasm was two to three times the value found in the animal cytoplasm, with the actual ratio varying between individual oocytes. The linewidths of the vegetal peaks were twice those of the animal peaks. To examine the reason for this factor, the spin-spin relaxation times (T_2) of the methylene peaks at 1.1 ppm in both compartments were compared. Values of (14 ± 1) ms and (12 ± 0.2) ms were obtained for the animal and vegetal cytoplasm, respectively – well in agreement with previously gathered data Sehy et al. (2001); Szczepaniak et al. (1999). The *in vivo* ^{1}H spectra did not reveal metabolites other than triglycerides.

To obtain a more resolved spectrum, several fresh prophase I-arrested stage VI *Xenopus* oocytes were subjected to a magic angle spinning (MAS) experiment. While subcellular variations could not be determined with this whole-cell technique, it yielded spectra with increased resolution and sensitivity, since dipolar broadening and susceptibility variation within the sample are being reduced Weybright et al. (1998). The triglyceride peaks were better resolved, and small additional peaks – creatine, choline, and phosphatidylcholine at 2.9 to 3.2 ppm Weybright et al. (1998) – were detected (Fig. 2.7).

The same voxel size and parameters as for subcellular MRS of untreated oocytes were subsequently employed to monitor the spectroscopic changes upon drug delivery in the three subcellular compartments of the *Xenopus* oocyte over time.

Figure 2.8A depicts the chemical structure of diminazene aceturate, with its MR signaling proton sites labeled (a-e). Figure 2.8B shows a MR spectrum of the medium, together with a spectral time series from the three oocyte compartments. The diminazene peaks (b, c) appear at 6.7 and 7.1 ppm, and the aceturate peaks (a, d, e) at 1.8, 3.4, and 7.8 ppm, respectively.

In the nucleus, diminazene and aceturate peaks showed differing kinetics: The aceturate peaks reached levels equivalent to those in the medium by one hour after immersion, while the diminazene peaks were notably smaller at that time and, after 6 h, reached only half the intensity of those in the medium. In the cytoplasm, the drug signal was superimposed with the natural triglyceride peaks. Diminazene peaks were not observed within 6 h, while aceturate peaks slowly grew with time.
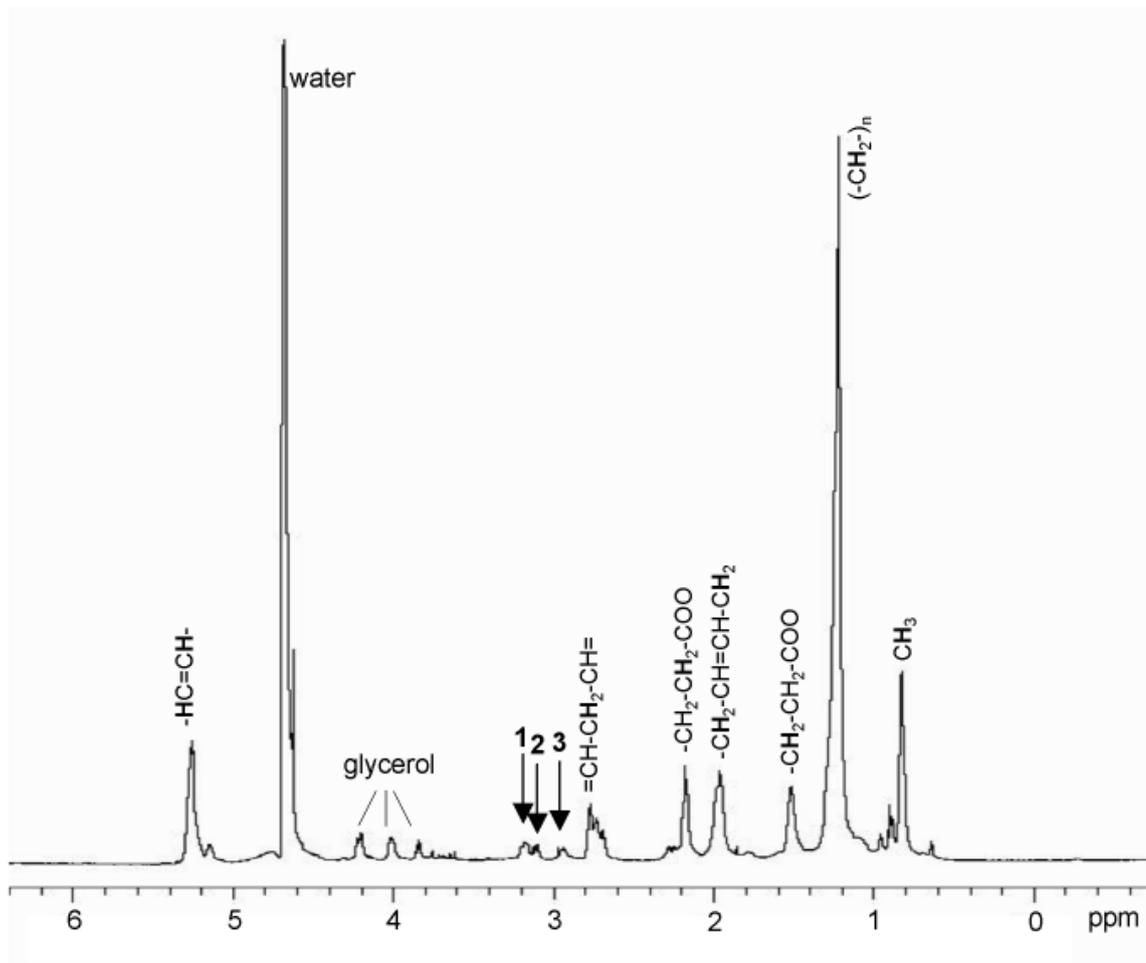
Figure 2.7.: ^{1}H MAS MR spectrum of *Xenopus laevis* oocytes. Four oocytes were spun at 2.8 kHz. Arrows indicate phospholipids (28). 1: phosphatidylcholine, 2: choline, 3: creatine. Water peak is referenced to 4.7 ppm.

Finally, it should be noted that, in contrast to the embryos undergoing third cleavage, the oocytes investigated in this section did not exhibit any morphological alterations with respect to the literature (e.g. Sardet et al., 2002).

2.5. Discussion

In vivo MRM can monitor subcellular features and their changes in the early *Xenopus laevis* embryo. Many of these appeared as they are known from previous – usually invasive – studies (Nieuwkoop and Faber, 1956; Hausen and Riebesell, 1991), though some of the early cell cleavage patterns differed from the standard description given in the Normal Table of *Xenopus laevis* (Nieuwkoop and Faber, 1956).

It may be surprising that the embryos develop normally after such an early and fundamental modification like third cleavage plane alteration but similar accounts of embryonic robustness have previously been given (Black and Vincent, 1988; Meinhardt, 2001; Patel and Lall, 2002).
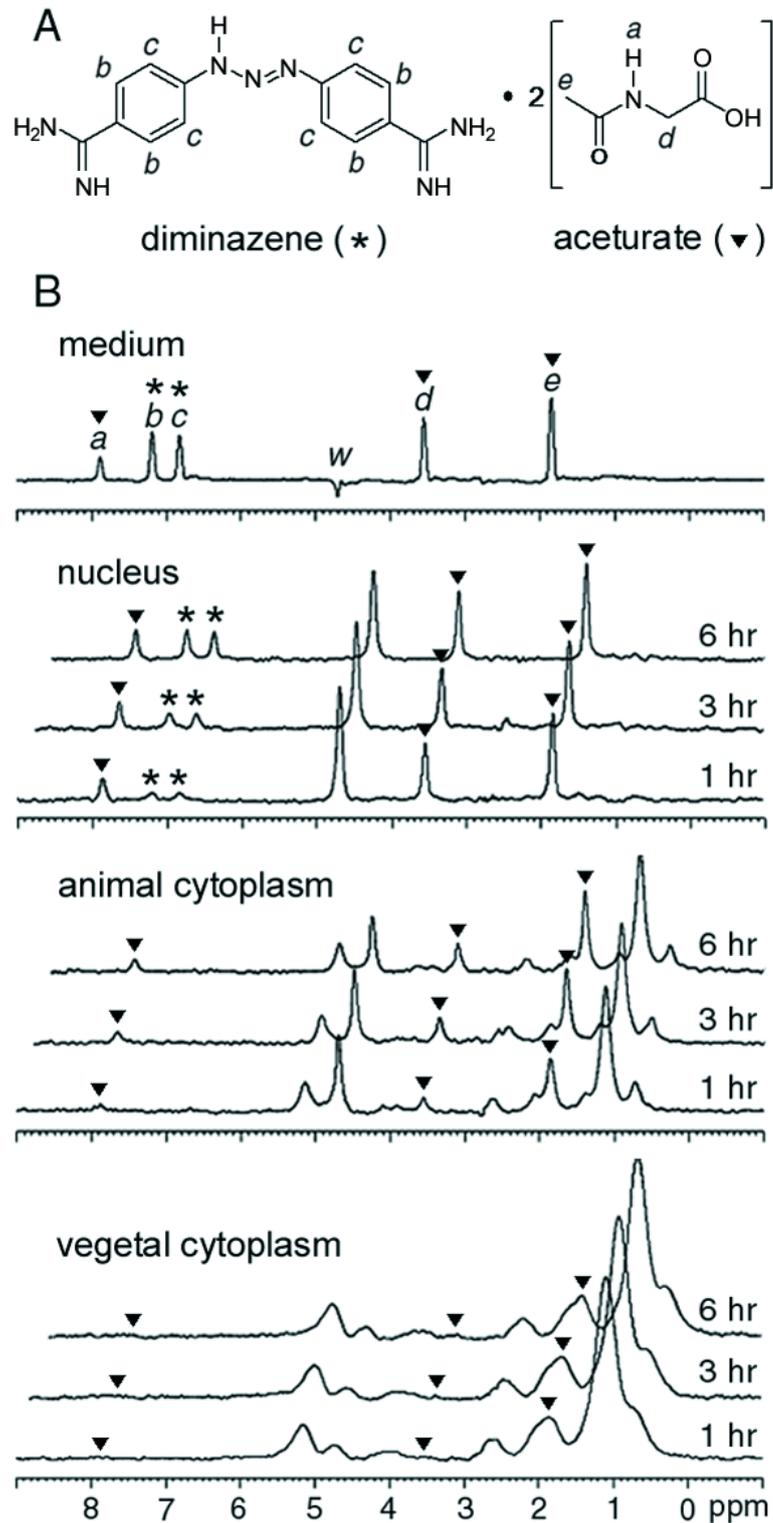
Figure 2.8.: Drug uptake into cellular compartments. (A) Chemical structure of diminazene aceturate, with MR-visible protons labeled as a-e. Diminazene is labeled with an asterisk (∗), and aceturate with inverted filled triangles (▼). (B) Localised spectra of the external medium, the nucleus, the animal, and the vegetal cytosolic region of a prophase I-arrested stage VI oocyte *in vivo*, taken at different times after immersion in diminazene aceturate. Water peak referenced to 4.7 ppm. Intensity scale applies to all spectra. a, d, e: aceturate (▼); b, c: diminazene (∗). The peak intensities of the diminazene peak c at 6.85 ppm and of the aceturate peak d at 3.55 ppm have been calculated, for each compartment and after 1 h, 3 h or 6 h, as the percentage of the respective peak intensity in the medium: Nucleus: 15, 24 and 51 for peak c and 81, 84, 95 for peak d; Animal: peak c not detectable, 18, 36 and 38 for peak d. Vegetal: peak c not detectable, peak d at 1 h not detectable, 3.2 and 6.2 at 3 h and 6 h, respectively.

On the other hand, the lack of obvious abnormalities in the tadpoles that had been subjected to long-term MRI meshes well with earlier findings that the teratogenic and mutagenic impact of strong magnetic fields on embryonic development is very low (Mild et al., 1981; Ueno et al., 1984; Schreiber et al., 2001), even if combined – as in our case – with exposure to radiofrequency pulses and persistently switching strong magnetic field gradients (Kay et al., 1988). Therefore, the proposed magnetic field-dependence of the alteration of the third cleavage plane in *Xenopus* embryos (cf. Denegre et al., 1998) will be explored in more detail in Chapter 3.

Besides documenting cleavage plane alterations, the MR images provided information on temporal aspects of mitotic events like cleavage furrow progression and yolk platelet aggregation as well as on embryonic features like deep cell formation, germ layer formation and organogenesis. Deep cell formation initiates epiboly (Keller, 1978), and the deep versus superficial cell distinction is an important step towards germ layer formation that is initiated by the invagination of bottle cells – and monitored by the MR image sequence (cf. Fig. 2.2, Movie 2.2), along with important steps in organogenesis (e.g. somitogenesis; cf. Fig. 2.4).

In the vegetal slices of Fig. 2.2B, bright spots can be seen to divide as the cells do, suggesting that they might be nuclei. No histological or optical sections at this stage are reported in the literature but histological images from the first cleavage and the early blastula (plates 13 and 17 in Hausen and Riebesell, 1991) indicate that the size of the nucleus (about 40 μm) does not change significantly in this phase of development. In the MR images, the boundaries of the spots are slightly blurred but within the histologically observed value. The blur results from the images having been acquired with a 200 μm slice thickness, which effectively sums up signals from within and around the nucleus.

The nuclei in the animal slice are not easy to discern before 4 hpf. This is partly because yolk platelets – whose low signal provides a dark background for the bright nuclei – are rare in the animal hemisphere during the early cleavages and partly due to the longer mitotic cycle after the onset of transcription.

It has to be noted that there is yet no tool other than MR microscopy to observe such dynamic developmental processes *in vivo* with intrinsic contrast inside opaque systems (cf. Alcaraz et al., 2004) but developmental MRM might well find applications in transparent systems, too.

This also means that it is time to engage in the development of a common framework which would allow to integratively store and link morphological, functional, develop-

mental and other 3D data acquired by different methods in the same model system or even comparative data across species. Such initiatives have already gained considerable ground in the cognitive sciences (Lancaster et al., 2000), and high resolution 3D morphological atlases – as they exist, e.g., of the mouse embryo (Dhenain et al., 2001) – constitute an important step towards the incorporation of developmental data.

As for *Xenopus*, an existing nomenclature for the orientations of the early cell divisions (Chalmers et al., 2003) is based on fluorescently stained mitotic spindles. In this reference system, the cleavage depicted in Figure 2.2C would be a parallel division because the mitotic spindle is oriented parallel to the surface of the embryo and results in the formation of two superficial daughter cells. Similarly, a division that gives rise to one superficial and one deep cell (as in Figure 2.2D) would be called perpendicular.

Such a surface-oriented description, though valid for the initial cleavages it was designed for, lacks the power to adequately describe three-dimensional development at later stages. Coordinate systems valid beyond the initial cleavages have long been in use (Nieuwkoop and Faber, 1956; Elinson and Rowning, 1988) but were recently challenged (Gerhart, 2002; Solnica-Krezel, 2005), and so – even though the necessary computational methods are already in place (Tyszka et al., 2005) – the development of *Xenopus* atlases will have to wait until consensus is reached on these issues.

One of the morphogenetic channels by which the gene expression and protein translation machineries drive growth and development is biomechanics. Yet although its importance was recognised long ago (Thompson, 1917), it received relatively little attention for decades – a situation that apparently is about to change, as biomechanical aspects begin to be incorporated into concepts of cytoskeletal architecture (reviewed in Ingber, 2003), tissue growth (Alcaraz et al., 2004; Nelson et al., 2005), tumorigenesis (Ambrosi and Mollica, 2002) and development (Keller et al., 2003; Kwiatkowska, 2004; Basu et al., 2005; Sepich et al., 2005; Lucchetta et al., 2005).

This creates the need to account for biomechanical stress during culture (Wang et al., 1998; Shook and Keller, 2003; Nelson et al., 2005) and manipulation (Thielecke et al., 2005) of cells and tissues, and it calls for techniques to measure the relevant parameters. Biomechanical properties of isolated tissues or individual cells have previously been determined *in vitro* (Moore, 1994; Vanni et al., 2003; Rosello et al., 2004; Bursac et al., 2005). Strain rates as well as curvatures could also be determined on the surface of plant meristems *in vivo* (Kwiatkowska, 2004), and convergence and extension movements during ongoing gastrulation have been followed by optical microscopy in labeled zebrafish embryos (Sepich et al., 2005).

For *Xenopus*, this optical approach is not a valid option, and with conventional fixation and sectioning, such studies are impossible or inaccurate, as a large number of embryos – with their individual biomechanical patterning – would have to be used for statistics. While the biomechanical properties were characterised here at just one spot, the analysis could easily be extended to areas – as it has been demonstrated in the zebrafish, both on the surface (Concha and Adams, 1998) and within the embryo (Sepich et al., 2005) – and volumes. On the other hand, studies of volume biomechanics in liquid systems like cells and tissues generally are rheological investigations (Verdier, 2003), for which MR techniques have proved very effective (e.g. Callaghan, 1991; Manz et al., 2003).

The negligible lipid signal in the spectrum obtained from the voxel in the nucleus demonstrates that although localisation errors are not entirely evitable in high-field MRS (cf. Table 2.1), there is no significant signal spill-over from the lipid-rich cytoplasm surrounding the nucleus. Localisation errors in these experiments can hence be considered to be confined within each compartments. Besides, the lack of lipid signal in the nucleus is consistent with its lack of yolk platelets (Danilchik and Gerhart, 1987; Hausen and Riebesell, 1991) and with a previous lipid ^{1}H MRI study of the *Xenopus* oocyte (Sehy et al., 2002). The observed differences in the lipid peak integrals in the cytoplasm also affirm earlier studies of yolk distribution within the oocyte (Danilchik and Gerhart, 1987) and agree well with triglycerides being the major neutral lipid component of many types of cells (Hakumäki and Kauppinen, 2000).

The similar T_2 values of the animal and vegetal methylene peaks imply that molecular motion occurs at the same time scale in both compartments and cannot account for the linewidth difference. Instead, the broad linewidth in the vegetal cytoplasm may stem from magnetic inhomogeneity in that region. It seems thus probable that yolk platelets – lipoprotein assemblies of different sizes (Lee et al., 1999) – have caused the inhomogeneities in the vegetal cytoplasm, perhaps along with mitochondria and other organelles with paramagnetic components. In line with this interpretation, previous studies found an apparent mitochondrial asymmetry along the animal-vegetal axis of the *Xenopus* egg (Tourte et al., 1984; Volodina et al., 2003).

The whole-cell MAS spectrum being dominated by lipids is in apparent contrast with previous whole-cell experiments in another large single cell, an *Aplysia californica* neuron (Grant et al., 2000), which brought about a negligible lipid signal and large amounts of other metabolites, including the neurotransmitter choline. Considering, though, that the *Aplysia* neuron is an already fully differentiated somatic cell, while the *Xenopus* oocyte is a germinal cell containing large fat stores to fuel quick embryonic development, these spectroscopically observed differences in lipid contents turn out to simply reflect, in both cases, physiological adaptations to the function of the respective cell type.

Alterations in ^{1}H NMR peak levels from intracellular lipids have been reported in various cell biological processes, such as cell activation, proliferation and apoptosis (Hakumäki and Kauppinen, 2000). Based on the observation that fertilised *Xenopus laevis* oocytes can undergo complete embryogenesis in a NMR tube during *in vivo* acquisition of MR images (Lee et al., manuscript in preparation), applications of localised MR spectroscopy to the above-mentioned processes would make embryonic development accessible to non-invasive *in vivo* investigations. Given that early-stage *Xenopus laevis* embryos are about 1 mm in diameter, oocytes up to the 8-cell or 16-cell stages would, under optimal conditions, be observable at single-cell resolution with a (180 μm)^3 voxel size. In the later stages, the voxels do no more provide single cell resolution, but the variation of lipids or other metabolites within a particular region of the developing embryo could still be studied non-invasively and in real time.

Alternatively, as the size of *Xenopus laevis* embryos does not change significantly until neurulation (Hausen and Riebesell, 1991), a voxel that contains a whole oocyte would allow to follow total lipid changes during cell division and embryonic development at real time, and the time for localised shimming at each voxel position could be saved.

The apparent spatial and temporal dissimilarities between diminazene and aceturate signals in the cellular compartments can be explained by their membrane permeability and macromolecule binding strength. The molecular weight of aceturate is 117.1 g/mol and that of diminazene is 281.3 g/mol. Since small molecules cross the cell membrane by passive diffusion at a rate mainly determined by the molecule's hydrophobicity which is commonly expressed in terms of the partition coefficient P between n-octanol and water (Sangster, 1997; Lodish et al., 2000), the permeability of the molecules can be estimated from calculations of the partition coefficients of the drug's components. The method of Hansch and Leo (1995) predicts log(P) to be 0.91 for diminazene and -0.91 for aceturate, which agrees well with the respective values of 1.5 and -1.02 that were obtained following Meylan and Howard (1995). These calculations indicate that the membrane is about two orders of magnitude more permeable to diminazene than to aceturate. Thus, the low amplitude of the diminazene signal in the nucleus must reflect binding effects.

This view is supported by both the signal amplitude and linewidth in the nucleus with time: Depending on the binding strength, bound molecules would give broad NMR peaks or no signal at all, and the diminazene signal is initially (after 1 h) much smaller than that of aceturate but, after 6 h, reaches about half of the aceturate amplitude. The linewidth of the diminazene peak in the nucleus is initially about twice as broad as that of aceturate and approaches the latter over time, while the linewidths of both molecules in the medium are nearly identical.

One possible interpretation would be that although diminazene penetrates the cell membrane earlier than aceturate as a result of higher permeability, a large portion of it is strongly bound, and only a small portion of diminazene molecules weakly bound to nuclear macromolecules gives the initial signal. When the binding reaches saturation, non-bound molecules dominate the diminazene signal in the nucleus. The aceturate signal after 1 h being nearly equivalent to that in the medium suggests that aceturate in the nucleus has already approached equilibrium with the medium at that time. The aceturate linewidth in the nucleus does not change, which can be understood in terms of constantly low macromolecule binding.

To understand the absence of diminazene signal in both the animal and vegetal cytoplasm, macromolecule binding has to be considered once more. The mitochondrial DNA quantity varies with species and cell type, and for a mature *Xenopus laevis* oocyte, it is several hundred times that of nuclear DNA (Shen and Bogenhagen, 2001). Furthermore, since transcription levels will remain low until the mid-blastula stage when development speeds up, the cytoplasm is stuffed with high amounts of maternal RNA (Bashirullah et al., 1998). Finally, proteins – which represent one third of the oocyte's dry mass, far exceeding the contribution of ribonucleic acids (Territo and Smits, 1998) – have been shown to bind large quantities of diminazene in other systems (e.g. Mamman et al., 1993). So the localised MR spectra are consistent with the assumption that all of the cytoplasmic diminazene would have been bound to macromolecules and thus give no MR signal.

The aceturate signal in the animal cytoplasm is much lower than that in the nucleus and increases only slowly. The linewidth, in turn, is broader in the animal cytoplasm than in the nucleus, but constant over time, which suggests that aceturate experiences faster diffusion in the nucleus than in the macromolecule-rich animal cytoplasm and that, although there is no strong macromolecule-binding of aceturate molecules, they are nonetheless restricted in their translational and rotational motions, resulting in a short spin-spin relaxation time and a correspondingly large linewidth. In the vegetal cytoplasm, the aceturate peaks are still smaller than in the animal cytoplasm, concordant with the vegetal cytoplasm being even more stuffed with maternal macromolecules (Danilchik and Gerhart, 1987; Bashirullah et al., 1998; Shen and Bogenhagen, 2001).

Delivery of drugs – including MRI contrast agents (Allen et al., 2004) –across cellular membranes is one of the main goals of current pharmaceutical research (Orive et al., 2003). It should be noted that the diminazene aceturate concentration used for the cellular uptake experiments is relatively high (250 mM) but still not even half a percent of the concentration of water which dominates the MR signal and thus had to be suppressed.

Furthermore, the spectroscopically investigated volume is to be taken into account – it is just $(200 \ \mu\text{m})^3$, or 8 nl. As the maximum size of a voxel that allows for intracellular spectroscopy in a *Xenopus* oocyte would be about $(600 \ \mu\text{m})^3$, this would result in the same SNR as the one obtained here if the drug concentration were to be reduced by a factor of 27 (i.e. down to about 7 mM). Hence, with reasonable SNR, even one or two milli-molar concentrations appear to be detectable non-invasively on a cellular level, rendering localised spectroscopy with *Xenopus* oocytes an attractive methodology to non-invasively determine the permeability of a cell for specific drugs, especially since the membrane of amphibian oocytes frequently serves as a broader membrane model (Horowitz, 1972; Kusano et al., 1977; Horowitz and Pearson, 1981; Dascal, 1987; Päuser et al., 1993).

Macromolecular binding, however, prevents an exact quantification of the drug concentration (especially at or near the lower detection limit), which would be required for a detailed kinetic analysis of drug uptake. The same issue arises with quantification of physiological constituents of the cell, e.g. the yolk. Further localised MRS studies probing membrane permeability of drugs or metabolites should thus seek to calibrate the individual intracellular spectra against data obtained in model membrane systems with known macromolecule concentrations.

As the SNR of NMR experiments increases with magnetic field strength, localised spectroscopy experiments at higher strengths could be promising because they could reduce the minimum detectable drug concentration in the cell. According to the simple $\omega^{\frac{7}{4}}$ law proposed by Hoult and Richards (1976), a 1.5 times SNR increase is expected betwen 14.1 T and 18.8 T. This can lower the detection limit of berenil to submillimolar if a whole cell is selected. The achievable voxel dimension is then mainly limited by the gradient eddy current charcteristics: as described above, for an identical voxel size, higher gradients are necessary in a higher magnetic field, inducing larger eddy currents.

In conclusion, the experiments presented here demonstrate that subcellular *in vivo* MR techniques provide interesting options to address cell biological and embryological as well as general developmental and pharmacological issues and provides alternatives to fixation, physical sectioning and staining, especially so in opaque systems. Likewise, longitudinal *in vivo* MR studies on cells and embryos offer new insights into the dynamics of three-dimensional morphological and biochemical patterning from the initial cleavages to germ layer formation to organogenesis. MR microscopic imaging and spectroscopy can thus be of significant help in broadening the experimental basis of comparative (Arendt and Nübler-Jung, 1999; Valentine et al., 1999; Valentine and Jablonski, 2003; Solnica-Krezel, 2005; Mathur, 2005) and theoretical (Meinhardt, 2001; Brodland and Veldhuis, 2002; Valles Jr., 2002; Longo et al., 2004; Prusinkiewicz, 2004) developmental studies. This is of special importance in model organisms like *Xenopus laevis*.

In view of later applications to dehydrated samples, the mechanisms discussed in 1 will reduce the image quality with respect to data acquired from dehydrated samples, and so the water ^{1}H MR images obtained here represent the upper limit of what is currently achievable in terms of spatial and chemical resolution. As for MRS, the water suppression technique employed to coax non-water contributions out of the ^{1}H MR signal can be regarded as an artificial means of dehydration, and the localised spectra demonstrate that much insight can be gained from such experiments. Their predictive capacity for solid state spectra is, however, limited, since further effects – mainly line broadening due to diploar interactions – complicate the picture. This will be illustrated by spectroscopic analyses of fossil and frozen samples in Chapters 4 and 5, respectively.

2.6. Outlook

Developmental studies, which initially contributed significantly to the formation of evolutionary biology as a new discipline, have recently returned to the agenda of the latter and spurred the symbiosis of the two fields to what is now called "Evolutionary Developmental Biology", or "evo-devo" (Baguñà and Garcia-Fernàndez, 2003; Gilbert, 2003). The rationale behind these developments is that comparative studies of developmental processes can – in a way similar to comparative genomic analyses (Meyerowitz, 2002; Blair et al., 2005) – shed light on phylogenetic relationships between the investigated species and clades, be they extinct (Xiao, 2002; Hughes, 2003; Valentine and Jablonski, 2003; Schmitt, 2005) or not (Arendt and Nübler-Jung, 1999; Solnica-Krezel, 2005; Song and Wessel, 2005).

This concept was beautifully illustrated by the work of D'Arcy Thompson who showed that mathematically simple transformations of suitably chosen coordinate systems can be used to warp the body plans back and fourth between related species (Thompson, 1917). Since then, multiple molecular mechanisms have been identified that can indeed account for transformations of this sort *in vivo* (reviewed in De Robertis and Sasai, 1996; Gerhart, 2001; Lall and Patel, 2001; Pourquié, 2003), and the first light has been shed on how these mechanisms might have evolved (Erwin and Davidson, 2002; Smith, 2003; Freitas et al., 2005). Considerable debate persists on what consitutes the biologically most meaningful reference frame for such matters (Solnica-Krezel, 2005; Gerhart, 2002) but in any case, 3D imaging modalities – especially if they are non-invasive – will be very helpful in acquiring the necessary data (Schatten and Donovan, 2004), both within and across taxa. Chapters 4 and 5 will provide some further examples for that.

Chapter 3. Safety aspects of Magnetic Resonance Microscopy

3.1. Summary

Objectives Strong magnetic fields as those required for microscopic MR imaging and localised MR spectroscopy have frequently been reported to interfer with cellular physiology. However, the evidence gathered so far is equivocal. The cleavage plane alterations observed in the previous chapter will therefore be analysed in more detail here.

Methods A review of the available literature suggests that part of the inconsistencies might be resolved by considering a new parameter for morphological alterations induced by magnetic fields – the jelly layers that normally surround the amphibian egg and are often removed in laboratory studies for easier cell handling. To experimentally test this hypothesis, fertilisable *Xenopus laevis* eggs and early embryos with and without jelly coat were exposed to static magnetic fields of up to 9.4 T for different periods of time and their morphology compared with the *Xenopus* Normal Table which is based on jelly-bearing eggs only exposed to the geomagnetic field.

Results Embryos developing from dejellied eggs showed an alteration of the third and consecutive cleavage planes with respect to the Normal Table. In contrast to earlier reports, though, the effect did not depend upon magnetic field exposure but on the absence of the jelly coat. Similarly, a complex reorganisation of cortical pigmentation was found in dejellied eggs as a function of the magnetic field and the field exposure time. Initial pigment rearrangements could be observed at about 0.5 T, and less than 3 T are required for the effects to fully develop within two hours. No effect was observed when the jelly layers of the eggs were left intact.

Conclusions These results suggest that the action of magnetic fields on *Xenopus* oocytes and embryos might involve cortical pigments or associated cytoskeletal structures normally held in place by the jelly layers and that the presence of the jelly layer should indeed be included in further studies of magnetic field effects in this system.

3.2. Review of previous studies

Magnetic fields can alter cellular physiology via a number of mechanisms, including the facilitation of radical formation, interference with ion or side chain mobility as well as susceptibility-driven orientation effects of macromolecules (for review, see Rosen, 2003; Schenck, 2005). They have also been proposed to play morphogenetic roles in embryo-genesis as well as tissue neoplasm and regeneration (Levin, 2003).

As described in Section 2.4.1 (on page 32), the third and consecutive cleavage planes of embryos developing in the magnet during MRI experiments were altered with respect to the *Xenopus laevis* Normal Table (a detailed description of the developmental stages under physiological conditions, prepared by Nieuwkoop and Faber, 1956). The phenomenon has been observed in high magnetic fields before (Denegre et al., 1998; Valles Jr., 2002; Valles Jr. et al., 2002) and was attributed to a geometric reorientation of the centrosome replication and spreading cycle in response to a field-induced realignment of the mitotic spindle before the second cleavage (Valles Jr., 2002; Valles Jr. et al., 2002). While the proposed mechanism is partly compatible with the MRM series presented in 2.4.1, it fails to explain why the fourth cleavage in Fig. 2.2 would occur horizontally. One possible reason for this could be that, contrary to the model's assumptions (Valles Jr., 2002), the role of cell shape – which is affected by dejellying – in cleavage plane determination can not be neglected.

This interpretation receives support from other experimental (Black and Vincent, 1988; Chalmers et al., 2003) and theoretical (Brodland and Veldhuis, 2002) studies but it has never systematically been tested, even though magnetic field effects on amphibian development have been reported in several instances since the hatching rate of embryos of the frog *Rana pipiens* subjected to the field of a 1 T permanent magnet was found to be reduced (Neurath, 1968). The effects observed in *Xenopus laevis* ranged from reduced tadpole pigmentation at 1 T (Ueno et al., 1984) to cleavage plane alterations between 1.7 T and 17 T (Denegre et al., 1998) to no anomaly at all (Mild et al., 1981; Kay et al., 1988; Ueno et al., 1990, 1994).

A closer look at these results reveals, however (cf. Table 3.1), that magnetic field effects were only observed after dejellying (Ueno et al., 1984; Denegre et al., 1998; Iwasaka et al., 2001)[*], with the effects ranging from altered pigmentation in tadpoles at 1 T (Ueno et al., 1984) to cleavage plane reorientation in embryos developing in fields between 1.7 T and 17 T (Denegre et al., 1998; Iwasaka et al., 2001).

---

[*]Dejellying was not mentioned by Iwasaka et al. (2001) but can be inferred to have taken place before magnetic field exposure, i.e. within 20, 30 or 50 min after fertilisation (for which it is required, cf. Hedrick and Nishihara, 1991). It remains unclear whether zero-field control eggs were dejellied.

Table 3.1.: Correlation of magnetic field effects and the presence of the jelly

Magnetic field effects on *Xenopus* as reported in the literature

Field[a]	Magnet[b]	Jelly removed	Effect	Ref.
0	none$_{no}^{no}$	no	no	Nieuwkoop and Faber (1956)
0.25	E$_{no}^{no}$	no	no	Mild et al. (1981)
1.0	E$_{yes}^{yes}$	yes and no[c]	more embryos abnormal	Ueno et al. (1984)
1.5	SC$_{yes}^{yes}$	no	no	Kay et al. (1988)
6.34	SC$_{no}^{no}$	yes[d]	no	Ueno et al. (1990)
8	SC$_{no}^{yes}$	no	no	Ueno et al. (1994)
10	SC$_{no}^{yes}$	yes[e]	cleavage plane reorientation	Iwasaka et al. (2001)
14.1	SC$_{yes}^{yes}$	yes	cleavage plane reorientation	Section 2.4.2 in this thesis
14.1	SC$_{yes}^{yes}$	yes[f]	no	Section 2.4.3 in this thesis
17	SC$_{no}^{no}$	yes	cleavage plane reorientation	Denegre et al. (1998)

[a]Maximal field strength in T.

[b]Types of magnets: E = electromagnet; SC = superconductor. Superscripts denote the application of field gradients, subscripts indicate radiofrequency pulsing as in MR experiments.

[c]The experiments were mainly performed on cysteine-dejellied eggs but jelly-coated embryos were mentioned to give essentially the same results.

[d]Eggs were dejellied not immediately after fertilisation but about 1 h later. Description is ambiguous on whether field exposure started before or after dejellying.

[e]Dejellying is not mentioned but can be inferred from the figures to have been performed on the field-exposed embryos.

[f]prophase-I-arrested stage VI oocytes, not fertilisable

The jelly coat

Spawned amphibian eggs are surrounded by a multi-layered jelly coat that serves several functions: First, it sticks the cells together and glues them to their substrate to ensure stable positioning even in flowing environments. Second, it induces the acrosomal reaction that prepares the sperm for insemination and helps to inhibit polyspermy. Third, it provides a barrier for ionic or microbiotic stress and fourth – together with a cytoskeletal mesh of actin filaments and microtubules beneath the plasma membrane – an extracellular skeleton (Gilbert, 2000; Podolsky, 2002; Sardet et al., 2002).

Xenopus laevis spawns and fertilises its eggs in hypotonic waters where jelly coat loss causes osmotic stress that may result in organelle perturbation, especially during the rapid initial cleavages that occur every 40 min at 21°C. Though axis formation and embryonic development in *Xenopus* do not require Earth gravity (Neubert et al., 1998), maintaining an orientation which exposes the dark animal hemisphere to predators from above and the light vegetal hemisphere to predators from below certainly increases the chances of survival. This is achieved by gravitational orientation of the embryo which can freely rotate inside the jelly coat that sticks it to the substrate, typically grass or leaves.The stickyness, however, complicates cell handling, and removal of the jelly coat has therefore become common practice (Freeman, 1968; Gusseck and Hedrick, 1971; Yurewicz et al., 1975; Wolf et al., 1976; Ubbels et al., 1983; Ueno et al., 1984; Ueno et al., 1990; Denegre et al., 1998; Iwasaka et al., 2001).

3.3. Experimental procedures

3.3.1. Oocyte and embryo preparation

Mature *Xenopus* frogs of both sexes were maintained under physiological standard conditions, as described in section 2.3, with the following slight modifications: The amount of HCG (Sigma-Aldrich, Germany) injected varied between 500-1.200 IU, the eggs were spawned directly into isotonic modified Barth's medium (MBM; Richter and Bauer, 1990) and dejellied with 2 % of cysteine chloride (VWR International, Darmstadt, Germany) in MBM. Only freshly spawned fertilisable eggs were used, and the whole batch obtained from one female was either dejellied or not and either fertilised or not. All experiments have been carried out according to institutional ethical guidelines at IBMT and the University of the Saarland.

3.3.2. Magnetic field exposure

To expose eggs of the same batch to different field strengths at the same time, they were distributed in groups of roughly 100 to Petri dishes of 65 mm outer diameter that were placed in a rack with 24 equidistant storeys (cf. Fig. 3.1). The rack was then slowly (with about 3 mm/s) inserted into the shim system of the vertical superconducting magnet of the DMX 400 NMR spectrometer (Bruker, Rheinstetten, Germany) at IBMT. The magnetic flux density (commonly referred to as magnetic field strength) in the rack varied between 0.5 T and 9.4 T. Control eggs (zero field references) both with and without jelly coat were placed approx. 8 m from the magnet (about 70 μT Earth's field strength) under otherwise identical conditions.

When third cleavage was completed, the embryos were taken out of the magnet and – along with the controls – fixed with 2.5 % glutaraldehyde in MBM before finally being classified according to their number of vertical third cleavages (as in Denegre et al., 1998). Results were pooled from three experiments with jelly coat and from four experiments with dejellied embryos. Embryos which had not completed the second cleavage at the time of fixation or which had already completed fourth cleavage were not included in the statistics. Temperature was kept at $(21 \pm 1)°$C throughout the experiments.
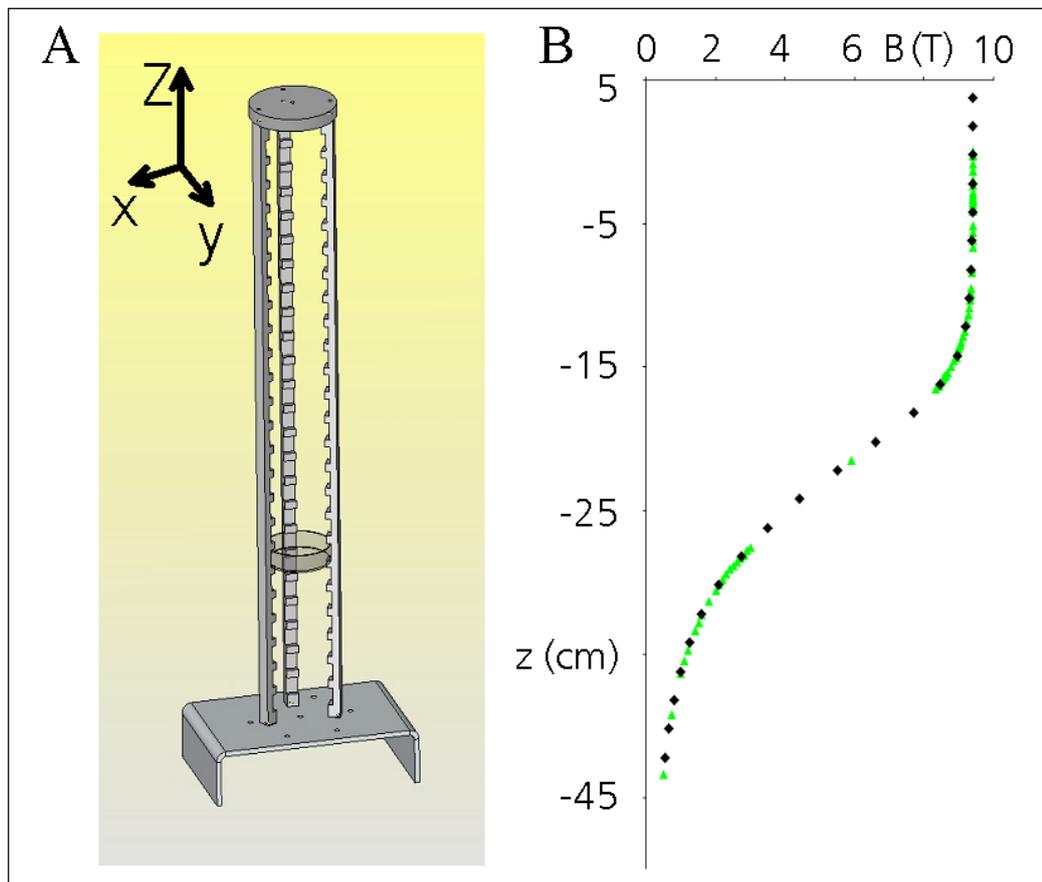

Figure 3.1.: Magnetic field exposure. (A) The rack in which the Petri dishes with the cells were positioned. z direction is the direction of the static magnetic field (courtesy of Martin Benecke). (B) Characterisation of the magnetic field. Green triangles represent measured field strengths, blue diamonds indicate the field strengths at the respective positions in the rack.

3.4. Results

3.4.1. Cell division in the magnet

Control embryos with intact jelly coat and not exposed to the magnetic high-field almost exclusively followed the prototypic description given by Nieuwkoop and Faber (1956) in the Normal Table: They showed four horizontal third cleavages and were thus assigned Type 0 because of their lack of vertical cleavages (cf. Fig. 3.2A). Type IV embryos in which all four third cleavages are vertical did not occur below 4.50 T but the overall incidence was too low to regard this as significant. At higher magnetic field strengths, the number of observed vertical cleavages increased slightly but no significant difference could be found between field strengths of 1.00 T and 9.40 T, which are one order of magnitude apart and should hence allow to detect field-dependent effects.

Interestingly, embryos that had already entered their fourth cleavage at the time of fixation often showed a horizontal fourth division plane if the third one had been vertical, concordant with the observations reported in Section 2.4.1.
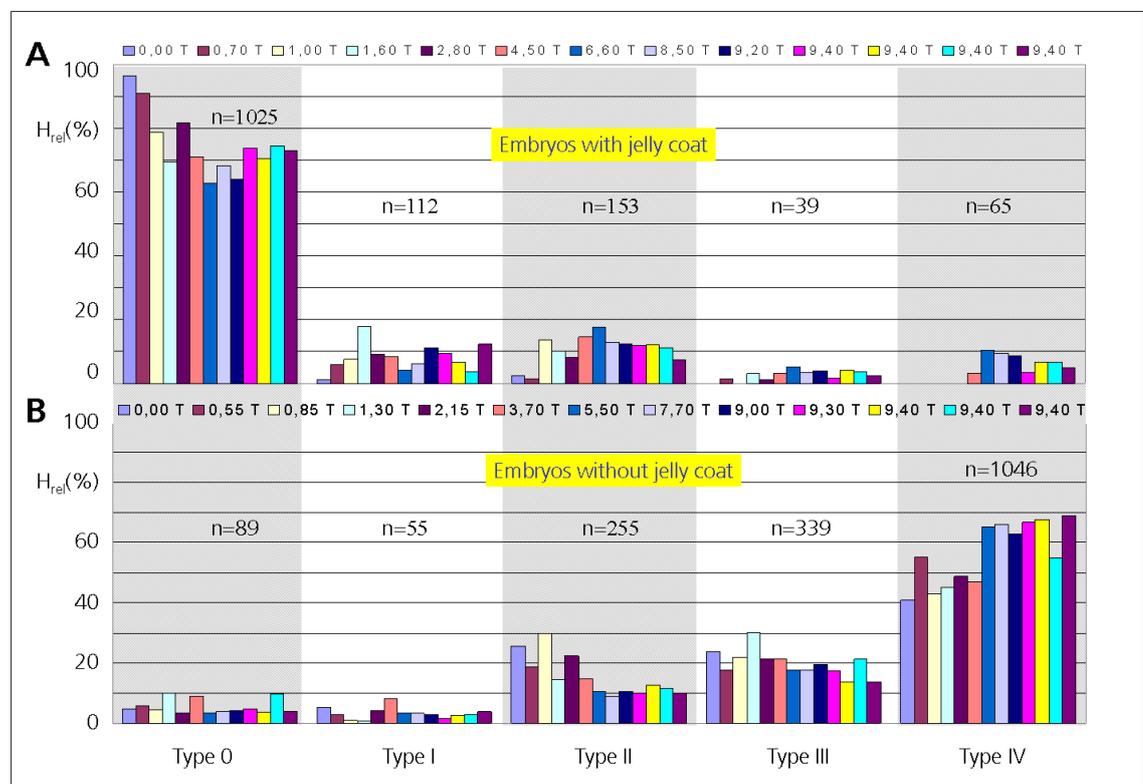

Figure 3.2.: The occurance of vertical third cleavages as a function of field strength in 1394 *Xenopus* embryos developing with their jelly coat (A) and 1784 without (B). The Arabic numeral represents the sum of all embryos that showed the number of vertical third cleavages (normally and minimally zero, maximally four) given by the Roman numeral.

The third cleavage plane of dejellied embryos exposed to the magnet was usually reoriented with respect to the Normal Table (cf. Fig. 3.2B), as previously described (Denegre et al., 1998; Valles Jr., 2002; Valles Jr. et al., 2002). In sharp contrast to those studies, however, the effect appeared not only under high-field conditions but also in controls only exposed to the Earth's magnetic field. Again, as with the non-dejellied embryos, no dependence on the magnetic field strength was detectable, though a tendency exists towards the direction advocated by Denegre et al. (1998).

3.4.2. Pigment pattern in the egg cortex

A typical control egg with intact jelly coat and no exposure to the magnetic field is depicted in Fig. 3.3A, appearing as described in the literature (Nieuwkoop and Faber, 1956). Removal of the jelly coat does not alter the egg's phenomenology, which is essential for the popularity of dejellying procedures (Gusseck and Hedrick, 1971; Yurewicz et al., 1975; Wolf et al., 1976; Merriam et al., 1983; Ubbels et al., 1983; Ueno et al., 1984; Ueno et al., 1990; Denegre et al., 1998). Field-exposed eggs with jelly coat are visually indistinguishable from those of the kind depicted in Fig. 3.3A.

However, cells without jelly coat that were subjected to fields above 0.5 T showed a two-phase pigment redistribution with respect to the zero-field controls: In the first phase (TBE I), the white band characteristic of stage VI oocytes and fertilisable eggs concentrically descended from its usually equatorial position towards the vegetal pole (Fig. 3.3B), while the second phase (TBE II) is characterised by a tongue of this white band moving towards the animal pole (Fig. 3.3C), with a final arrangement (Fig. 3.3D) reminiscent of the seam topology of a tennis ball (Fig. 3.3E). This upward moving tongue was always aligned with the main axis (z) of the magnetic field but randomly oriented in the x-y plane (Fig. 3.3F). The TBE appeared irreversible and was exclusive to but ubiquitous in dejellied field-exposed fertilisable eggs.

In order to monitor the temporal evolution of the TBE, the cells were taken out of the magnet at regular intervals (after 15, 29, 42, 63 and 76 min of cumulative exposure time) to determine the TBE frequency in the individual dishes (cf. Fig. 3.4A). As the distinction between TBE I, TBE II and no TBE requires closed inspection of each individual cell and is thus time-consuming, only the easily recognisable late TBE II were considered, so that the rack could be repositioned in the magnet after about 10 min. The results reveal that the TBE II frequency depends on exposure time in a sigmoidal way and that a critical threshold just above 1 T is required for TBE II to occur, while all groups exposed to field strengths above 3 T reached essentially the same TBE II percentage after 76 min of exposure to the field.
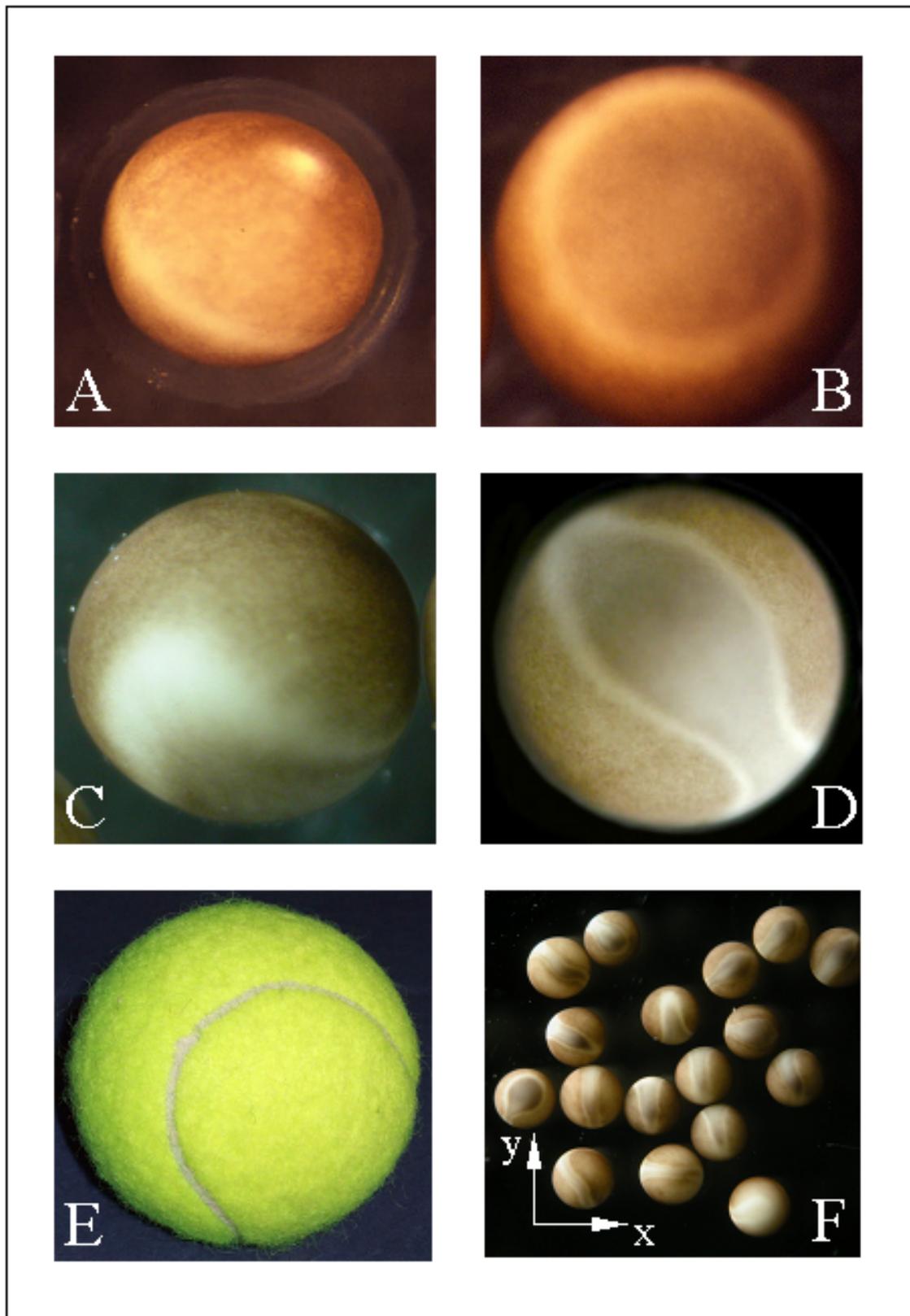
Figure 3.3.: (A) Jelly-coated egg not exposed to the magnet. The overall appearance and the pigmentation pattern are indistinguishable from the jelly-coated eggs exposed to the magnet and from the dejellied controls not exposed to the magnet. Note the position of the white equatorial line. (B-D and F) Cysteine-dejellied eggs after exposure to the magnet, with altered cortical pigmentation. (B) Vegetal view of a late TBE I, with the equatorial line descended towards the vegetal pole. (C) Lateral view of an intermediate TBE II, showing the tongue that reaches out from the descended equatorial line. (D) Animal view of late TBE II, with the tongue from the equatorial line having reached the animal pole. (E) Tennis ball. (F) Orientation of the TBE in the magnetic field. The magnetic field's central axis (z) was perpendicular to the image plane. The images in (A), (C-D) and (F) were taken prior to and the one in (B) after fixation.

Interestingly, the eggs placed between 4.4 T and 8.5 T – i.e. those exposed to the highest gradients of the static magnetic field – showed a tendency to develop TBE II more quickly and more frequently, though this was not significant due to the relatively high standard deviation of the TBE counts.

To eliminate the possibility that the repetitive insertion and removal of the rack exerts additional gradient-induced stress on the eggs, another experiment was performed in which they were continuously kept in the magnet for 109 min and then directly fixed. To further disambiguate between potential field strength and field gradient strength effects, pairs of Petri dishes with eggs were distributed to storeys of the rack such that both were placed at equal (or, in one case, similar) gradient strengths but one of them at a high, the other at a low field strength. Field strength and gradient strength could not be varied independently in the setup.

The results (cf. Fig. 3.4B) show that although differences exist in TBE percentages between high field and low field at gradient strengths below about 0.2 T/m, these mainly reflect the transition between TBE I and TBE II and do not affect the sum of both TBE percentages. TBE II generally requires just over 1 T to occur, independent of gradient strength, whereas the threshold for TBE I was about 0.5 T. The difference in TBE II percentages between the experiments in Fig. 3.4A and Fig. 3.4B can be accounted for by the inclusion of early TBE II in the latter, while the higher standard deviations in Fig. 3.4A result from the impossibility of detailed inspection of individual cells due to time limits, which was not the case with the fixed samples.

3.5. Discussion

The observations reported here on embryonic cleavages in dejellied embryos can not be reconciled with the idea (Denegre et al., 1998; Valles Jr., 2002; Valles Jr. et al., 2002) that magnetic fields exert a major influence on cleavage plane determination. Considering instead that embryos dejellied 1 h after fertilisation had shown no effect of exposure to 6.34 T fields (Ueno et al., 1990), it seems plausible that the magnetic field effects reported in (Valles Jr. et al., 2002) and attributed to field exposure time could alternatively be explained by supposing that cleavage plane alterations are determined by the time the embryo spent in a dejellied state.

This view is in line with the initial hypothesis derived from the literature survey (cf. Table 3.1) – the interplay between the jelly coat and its underlying extra- and intracellular layers (the vitelline envelope and the plasma mambrane, respectively) mediate the action of magnetic fields in *Xenopus laevis*.
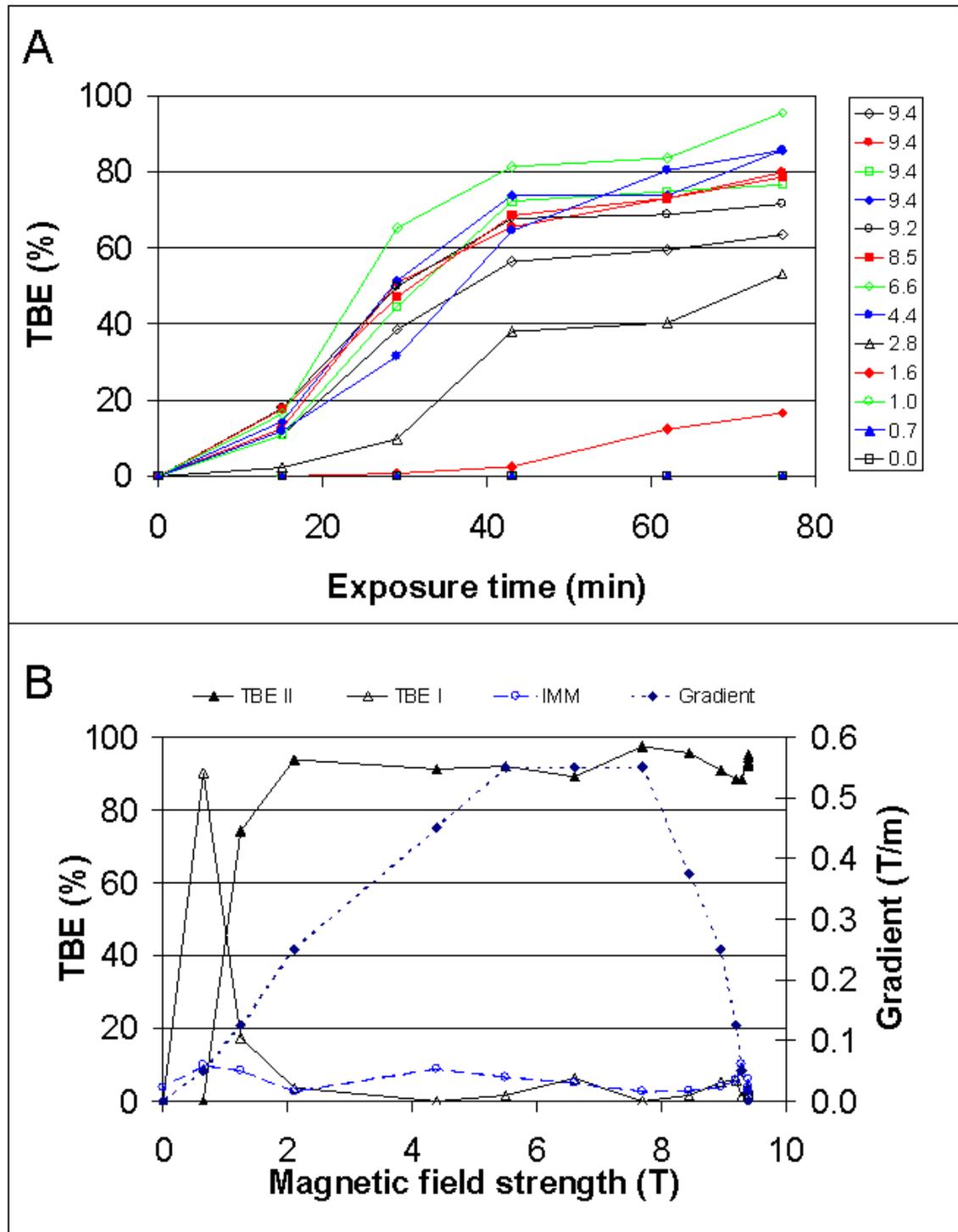
Figure 3.4.: The frequency of TBE in two populations of cysteine-dejellied fertilisable *Xenopus* eggs as a function of field strength, gradient strength, and magnet exposure time. (A) Temporal evolution of TBE II at different field strengths (in T). The diagram only gives field exposure times. The total duration of the experiment was about 50 min longer. Each individual point in the diagrams represents a group of about 150 cells. The standard deviation in TBE count, as determined from the four Petri dishes positioned at 9.4 T field strength in the center of the magnet, was 12.3 %. A total of about five percent of the eggs obtained from one ovulation were nekrotic. These were not considered when calculating TBE percentages. (B) TBE percentages after 109 min of continuous magnetic field exposure as a function of field strength and field gradient strength. The TBE counts were all performed after fixation of the eggs, and the standard deviation in the four central dishes was 0.7 % for TBE I and 1.2 % for TBE II. IMM = percentage of immature oocytes present in the dish.

It is also compatible with earlier findings that cleavage furrowing depends upon cell shape (Ubbels et al., 1983; Black and Vincent, 1988; Brodland and Veldhuis, 2002; Shuster and Burgess, 2002; Chalmers et al., 2003) and with the cortical pigment reorganisation observed in dejellied eggs.

The pigmentation – melanin granula closely linked to the cortex (Merriam et al., 1983) – served here as a visual indicator for a reorganisation of the cortex. However, the melanin might well be responsable for the effect, since it resembles vertebrate pigments discussed in relation to magnetoreception at Earth's field strength (Ritz et al., 2000).

As for *Xenopus*, the involvement of pigments in such rearrangements fits with earlier reports of increased pigmentation anomalies in tadpoles subjected to static fields of 1 T (Ueno et al., 1984). In turn, the occurance of TBE in *all* fertilisable eggs without jelly coat above 3 T but not in prophase I-arrested oocytes at 14.1 T (cf. Section 2.4.2) points at a passive reaction to the magnetic field and suggests the involvement of structures or pathways in the oocyte that are not present before maturation and normally kept in place by or with the help of components of the jelly coat. The cortical rearrangements leading to the TBE probably go along with a redistribution of sperm receptors, which might impede fertilisation. However, this could not be tested, as fertilisation requires the jelly coat (Hedrick and Nishihara, 1991).

Embryos developing with or without jelly coat did not show any difference due to magnetic field exposure but solely on the basis of these results, it can not be decided whether the cortical pigments or their anchorage in the cortex are modified by fertilisation or whether the quick cortical reorganisations normally accompanying fertilisation and embryonic cleavage simply dominate over the passive movements of the pigment granula.

The way in which the jelly coat was removed could also influence the pronounciation of magnetic field effects. Five major approaches have been proposed to achieve it in a way useful for further biological studies of the eggs (Gusseck and Hedrick, 1971): Mechanial removal, UV irradiation, alkaline or enzymatic digestion or disulfid-reducing reagents. The first one is too time-consuming for the thousands of eggs necessary for our experiments, and the following three do not specifically act on the jelly coat. This problem concerns the last group as well (Gusseck and Hedrick, 1971; Wolf et al., 1976; Merriam et al., 1983; Ueno et al., 1984; Ueno et al., 1990; Yurewicz et al., 1975) but we chose cysteine dejellying because it provides a relatively soft approach (Gusseck and Hedrick, 1971): It can reliably be stopped before attacking the vitelline envelope. Possibly, though, cysteine actions beyond jelly lysis might contribute to the TBE, and further studies should seek to incorporate dejellying mechanisms in the assessment of magnetic field effects.

3.6. Outlook

The magnetic-field dependent cortex reorganisation in fertilisable eggs of *Xenopus laevis* appears to be mediated by the cortical pigment molecules, suggesting that pigmentous structures in other systems might exert similar roles. A detailed understanding of the mechanisms underlying such effects in model systems can provide better estimates of possible biological limitations on the applicability of high magnetic fields to cells, tissues and organisms, including humans. In this respect, it is important to note that the minimum field strengths required for TBE I onset and for TBE II saturation, respectively, coincide with the current lower and upper limits of typical clinical magnetic resonance studies (Schreiber et al., 2001). Therefore, further research on routine or long-term exposure of pigmented biological tissue to strong static magnetic fields is necessary. *Xenopus*, once more, has proven a suitable test system, as it provides for both field-sensitive and field-insensitive eggs, depending on the simple removal of the jelly coat.

Chapter 4. Magnetic Resonance Microscopy of Fossils

4.1. Summary

Objectives   Fossilisation preferentially occurs in specimens that performed *in vivo* biomineralisation, i.e. a compaction of inorganic and organic compounds, some of which might survive over diagenetic periods. From a MR perspective, the ^{1}H nuclei of such organic groups could possibly compensate, at least in part, for the dramatic signal loss due to dehydration. In this case, fossils could potentially serve as a test system for investigations in systems where organic and inorganic matter are heavily compacted, as is the case with frozen biological materials. With respect to them, fossils have the additional advantage that metabolism and recrystallisation do not occur on the time scales relevant for MRM, which will be attempted here.

Methods   Three-dimensional MR images were acquired from a series of normal and pathological belemnites from different diagenetic backgrounds. The study was then extended to a broad taxonomic variety, ranging from invertebrates to vertebrates and plants. In addition, ^{1}H and ^{13}C MAS MR spectra were recorded from a belemnite to clarify the molecular origin of the MR signal.

Results   Belemnites can routinely be imaged by MRI, and the achievable microscopic resolutions around or below 100 μm allow the deduction of palaeopathological scenarios ranging from endoskeletal fractures to inflammation. The MR signal, though featuring small organic contributions, is mostly due to residual water and strong enough to allow MRI of most animal and plant clades that have been tested. Besides factors relating to biomineralisation, diagenetic parameters also impact on the achievable signal intensity.

Conclusions   MRI of fossils is feasible with current technology and can be expected to yield substantial new insights into fossilisation, palaeoecology, evolution and biomineralisation.

4.2. Review of previous studies

Every fossil is unique – not only in the sense that the life of the being it stems from was unique but also with respect to the taphonomic and diagenetic processes the remains were subjected to and, perhaps, with regard to the circumstances of its discovery, handling and storage. Specimen interpretation has to take into account these individual features in order to meaningfully place it within the context of other findings.

When an organism dies, it is usually quickly decomposed but special conditions – namely the presence of extended mineralised structures – sometimes allow for part of its morphological or biochemical characteristics to be preserved (for reviews, see Behrensmeyer et al., 2000; Briggs, 2003; Weiner and Dove, 2003). Though these conditions only apply to a tiny minority of individual life forms at a given time, vast amounts of biogenic deposits have been accumulated over geological times, most famously perhaps in the form of sedimentary rock which bears various types of fossils (Albrecht and Ourisson, 1971; Poinar et al., 1993; Poinar Jr. and Poinar, 1999; Kidwell and Holland, 2002; Behrensmeyer et al., 2000; Briggs, 2003) that can also turn into fossil fuels (Brocks et al., 1999; Vandenbroucke, 2003). Fossils were often found to contain organic matter, especially in biomineral matrices like in cephalopod shells (Westbroek et al., 1979), belemnite rostra (Bandel and Spaeth, 1988; Florek et al., 2004), bones (Schweitzer et al., 2005), or wood (Boyce et al., 2001; Siurek et al., 2004).

Such observations led to the suggestion (e.g. Keilin, 1959; Weiner et al., 1976; Westbroek et al., 1979; Eglinton and Logan, 1991; Engel et al., 1994) that part of the organic material detected in fossils might actually represent the most stable portion of the molecules originally constituting the individual at the time of its death, which opened the door for biochemical contributions to palaeotaxonomy (Blumer, 1965; Albrecht and Ourisson, 1971; Niklas and Gensel, 1976; Westbroek et al., 1979; Ourisson and Nakatani, 1994; Waggoner, 2002; Schweitzer, 2003; Pääbo et al., 2004; Rogaev et al., 2006).

Chemical analyses, however, generally consume the specimens or parts thereof, thus reducing the morphological information they contain (Albrecht and Ourisson, 1971; Sælen, 1989; Schweitzer et al., 2005). On the other hand, serial grinding techniques combined with digital photography allow to reconstruct the three-dimensional structure of fossils (Luo and Eastman, 1995; Luo and Marsh, 1996; Sutton et al., 2001; Siveter et al., 2004; Sutton et al., 2005). Unfortunately, this achievement is traded for a complete loss of the specimen, which imposes severe limits on the applicability of the method to investigations of rare specimens, amongst which fossils with pathological alterations undoubtedly form a prominent group. Therefore, it is important to explore the potential of non-invasive techniques to contribute to the characterisation of fossil evidence.

4.2.1. Non-invasive fossil imaging

Obtaining chemical and spatial information from the same specimen became possible by using x-ray computed tomography (CT) to construct non-invasive 3D representations at microscopic resolution of porous or otherwise heterogeneous fossils (e.g. Fisher et al., 2000; Zollikofer et al., 2002), which keeps the specimens intact and does not prevent subsequent analyses. Furthermore, Neutron Tomography (NT) has recently been demonstrated to allow for the non-invasive reconstruction – at a spatial resolution comparable to the one achievable with CT – of three-dimensional morphology in sauropod vertebrae (Schwarz et al., 2005), and its spectroscopic sister technique can provide some basic chemical information (Gabel et al., 2002).

As demonstrated in Chapter 2 of this thesis, Magnetic Resonance techniques can deliver both spatial and chemical resolution in living tissue. Though the geosciences are much more concerned with the study of minerals, [1]H-rich fluids like water and oil play nonetheless an important role, and so MR spectroscopic techniques have found a multitude of applications in sedimentology (Rothwell and Vinegar, 1985; de Swiet et al., 1998; Song et al., 2000; Dria et al., 2002; Westphal et al., 2005). In parallel, they also gained popularity in neighbouring fields, such as environmental engineering (Lens and Hemminga, 1998), materials science (Smith and Strange, 1996), archeology (Lee et al., 1995; Ghisalberti and Godfrey, 1998; Lambert et al., 2000), anthropology (Spoor et al., 2000; Borah et al., 2001) and palaeontology (Lambert and Frye, 1982; Bates and Hatcher, 1989; Almendros et al., 2005), suggesting that MR images of geological samples are in principle possible and only technically limited by the fast T_2 relaxation typical for solids.

In consequence, such MRI studies initially took a rather indirect approach by using cavities artificially filled with water or crude oil to generate negative images of fossil bone (Sebes et al., 1991), sandstone (de Swiet et al., 1998) and mouldic fossils (Clark et al., 2004). However, intrinsic contrast – primarily due to residual water – could also be used to record MR images of hydrous minerals (Nakashima et al., 1998), sea ice (Callaghan and Eccles, 1996; Eicken et al., 2000), and rocks (Borgia et al., 2000; Gingras et al., 2002; Westphal et al., 2005). Therefore, this study was designed to investigate the potential of MRI to image the three-dimensional morphology of fossils, with special emphasis on pathologically altered ones, and to test the resolution limits.

4.2.2. Palaeopathology

Palaeopathological studies can shed light on the ecology of ancient life forms, on climate change and on the functional significance of morphological traits (Keupp, 1984, 1985).
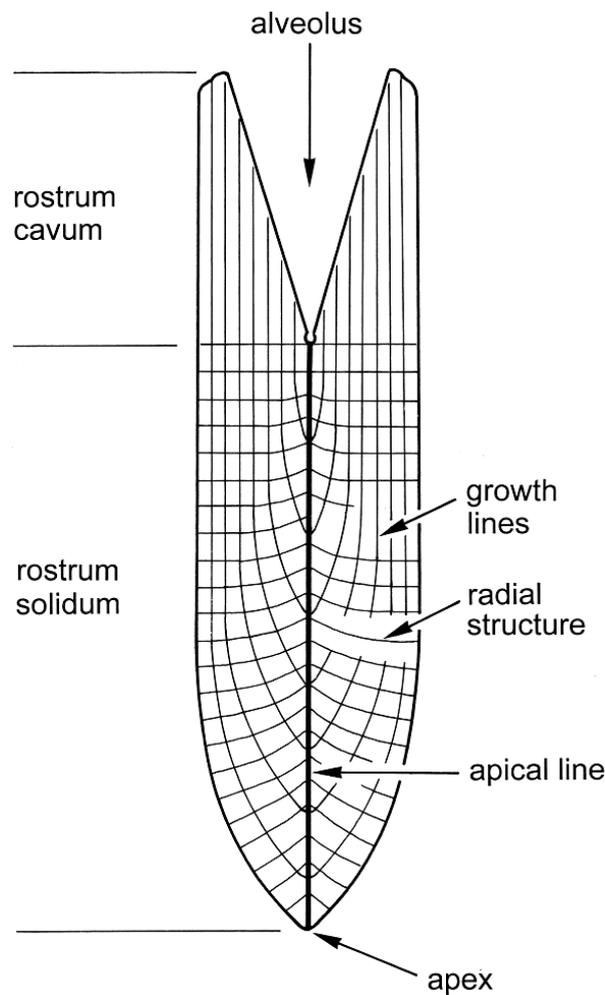
Figure 4.1.: Schematic of the anatomy of a belemnite guard (longitudinal section), showing the rostrum cavum, the rostrum solidum and the central channel (courtesy of Martin Aberhan)

Most of the described palaeopathological phenomena of fossil hard parts arose from interactions between different species (e.g. through predation or parasitism). The specific reaction of the organism under attack led to a characteristic syndrome often manifesting itself in anomalous growth patterns that can still be observed in fossil remains. The resulting degree of alterations in morphology always ranges within specific tolerance limits and allows to estimate the functional relevance of distinct morphological features.

Within a wealth of palaeopathological studies, most focus on vertebrates (cf. Tasnádi-Kubacska, 1962) but considerable efforts have also been directed towards pathological aspects of invertebrates. Descriptions and interpretations of anomalies in skeletons of endocochleate cephalopods, in contrast, appear only sporadically. The reason for the different treatment of endo- and ectocochleate specimens is of a very practical nature: The shells of ectocochleate cephalopods allow an immediate diagnosis of sublethal injuries or other growth disturbances and of the subsequent formation of characteristic syndromes by the attacked animal. One notable exception to the rule are healed fractures in belemnite guards, which have received frequent attention (see Keupp, 2002, and references therein).

Belemnites formed a now extinct group of decabrachiate cephalopods, related to the extant coleoids. They had an endoskeleton whose most distal part – the rostrum or guard – is frequently preserved. As illustrated in Fig. 4.2.2, it consists of the rostrum cavum with the alveolus – a conical cavity at the anterior portion that helped to maintain a horizontal swimming posture (Naef, 1922) – and the rostrum solidum (e.g. Sælen, 1989, Fig. 1). It is further characterised by (i) the apical line, which represents the axis of the rostrum and marks the trajectory of the apex (the most posterior part of the rostrum) during successive growth stages, (ii) composite radial structures formed by crystals of low-Mg calcite radiating out from the apical line to the outer border of the rostrum, and (iii) concentric growth lines (or growth rings) which stem from periodical accretions of radial structures that resulted in spatial variations of the organic content. This variation is often subtle, so that growth rings may be difficult to define (Sælen, 1989).

Apart from the primordial rostrum and very early growth stages, the original mineralogy of belemnite rostra was low-Mg calcite (Veizer, 1974). As such, they are relatively stable even under freshwater influence (meteoric diagenesis). The microstructure consists of regular, fine prisms with parallel crystal axes, arranged in well-ordered prismatic layers (Bandel and Spaeth, 1988) which can still be discerned in even strongly recrystallised specimens. Diagenetic exchange between rostra and enclosing rock appears to be limited (up to about 10% by weight, according to Veizer, 1974) and may be caused by solution-precipitation phenomena or filling of the pore space which was either primary or diagenetically generated by the decay of organic matter. Growth lines are frequently preserved.

With respect to ^{1}H sources in belemnites, Westbroek et al. (1979) analysed rostra of two late Cretaceous taxa, *Gonioteuthis* and *Belemnitella*. In the water-soluble macromolecular fraction of well-preserved *Gonioteuthis* rostra, these authors identified a mix of peptides and saccharides as well as an amino acid composition very similar to that of *Nautilus* and dominated by glycine and alanine. Even original antigenic properties of certain fractions were still preserved. Westbroek et al. concluded that the biochemical materials derived from *Gonioteuthis* were original belemnite compounds which only experienced minor alterations during diagenesis. The observed enrichment in polyphenols may be due to reactions between peptides and carbohydrates during diagenesis. In contrast to the exceptionally well-preserved rostra of *Gonioteuthis*, Westbroek et al. found that those of *Belemnitella* were strongly recrystallised. Although the amino acid composition is similarly dominated by glycine and alanine, less stable (threonine, serine, arginine) and even very labile amino acids (methionine) were also present. Together, this led to the conclusion that the primary organic composition of the *Belemnitella* rostra was contaminated during or after recrystallisation by percolating ground water (Westbroek et al., 1979).

Deformations of belemnite guards can result either from diagenetic, tectonic and impact events after the death of the organism or, during its life time, from illness or antibiotic interactions (predator-pray relationships, parasitism). Specimens of the latter group are commonly dubbed pathological. They were first described and interpreted by Duval-Jouve (1841) in sliced rostra with fractures. First attempts to extract evidence for behavioural traits of belemnoid animals from pathologic guards were made by Abel (1916) who attributed the rostral fractures described by Duval-Jouve to damage experienced when the animal used its posterior end as a digging tool, (rather than to an unsuccessful attack by a predator), which led him to propose that they lived on the sea floor.

However, cuttlebone growth disturbances in modern cuttlefish living in their natural habitat are mostly triggered by repair of sublethal injuries as a consequence of unsuccessful attacks of predators (including human divers von Boletzky and Overath, 1989). Correspondingly, it may be expected that many anomalous guards of belemnites reflect the repair of similar damages to the preadult rostrum or its muscular mantle. Nonetheless, it has been shown that – besides such exogenous traumatic events – remarkable anomalies also resulted from endogenous disturbances of the mantle tissue, including presumed cases of parasitism (Radwánska and Radwánski, 2004).

4.3. Experimental approach

4.3.1. Fossil material

Invertebrates

The fossil locality of Tendaguru, famous for its diverse dinosaur assemblages, is located approximately 60 km northwest of the seaport of Lindi in southeastern Tanzania. The Late Jurassic to Early Cretaceous Tendaguru Beds reach a thickness of 110 m and consist of three fine-grained dinosaur-bearing sequences which are intercalated with sandstone-dominated sequences containing a predominantly marine fauna (Aberhan et al., 2002). The analysed belemnite rostra, identified as *Belemnopsis* sp. by Dietrich (1933), were collected by the German Tendaguru Expedition (1909-1912) at Tendaguru site IX, about 1.4 km northeast of Tendaguru Hill (Janensch, 1914). They were embedded in a medium- to coarse-grained sandstone of Late Jurassic (Tithonian) age at the transition between the so-called *Trigonia smeei* Bed and the base of the Upper Saurian Bed. Most specimens are fragmented and the outer surface appears pitted due to intense weathering.

Recent sedimentological and palaeoecological analyses of the Tendaguru Beds (Aberhan et al., 2002) suggest that deposition of the *Trigonia smeei* Bed took place in lagoon-like, shallow marine environments above fair weather wave base and with evidence of

tides and storms. Sediments of the Upper Saurian Bed represent extended siliciclastic tidal flat environments including brackish coastal lakes and ponds. The Late Jurassic palaeoclimate of the Tendaguru area was subtropical to tropical, characterised by seasonal rainfall alternating with a pronounced dry season.

The analysed rostrum of *Belemnella (Pachybelemnella) sumensis* Jeletzky is from the boreal Upper Cretaceous (Lower Maastrichtian) White Chalk of the Stubbenkammer, isle of Rügen (Northeastern Germany). The sedimentary matrix is a weakly lithified coccolith limestone, representing fully marine, distal open shelf conditions well below storm wave base. The fossil material figured here is housed at the Museum für Naturkunde (MfN), Humboldt-Universität zu Berlin if not mentioned otherwise. As far as registration in the respective collection was finished at the time of writing, the catalogue numbers of the specimens will also be given.

Five pathological belemnite guards from the collection Keupp (PB), housed at the Institut of Geological Sciences, Freie Universität Berlin, Germany, were also investigated. PB246, PB248 and PB249 are *Gonioteuthis quadrata* (Blainville, 1827) guards from the Late Cretaceous (Upper Campanian, ca. 75 Myr) of the marl pit "Alemannia", Höver near Hannover, Germany. PB264 is a cast of a *Neoclavibelus subclavatus* (Voltz, 1830) rostrum from Late Toarcian (Upper Liassic, ca. 182 Myr) of Mistelgau near Bayreuth, Germany. Our study has been performed on the original sample which is with V. Kriegisch, Schonungen, Germany. PB251 is a *Hibolithes jaculoides* (Swinnerton, 1937) rostrum of the Lower Cretaceous (Late Hauterivian, ca. 118 Myr) from the coast of Helgoland Island, Germany.

Vertebrates

The first bone sample used for the current study is a periotic (whale earbone) originating from a partial skeleton of a kentriodontid dolphin (Cetacea: Odontoceti) belonging to the genus *Atocetus* (de Muizon, 1988) of the subfamily Pithanodelphininae Barnes, 1985. The fossil was discovered in a commercial gravel pit near Groß Pampau in Schleswig-Holstein, Northern Germany, and is stored since then in the Museum für Natur und Umwelt in Lübeck (MNU-071-18). The site is famous for several whale remains (e.g. Höpfner, 1991; Hampe, 1999). The horizon containing the whale fossils belonged to a dark mica clay ("Oberer Glimmerton" in regional stratigraphy, cf. Hinsch, 1990) that was deposited between 10.6 Ma and 11.8 Ma (Spiegler and Gürs, 1996) after *Bolboforma* biozones (about the middle/upper Miocene boundary) and is rich in organic matter, the sheet silicate muscovite and occasionally in pyrite, glauconite, and carbonate (Gripp, 1964).

Plants

For this study, two silicified fossils were chosen that exhibited some well-preserved ana-tomical details under the light microscope. They were collected by Wehrfeld in North Patagonia, Argentina, in 1937 and later donated to W. Gothan. The material comes from the "Classic" locality Cerro Cuadrado, where silicified conifer remains are preserved in a volcanic ash. The age of these fossils is considered to be mid- to late Jurassic (Calder, 1953; Menéndez, 1960). Cones in the same state of preservation have been described earlier (Spegazzini, 1924; Gothan, 1925; Darrow, 1936; Calder, 1953; Stockey, 1977, 1978), and a comprehensive monograph on Cerro Cuadrado conifer fossils is available (Dernbach et al., 1992).

The cones are completely silicified by alpha-quartz, as demonstrated by x-ray diffrac-tion (Stockey, 1975). This quartz, known as chalcedon, spots a wide variety of colours. In case of the conifer cones, abundantly interspersed hematite renders the fossils reddish brown. However, it seems that different seed tissues of these cones tend to show differ-ently coloured quartz (Darrow, 1936). Consequently, the parts of these cones can be easily distinguished by light microscope when cut.

Two fossils were used for this study. The first one is a silicified twig of about 9 cm length and approximately 1.3 cm diameter from an araucarian conifer and appears poorly preserved, perhaps due to longer periods of exposure to water erosion shortly after death. The piece is broken off at the base and at the top. The *Brachyphyllum*-type foliage is dense and seems to be helically arranged. The leaves show rhomboidal leaf cushions and acute apices. In most cases, only the leaf base is preserved, and no obvious wood or leaf-structures could be found under the light microscope.

The specimen MB.Pb. 2006/33-36, a cone of a conifer of uncertain affinities, *Para-raucaria patagonica* (Wieland, 1935), is approximately 3.3 cm in length and 1.5 cm in maximal diameter and exhibits an excellent threedimensional preservation of a typical cone morphology.

Further fossil samples

A broad range of other fossil taxa was also tested for MR applicability but since their morphological description is not in the focus of this thesis, MR data will only be shown for a small – but taxonomically broad – selection. These samples will just briefly be described along with the respective sample image.

4.3.2. MR parameters

The MRI experiments were performed on a Bruker Avance NMR spectrometer (Bruker, Rheinstetten, Germany) operating at a ^{1}H resonance frequency of 400 MHz with standard Micro2.5 microimaging equipment and a maximum gradient strength of 0.4 T/m. Images were recorded using a standard 3D spin-echo imaging sequence, i.e. with an echo time $T_E = 1.3$ ms, repetition time $T_R = 1$ s, spectral width SW = 150 kHz if not mentioned otherwise (for details, see Ernst et al., 1997)). Each image consists of 128x128x256 pxl^3. With typical sample dimensions of the order 10x10x30 mm^3, this normally resulted in spatial resolutions around 100 μm. The total experimental time (T_{exp}) ranged between 18 and 93 hours per image, depending on each sample's signal strength. Details are given in the figure legends.

4.4. Results

4.4.1. *In saxo* MRM of fossil morphology

Belemnites

In cross-sectional MR images of the Tendaguru samples, concentric circles reflecting radially oscillating signal intensity can easily be identified – with higher signal intensity indicating a higher number of mobile ^{1}H nuclei, and lower signal indicating lower ^{1}H contents, lower mobility or a combination of both. As for the molecular affiliation of these nuclei, water trapped in nanopores or organic remains of the original material perhaps provide the simplest explanations. This is compatible with recently published findings (Florek et al., 2004), according to which organic and inorganic signals in electron microprobe measurements showed very similar oscillatory patterns, yet with opposite sign, along a radial line extending from the central channel. The signal oscillations correspond to growth rings reflecting a layered microstructure similar to the one described for nacre (Jackson et al., 1988; Feng et al., 1999, 2000), where inorganic layers (aragonite in molluscs, calcite in belemnites) basically alternate with organic layers, with each of both phases forming a continuum through small bridges (cf. Fig. 10ff in Jackson et al., 1988) but those can not be identified in the MR images.

In the longitudinal sections, the apical line or central channel is visible in its whole preserved length, from the apex till the alveolus at the distal tip of the phragmocone (which forms the border between the rostrum cavum and the rostrum solidum). Interestingly, the signal distribution observed in the three belemnite samples differs considerably – while the growth rings can easily be distinguished in the Tendaguru sample where the central channel shows a very low signal, the situation is opposite in the other two samples, though at a lower overall signal intensity. Gradient-echo sequences were also tested on some of the specimens but did not give images of comparable quality.

4.4.2. *In saxo* **MRM of fossil pathology**

All five belemnite guards described in this section exhibit anomalous growth patterns, the beginning of which – as well as their presumptive endogenous or exogenous origins – are not observable from outside, since subsequent calcitic lamellae cover the original disruption and obstruct the cause for its existence. In each case, the MR imaging series allowed to extract a plausible hypothesis about the respective pathogenesis and of growth anomalies developing in relation to that. The following pathological morphologies have been recognised and their causality interpreted:
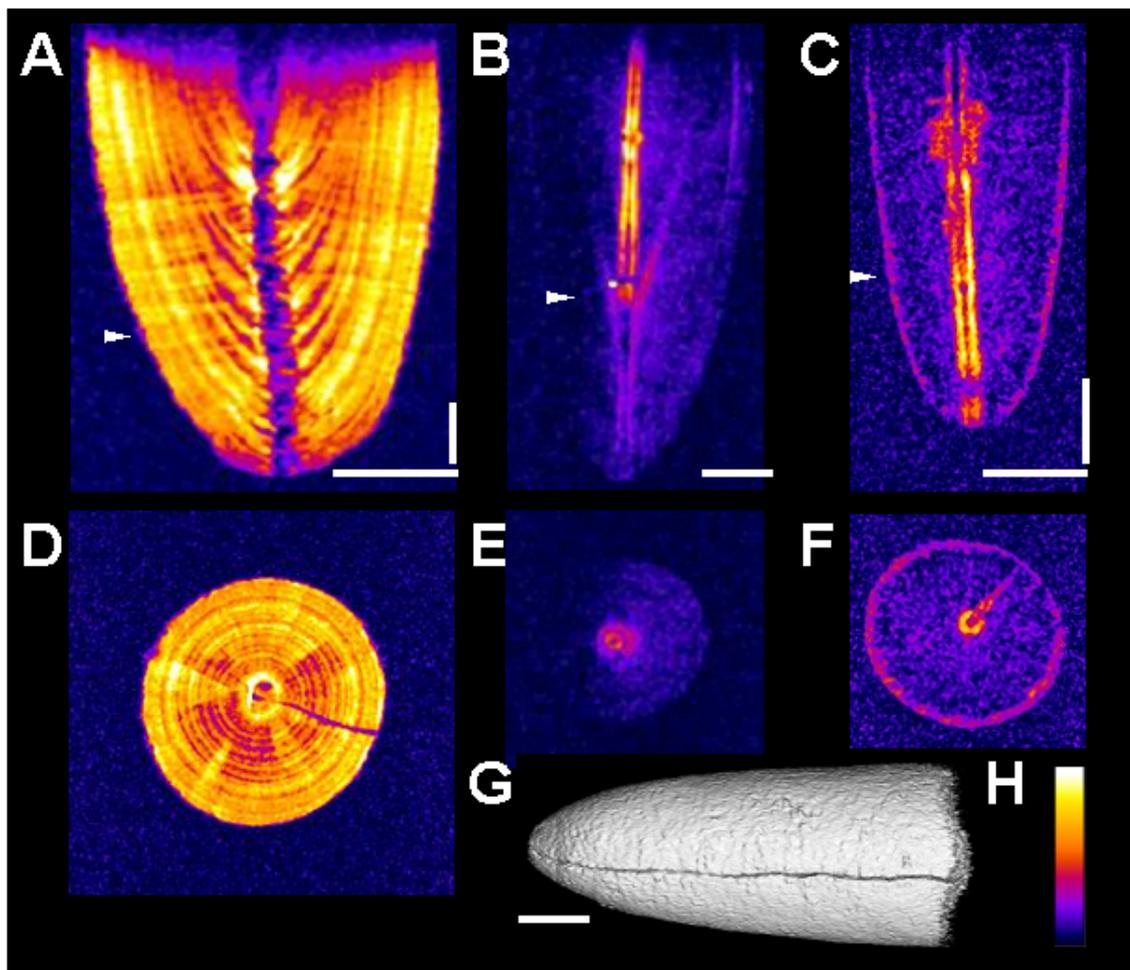

Figure 4.2.: Three-dimensional MR image slices of three belemnite guards of different origin. (A) Longitudinal section of a *Belemnopsis sp.* (MB.C.3701.3) from Tendaguru, site IX. FOV: $15\times15\times30$ mm^3, MTX: $(256 \text{ pxl})^3$, T_R: 784 ms, NA: 8, T_{exp}: 113 h. Arrow head indicates position of the slice depicted in (D). The corresponding slice series (in steps of 117 μm) with this orientation is given in Movie 4.2 Ⓜ. Scale bars throughout this chapter are isotropic 5 mm or otherwise 5 mm in the indicated directions. (B) *Belemnopsis* sp. of uncertain affinity. Arrow head indicates slice position for (E). FOV: $18\times18\times36$ mm^3, MTX: $128\times128\times256$ pxl^3, T_R: 800 ms, NA: 2, T_{exp}: 14 h. (C) *Belemnella occidentalis*, from Rügen. Arrow head indicates slice position for (F). FOV: $12\times12\times30$ mm^3, MTX: $128\times128\times256$ pxl^3, T_R: 1000 ms, NA: 2, T_{exp}: 18 h. (D) Transverse section as indicated in (A). (E) Transverse section as indicated in (B). (F) Transverse section as indicated in (C). (G) 3D model of the Tendaguru specimen in (A), directly obtained from MRI data (scaled to isotropy). (H) Colour scale of MR signal intensity in arbitrary units (identical for all MR images in Chapters 4 and 5 if not mentioned otherwise).

Sublethal injury with fracture of the rostrum (Cat. No. PB246)

The complete, 33 mm long and up to 9 mm broad guard of *Gonioteuthis quadrata* shows a zigzag-like deformation (Fig. 4.3A). The MR image (Fig. 4.3B) revealed multiple internal fractures of the juvenile guard (Ø 5.1 mm in maximum) distally of the intact alveole. It seems plausible that, following a probably sublethal bite of an unknown predator, the second fragment has ventrally been dislocated almost perpendicularly to the two neighbouring fragments, while the small final fragment of the distal tip of the rostrum shows only a tiny kink. A presumed fourth fracture cutting the small fragment near the distal tip produced no dislocation. The fractures healed after the dislocated fragments were fixed by the surrounding soft body which mainly consisted of muscles and tendons (Abel, 1916), and was then consecutively covered with several calcareous layers.

The interim surface of the guard's fragments at the time of the traumatic attack is marked by sharp lines of high signal intensity, interpreted as to represent a temporary interruption of the mineralisation which might have triggered a higher incorporation of organic material. During regeneration, the secretion of new calcareous layers was partly asymmetrical. Particularly inside the knee-like arrangement of the rostral fragments (i.e. dorsally), the thickness of single growth lines is enlarged, and accreted posttraumatic calcitic layers add up to 6.2 mm in thickness, whereas they are reduced on the convex part – only a 0.8 mm thick posttraumatic calcitic coating was added at the ventral part of the knee. A very similar anomalous guard of *Hibolithes subfusiformis* was reported earlier to have recovered from a double-fracture by forming such a double-kinked rostrum (cf. pl. 10, Fig. 17 in Duval-Jouve, 1841).
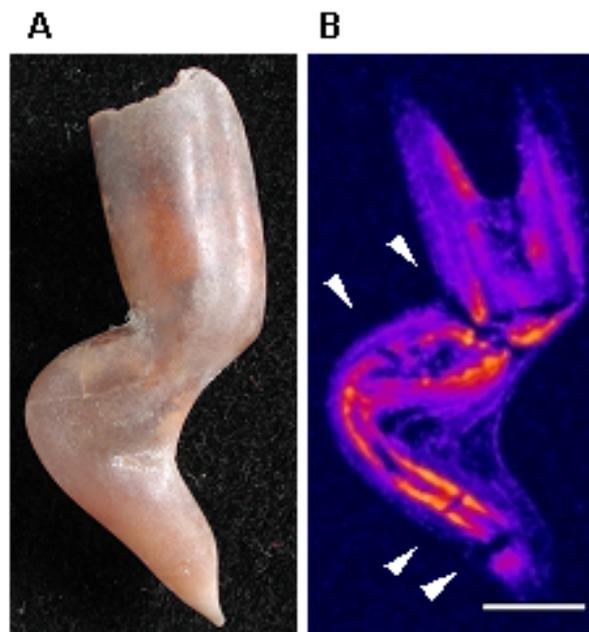
Figure 4.3.: Sublethal injury with fracture of the rostrum. *Gonioteuthis quadrata* (Blainville, 1827) guard with a zigzag-like deformation. (A): lateral view (photomicrograph). (B): median MR section. Arrow heads indicate fractures. The corresponding slice series (in steps of 125 μm) with this orientation is given in Movie 4.3 Ⓜ. Acquisition parameters: FOV: $15 \times 15 \times 32$ mm^3, MTX: $128 \times 128 \times 256$ pxl^3, NA: 2, T_{exp}: 18 h.

Sublethal injury which only affected the muscle mantle around the guard (Cat. No. PB248)

Two anomalous rostra of *Gonioteuthis quadrata* exhibit an apparent doubling of their pointed apexes. The 60 mm long and up to 9 mm wide guard PB248 developed, along the final 25 mm of the main guard, a second rostral element laterally, beginning with a bubble-like bulge of 9 mm length (Fig. 4.4A). The phenomenon corresponds with an apparent bifurcation of the rostrum in which the two branches – that originally developed separately and ran parallel to each other – have in fact been connected in a later phase by common growth layers.

The MR image (Fig. 4.4B–E) suggests that the surface of the juvenile guard inside (Ø 7.6 mm) was probably undamaged at the beginning of the anomaly. The irregular growth pattern from which the bulge arose through subsequent thickening by new calcite layers can be interpreted as a disturbance of the calcite secreting mantle, most probably initiated by a traumatic event. The muscular mantle had in part torn off, thereby isolating a small piece of it. Similar to the formation of a free pearl in mussels where an isolated fragment of the secreting epithelium provides the basis for the construction of the pearl sac (Götting, 1974; Keupp, 1987), this small piece was then the starting point for a second mantle fold during regeneration of the mantle tissue in which an additional rostrum could evolve.
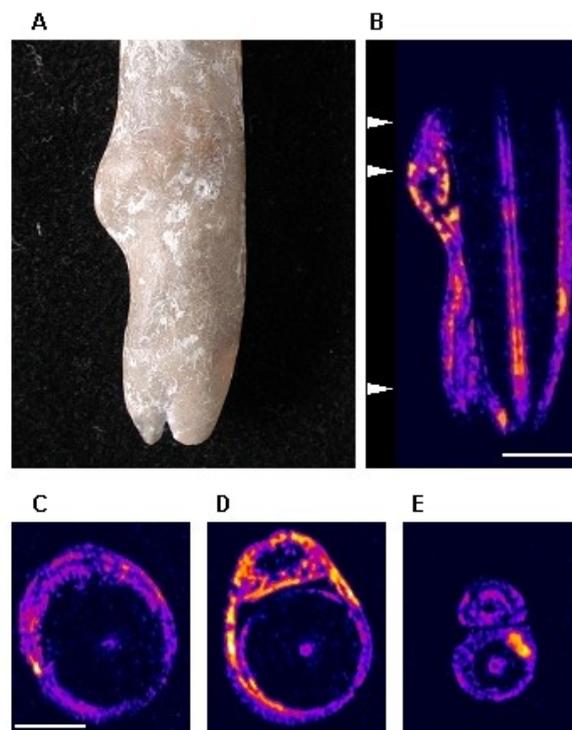
Figure 4.4.: Sublethal injury of the muscle mantle. *Gonioteuthis quadrata* (Blainville, 1827) guard with a twin apex. (A): lateral view (photomicrograph). (B): longitudinal MR section. Arrow heads indicate positions of the slices depicted in (C)–(E). (C): transverse MR section through the beginning of the anomaly exhibiting the preceding injury of the interimistic guard's surface. (D): transverse MR section through the initial bulg. (E): transverse MR section through the double rostrum at the posterior part. Acquisition parameters: FOV: $10 \times 12 \times 28$ mm^3, MTX: $128 \times 128 \times 256$ pxl^3, NA: 4, T$_{exp}$: 36 h.

The moment of the traumatic event is marked by a sharp growth line inside the entire guard, documenting again the phase of regeneration in which the mineralisation process was temporarily interrupted and a distinct layer probably rich in organic matter inserted. Similar anomalous rostra with proliferate growth phenomena by formation of separated mineralisation centres have been described of a Jurassic *Hibolithes*, while guards with two or multiple tips have repeatedly been reported (Keupp, 2002, and references therein).

Apical collar as a result of inflammation (Cat. No. PB249)

Another phenomenon frequently observed in Late Cretaceous belemnite guards of different taxa but not yet described is the development of a small collar-like rim in dorsal position above the rostral tip. The 75 mm long and up to 11 mm broad guard PB249 appears to have a double tip, owing to the close position of the anomalous dorsal collar to the normal tip of the rostrum (Fig. 4.5A). Yet it differs significantly from the real double tips described above. The MR image (Figs. 4.5B and 4.5C) reveals that the growth of the anomalous collar starts at the former surface of the guard with no visible damage and continues into a small hollow tunnel with an apical opening. The small tunnel resembles drainage channels for organic fluids of inflammatory portions of tissue. Therefore, this characteristic anomaly of belemnite guards is presumed to have been initiated by a local infection or other inflammatory disturbances of the muscular mantle, perhaps also by settlement of a tiny parasite (see below).
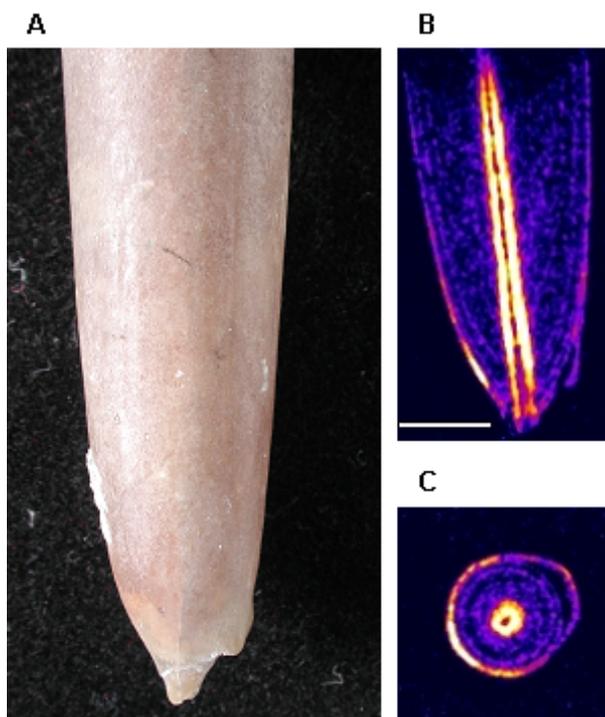

Figure 4.5.: Apical collar. *Gonioteuthis quadrata* (Blainville, 1827) guard with a collar-like dorsal anomaly. (A): lateral view (photomicrograph). (B): median MR section. (C): transverse MR section through the anomalous dorsal lip. FOV: $12 \times 12 \times 28$ mm^3, MTX: $128 \times 128 \times 256$ pxl^3, T$_R$: 852 ms, NA: 12, T$_{exp}$: 93 h.

Disturbance of the guard secreting mantle by presumed parasitism (Cat. No. PB264)

Bubble-like protuberances of guards as depicted in Figs. 4.6 and 4.7 were very probably initiated by implantation of parasites. The 32 mm long rostrum of *Neoclavibelus subclavatus* exhibits a drop-sized bubble elevated up to 5 mm above the guard's normal surface and shows a growth direction towards the anterior part of the animal (Fig. 4.6A). The vertical and horizontal MR image sequences (Figs. 4.6B–D) show a prominent growth line surrounding the juvenile guard at about 2.9 mm diameter.

During subsequent thickening of the guard, the successive formation of an irregularly bordered cavity can be observed immediately above the tip of the interimistic surface of the guard. At the beginning and end of the increasing bubble-like anomaly, no signs of a preceding damage of the rostrum are recognisable (cf. Fig. 4.6D). The sharp concentric growth line drawing the undisturbed juvenile guard is therefore presumed to mark the temporary interruption of an otherwise rather continuous secreting activity of the muscular mantle in response to the infection by an unknown parasite. The protuberance of the guard probably results from the successively increasing proliferation of the endoparasite. A 3D model of the guard, as obtained from the MR images, is depicted in Fig. 4.6E.
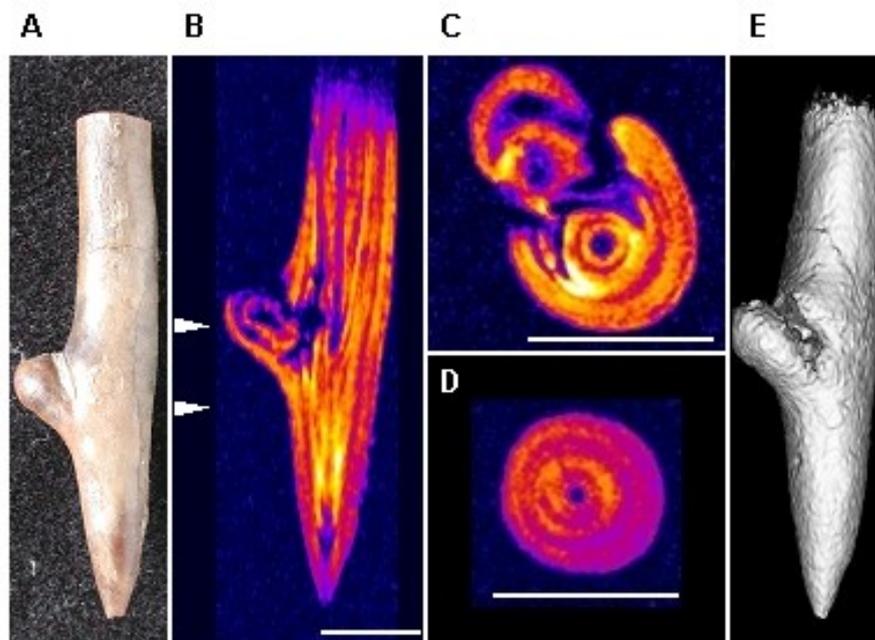
Figure 4.6.: Disturbance of the guard secreting mantle. *Neoclavibelus subclavatus* (Voltz, 1830) guard (collection of V. Kriegisch) with an anomalous protuberance, presumably caused by parasitism. (A): lateral view (photomicrograph). (B): median longitudinal MR section. Arrow heads indicate positions of the slices depicted in (C) and (D). (C): transverse MR section through the bubble-like anomaly. (D): more distal transverse MR section through normal tissue. The radial lines are indicative of the direction of calcite crystal growth. (E): 3D model of the guard, directly obtained from the MR images. FOV: $8{\times}8{\times}30$ mm^3, MTX: $128{\times}128{\times}256$ pxl^3, T_R: 952 ms, NA: 10, T_{exp}: 87 h.

Early disturbance of the guard secreting mantle by presumed parasitism (Cat. No. PB251)

A similar syndrome, probably also due to parasitism, is shown in Fig. 4.7. The surface of the 43 mm long and – outside the anomaly – 7 mm wide rostrum of *Hibolithes jaculoides* is slightly corroded. An ovoid bubble elevates about 6.5 mm above the normal surface near the proximal part of the guard (Fig. 4.7A). The MR images (Figs. 4.7B and C) suggest that the formation of the anomalous bubble began during an early ontogenetic stage and enabled the formation of an internal irregularly bordered cavity which enlarged the middle axis of the rostrum up to 7 mm. The anomaly starts close to the empty alveole from which only the distal part is preserved, probably situated immediately after the (invisible) primordial rostrum. The internal cavernous structure seems to be divided into a proximal ovoid chamber of ca. 2 mm by 5 mm, potentially reflecting the original size of the encysted parasite itself, and a larger distal portion characterised by proliferous growth of irregular tissue without or with only slight calcitic mineralisation.

Whale inner ear bones

The anatomy of the cetacean organ of hearing is well documented (Pilleri et al., 1987, see also Fig. 4.8) but was usually studied by producing serial sections by grinding the petrosals (e.g. Luo and Eastman, 1995; Luo and Marsh, 1996), resulting in the loss of the unique fossil specimens. The MR images, as with the belemnite samples discussed above, provide such morphological information non-invasively: Fig. 4.8D-E reveals a strong signal in the posterior cochlear part and the posterior process of the bone, as shown in light colours.

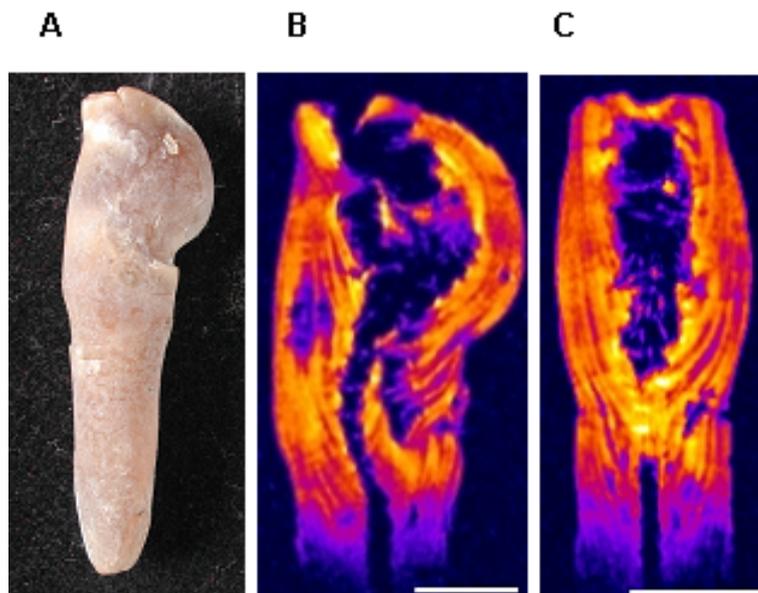**Figure 4.7.:** Early disturbance of the guard secreting mantle. Anomalous rostrum of *Hibolithes jaculoides* (Swinnerton, 1937). (A): lateral view (photomicrograph). (B): median longitudinalMR section. (C): dorsal longitudinal MR section. The corresponding slice series (proximal to distal in steps of 113 μm) with transverse orientation is given in Movie 4.7 Ⓜ. FOV: 13×11×29 mm^3, MTX: 128×128×256 pxl^3, NA: 4, T$_{exp}$: 36 h.

At the site of Groß Pampau the fossil bones are associated with diagenetically produced minerals like glauconite and pyrite. The latter is a product of a reaction between iron (Fe released by haemoglobin degradation) and sulphur (H_2S released by protein degradation Pfretzschner, 2000). FeS_2 (pyrite) develops under alkaline conditions, e.g. in the presence of water-dissolved NH_3 produced during collagen decay. It is less clear, however, what the destiny was of the hydrogen and carbon of the decomposed protein. Conversion to kerogen would be one explanation (Albrecht and Ourisson, 1971) but it could equally well be that they in part still reside in the bone and contribute to the high signal intensity.

MR images of further fossils and other dehydrated specimens

Fig. 4.9 shows a selection of other fossils and dehydrated samples relevant to fossil MRI: Fig. 4.9A depicts a columnal (stem element) of the crinoid species *Isselicrinus buchii* Roemer (1840) from the same white chalk sediment of the isle of Rügen as the belemnite shown in Fig. 4.2C. The spatial resolution achieved with this sample was 108 μm in the image plane depicted here (which was artificially increased by a factor of two via zero-filling of the data set before Fourier transformation) and 50 μm perpendicular to it – the highest resolution achieved in the fossils described in this thesis (see also Movie 4.9).

Next to it (Fig. 4.9B) is a 3D model of the brachiopod *Dictyothytis kurri* from the collection of Helmut Keupp at Freie Universität Berlin. It has to be noted that the two valves of the fossil were kept as they were – i.e. completely closed and inseparable – such that the internal brachial architecture important for taxonomy was not accessible to optical techniques. Virtual reconstruction on the basis of the MRI data, however, allows the partial visualisation of this architecture (cf. arrow). Fig. 4.9C shows the conifer cone of *Pararaucaria patagonica* from Cerro Cuadrado, highlighting the cone axis in the centre, surrounded by scales. The embedded seeds on each ovuliferous scale are clearly observable (high signal), and even the embryos inside the seeds can be discerned. The second plant sample, the badly preserved *Araucaria* twig, was also tested but did not give a signal sufficient for microscopic images.

In addition to the *Atocetus* specimen, a larger mammal's long bone fragment was subjected to MRI (cf. Fig. 4.9D). It had been unearthed from unit II/III of the palaeolithic site of Azokh Cave (Fernández-Jalvo et al., 2004) in Nagorno-Karabagh (Lesser Caucasus), accompanied by Mousterian stone tools. [14]C dating provided an age beyond the limit of the method (i.e. 60 ka or older). The layer is rich in bones of the fossil bear *Ursus spelaeus* but since the piece was foreseen for DNA analysis, no detailed taxonomic analysis was performed. Human remains have not yet been discovered in units II/III, although the oldest unit V had yielded a mandible of *Homo heidelbergensis* (Kasimova, 2001).
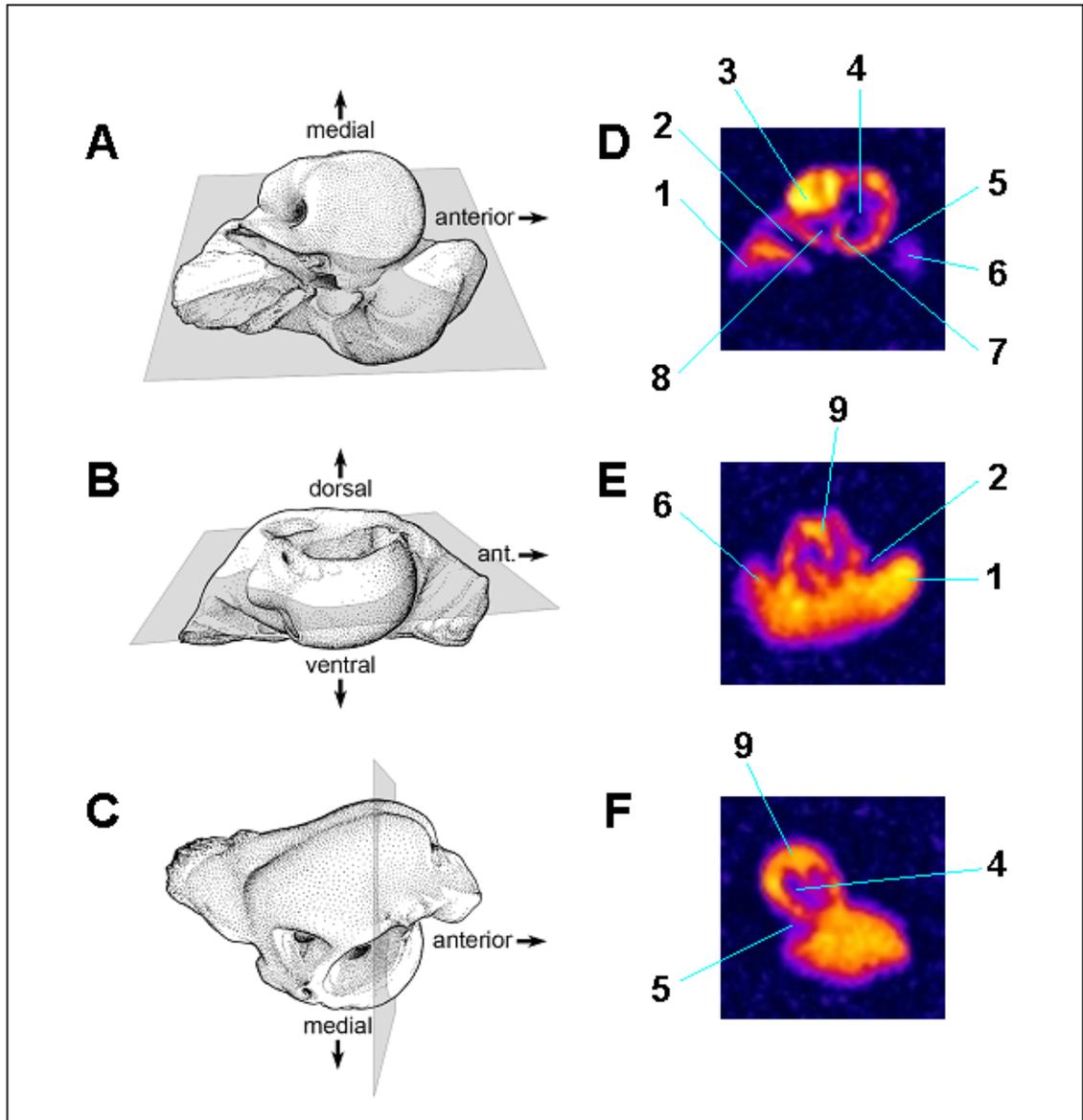
Figure 4.8.: Whale inner ear anatomy: Left periotic of *Atocetus sp.*, MNU 071-18. (A)–(C) Three-dimensional representation of the surfaces of the fossil, with the orientation of the corresponding MR slices indicated. (A) ventral/tympanal view. (B) medial view. (C) dorsal/cerebral view. (A)–(C) courtesy of Oliver Hampe. (D)–(E) Three-dimensional representation of internal morphology. *Atocetus sp.*, MNU 071-18, left periotic. (D) MR diagonal section. FOV: $20\times20\times40$ mm^3, MTX: $64\times64\times128$ pxl^3, T_R: 900 ms, T_E: 0.6 ms, NA: 16, T_{exp}: 32 h. (E) MR horizontal section. (F) MR vertical section. The numbers indicate the following anatomical structures: 1, posterior process; 2, canal for facial nerve; 3, organic matter; 4, inner auditory passage; 5, groove for tensor tympani; 6, anterior process; 7, transversal septum; 8, fenestra rotunda; 9, cochlea.

A further anthropological sample was an arrow head made of flint stone, found at the neolithic site of Ba'ja, Jordan. Its 3D image did not give very good contrast but the 2D projection of all its 128 3D slices nonetheless clearly reflects the shape of the arrow-head (Fig. 4.9E).

Finally, a slice of a 3D image of a brachiopod is shown in (Fig. 4.9F). However, the important point here is not the fossil (which appears white in this recontrasted image) but the round sample holder with one central and four peripheral holes. It is made of polymeric tetrafluormethan which is often used as a sample holder for MR experiments, as it gives a vanishing signal (Bloembergen et al., 1948). Approaching the limits of MR applicability to dehydrated samples thus also means that residual protons due to organic solvents remaining from the production process or due to impurities can be detected in MR image data.
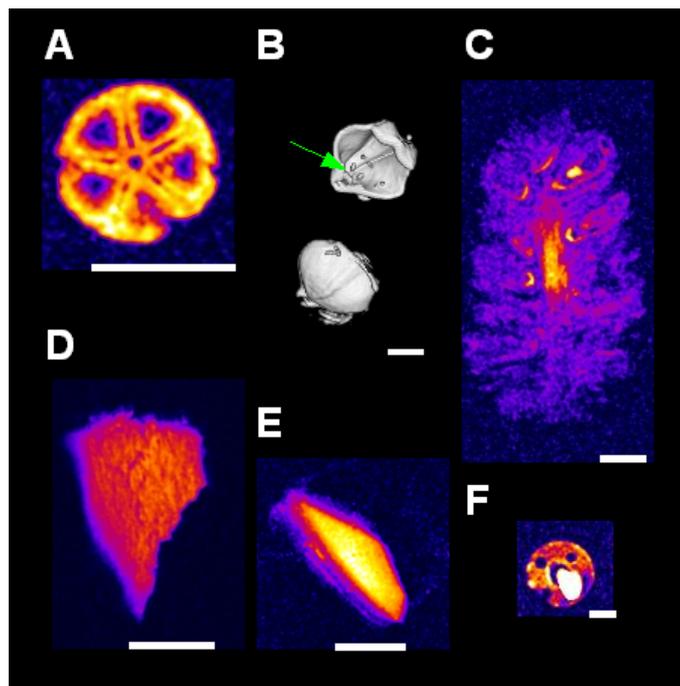

Figure 4.9.: Further sample MR images of dehydrated specimens. (A) Fossil crinoid (*Isselicrinus buchii*) from Rügen, Germany. FOV: $6.9\times6.9\times3.2$ mm^3, MTX: $(64$ pxl$)^3$ (here zero-filled to an isotropic matrix of 128 pxl), T_R: 2.9 s, NA: 32, T_{exp}: 106 h. The corresponding original image slice series (with steps of 50 μm) is supplied as Movie 4.9 Ⓜ. (B) 3D model directly obtained from 3D MRI data of a fossil brachiopod (*Dictyothytis kurri*). The two shells were artificially separated in the image in order to reveal the brachia (arrow). FOV: $15\times15\times15$ mm^3, MTX: $64\times64\times64$ pxl^3, T_R: 500 ms, NA: 32, T_{exp}: 18 h. (C) Fossil cone of the conifer *Pararaucaria patagonica*. FOV: $17\times17\times34$ mm^3, MTX: $128\times128\times256$ pxl^3, T_R: 1000 ms, NA: 12, T_{exp}: 109 h. (D) Fossil human bone fragment from the palaeolithic Azokh cave (Nagorny Karabakh, Caucasus). Unidentified fragment of a long bone of a larger mammal from (Unit II/III) of the palaeolithic site Azokh Cave (Nagorno-Karabagh, Caucasus). FOV: $9\times9\times22$ mm^3, MTX: $128\times128\times256$ pxl^3, T_R: 450 ms, NA: 12, T_{exp}: 49 h. (E) 2D projection (sum) of 3D image slices of a flint stone arrow head from the neolithic site of Ba'ja, Jordan. FOV: $15\times15\times$ mm^3, MTX: $128\times128\times128$ pxl^3, T_R: 1000 ms, NA: 4, T_{exp}: 18 h. (F) Tetrafluormethan sample holder. The white area is part of a brachiopod fossil which gave a higher signal. FOV: $(19$ mm$)^3$, MTX: $(64$ pxl$)^3$, T_R: 450 ms, NA: 8, T_{exp}: 4 h.

4.5. Discussion

This study has shown that Magnetic Resonance techniques allow to non-invasively visualise structural details in fossils with diverse taxonomic backgrounds and from different sites but it is not clear where the signal comes from. Fortunately, the anomalous samples already give some hints:

- First, signal intensity in the pathological regions is usually higher (cfs. Figs. 4.4B and 4.4D) and rarely lower (cracks in Fig. 4.3B) than in the normal ones, thereby indicating that the syn vivo processes laying the ground for the uneven signal distribution were activated rather than inactivated by the pathological incident. This corresponds well with previous reports of higher organic contents in pathologically affected areas (Sælen, 1989).

- Second, the frequent observations of a hollow (as in PB264 and PB251) rostrum cavum have led to the suggestion that its primary content might have been organic (Bandel and Spaeth, 1988).

- Third, in cases where the innermost layer of the rostrum is not hollow, it gives a higher signal than its immediate surrounding (as in Figs. 4.3 and 4.4). While this might equally point at taxonomic differences, it is well compatible with the assumption that the image contrast in the belemnite MRI data basically stems from differences in primary content in organic matter which was, perhaps, later partly replaced by diagenetic calcite.

- Fourth, the compact concentric layering of separate organic and anorganic layers in belemnites could provide an explanation for good conservation of organic matter within these structures.

However, the spin-echo sequences without selective excitation used for these experiments can not distinguish between signal contributions from ^{1}H nuclei in organic or inorganic groups, nor could gradient-echo sequences whose signal intensity did not reach that of the spin-echo images, probably due to susceptibility gradients within the samples. Furthermore, organic contibutions to the MR signal could possibly be justified even in the flint stone sample (cf. Fig. 4.9E), as flint has repeatedly been found to contain fossils and their organic remains (e.g. Ehrenberg, 1854; Deflandre, 1934).

Therefore, ^{1}H and ^{13}C MAS spectra were acquired from a powdered piece of a non-pathological belemnite from Tendaguru. The ^{13}C spectrum (Fig. 4.10) shows a peak (at about 180 ppm) reflecting C=0 or C=S double bonds, while no other signal can be clearly identified, and namely no CH_x groups which would hint at organic material. The ^{1}H spectrum, on the other hand, is dominated by the water peak at 4.8 ppm but also shows a small peak between 0 and 1 ppm, which indicates cyclopropyl or metal-bound methyl groups.
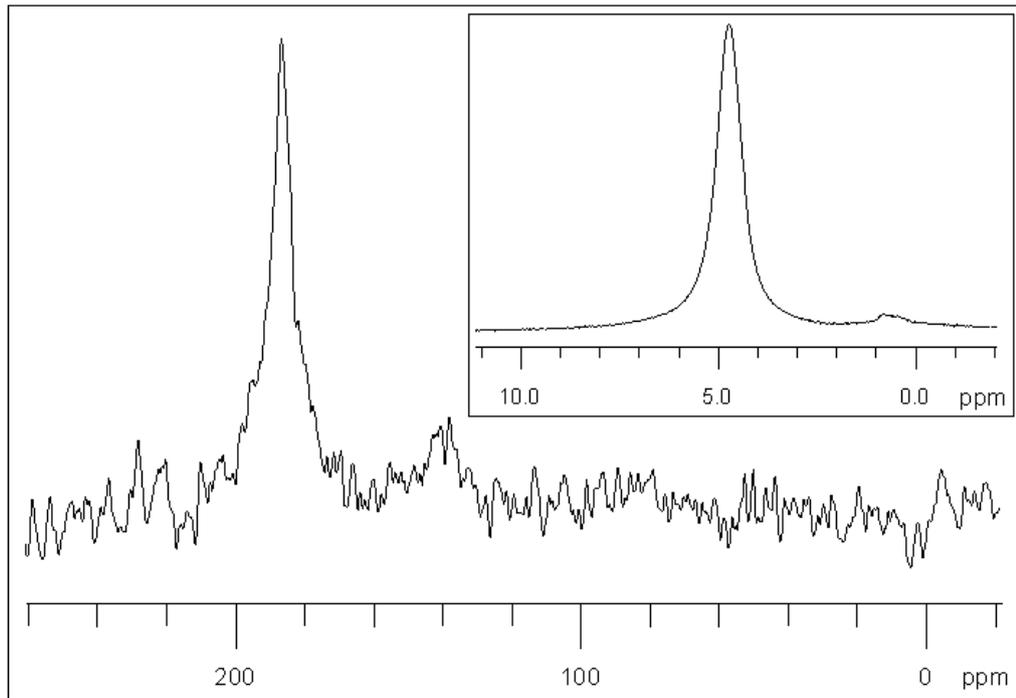
Figure 4.10.: [13]C MAS spectrum of a powder sample obtained from the rostrum of the Tendaguru belemnite (*Belemnopsis* sp.) with the project-internal number 9. Inset: Corresponding ^{1}H MAS spectrum. Both spectra were obtained at a spinning frequency of 10 kHz and calibrated against TMS in a separate experiment under otherwise identical conditions.

Part of the material used for the MAS experiment was then subjected to organochemical analysis by successive extractions with dichlormethyl/methanol, dichlormethyl/ethanol and ultrasonication, which did not reveal any traces of lipids, though it does not allow definitive statements about the contens in other organic constituents or water (Pierre Albrecht and Armelle Charrié, personal communication). Consequently, at least in this Tendaguru belemnite, the signal is not of an organic origin but mainly due to water. Whether this assumption also holds for the pathological belemnites and the other samples remains to be determined. In light of the palaeopathological investigations, however, it seems possible that the higher signal intensity observed in pathologically altered regions of the belemnites is not directly due to an originally elevated level of organic compounds but instead indirectly linked to it – larger amounts of organic matter might have resulted, upon degradation, in larger pores in the mineral matrix that were later filled by water.

4.6. Outlook

The MR image data obtained from belemnite guards allowed to observe their small-scale three-dimensional growth lamellae and to consistently interpret origins and developments of internal structures in rostra experiencing ontogenetic or anomalous anatomical and physiological alterations. Furthermore, the notion that the apical collar (cf. Fig. 4.5) might be indicative of an inflammatory disease illustrates that MRI can contribute to the generation or validation of hypotheses on belemnite pathologies.

Figure 4.11.: CT scans of pathological belemnites, as acquired with the multislice CT scanner (General Electric) jointly operated by the Leibniz-Institut für Zoo- und Wildtierforschung in Berlin and the Department of Veterinary Medicine at the Free University of Berlin (courtesy of Guido Fritsch and Helmut Keupp). Left: The same specimens as in Fig. 4.4. Right: The same specimens as in Fig. 4.7.

It was noticed earlier that the resolution of about 100 μm that was routinely achieved in this study "would be satisfactory ... for a majority of researchers and for most applications" (Lyons et al., 2002), at least after the Cambrian explosion. With this in mind, the MR image data obtained from fossils as diverse as crinoids, conifers and whales (cf. Fig. 4.9) demonstrate the wide taxonomic applicability of the method and suggest that MRI attempts to, say, visualise vasculature in permineralised plants, harbour considerable promise. It can even be expected that current or future MR imaging techniques will yield new insights into other heavily dehydrated specimens like mummies which had been unsuccessfully tested two decades ago (Notman et al., 1986).

Moreover, all other palaeontological investigations still remain possible after MRI scanning, which is not necessarily true in the opposite case. MR spectroscopy is one of these complementary techniques, and it can reveal insights into the molecular composition of the sample, e.g. that the belemnite analysed in Fig. 4.10 contained more mobile ^{1}H in water than in organic groups which are, nonetheless, present. On the basis of such MR spectroscopic data, a better planning of invasive investigations would be possible, thereby probably reducing the amount of specimen material that has to be consumed for individual non-MR investigations.

CT is another such complementary technique. It has already found wide application in fossil bones (e.g. Zollikofer and Ponce de Léon, 2005) and successfully been used for morphological studies of other types of fossils (e.g. ammonites, Keupp and Mita, 2004). CT was also tested with some of the pathological specimens presented above (cf. Fig. 4.11) but the image quality was much lower than in the corresponding MR scans. However, this can not be taken as a rule, and comparative analyses using both methods will surely find applications in the future.

It should be noted that the digital availability of MRI and CT data renders it ideal for applications like rapid prototyping (Zollikofer and Ponce de Léon, 1995) which can turn such large 3D data files into more human-accessible forms that have a high potential not only in biomedicine but also in science education at school or in museums (see also Zollikofer and Ponce de Léon, 2005).

Taken together, the microscopic resolution currently achieved with Magnetic Resonance techniques, their non-invasiveness, the possibility to obtain 3D spatial as well as chemical information, their potentially broad applicability and the multitude of ongoing efforts to further improve them (Glover and Mansfield, 2002) all suggest they could provide helpful insights into a wide range of palaeobiological issues, with the precious samples remaining intact.

Chapter 5. Magnetic Resonance Microscopy of frozen biological samples

5.1. Summary

Objectives Having shown in the previous chapters that MRI and water-suppressed localised MRS have the potential to become a tool in cell biology and that MRI can characterise the internal morphology of systems as dehydrated as fossils, the task for this chapter is to explore to what extent details of biological structures can be visualised by MRI under cryobiological conditions.

Methods Microscopic MR image series were acquired from a variety of aqueous solutions frozen in different containers, from tissue cultures and from cold-hardy insects – the gall moth *Epiblema scudderiana* and the gall fly *Eurosta solidaginis* whose larvae both overwinter in the goldenrod *Solidago* sp. and who serve as model organisms in the study of freeze avoidance and freeze tolerance, respectively.

Results Freezing in miniaturised cryocontainers is more homogeneous than in standard reaction tubes. MR image series of frozen cryobiological samples allowed to characterise media and particle suspensions for their cryoprotective potential. Large cells as well as large agglomerations of normal-sized cells can effectively be MR imaged at temperatures down to about -80°C, provided that sufficient amounts of cryoprotectants are present in the sample, so as to keep a MR-visible fraction of the water in a liquid state.

Conclusions ^{1}H MR imaging provides rich information about the distribution of water, ice and cryoprotectants within cryobiological samples, which opens up the possibility of using the method to study cryoprotection or freeze damage *in vivo* and to optimise cryobiological protocols.

5.2. Review of previous studies

From the perspective of a cell, the conversion from liquid to solid water is in many aspects similar to other forms of water loss or cell stress in the broader sense (Storey and Storey, 2004b). In terms of MR, the longitudinal relaxation time T_1 of water ice is similar to the T_1 of liquid water but the transverse relaxation time T_2 is about five to six orders of magnitude lower than in liquid water of the same composition. With the exponential relationship between the MR signal and T_2, this translates into an enormous signal decay upon freezing and a corresponding signal increase upon thawing, which provide a good basis for the experimental observation of these processes.

While theoretical and experimental determinations of the relaxation constants T_1 and T_2 of water, ice and steam was already included in one of the earliest descriptions of the Magnetic Resonance principle (Bloembergen et al., 1948), the first application of MR techniques to frozen samples of biological relevance was the determination of brine content in sea ice by comparing the integral MR signal intensity within a sea ice sample and a solution of known composition that was obtained by melting sea ice (Richardson and Keller, 1966). Later on, the temperature dependence of the brine content was determined and found to exhibit a hysteresis reflecting freezing parameters (Melnichenko et al., 1979).

Brine content was also the dominating feature in the first ^{1}H MR images of salt-water ice mimicking the mineral composition of sea water (Edelstein and Schulson, 1991), and of sea ice cores (Callaghan and Eccles, 1996, acquired at geomagnetic field strength in Antarctica). Furthermore, the diffusivity of the brine phase in intact sea ice cores could be measured by a pulsed field gradient MR technique (Callaghan et al., 1997), the previously reported temperature dependence of brine content (Melnichenko et al., 1979) could be correlated with changes in brine pocket size by MR imaging of sea ice (Eicken et al., 2000), and the freezing process was followed in a sea ice model system (Menzel et al., 2000). In the latter study, the ^{1}H MRI experiments were complemented by [23]Na MR techniques to monitor, e.g., the spatial distribution and diffusivity of the Sodium contained in the sample.

Apart from sea ice and related model systems, MRS has found multiple applications related to cryobiology, ranging from ^{31}P observation of phosphate metabolism (Storey et al., 1984) to ^{1}H studies of glucose metabolism and transamination after thawing (Dabos et al., 2002) and of water content in frozen biocatalytic systems (Volke et al., 1996) or frozen food (Mariette and Lucas, 2005). [1]H MRI, in turn, was used for temperature monitoring and damage assessment during cryosurgery (Daniel et al., 1999) as well as for the monitoring of freezing and thawing in food (Kerr et al., 1998) and cold-hardy plants (Price et al., 1997) and animals (Rubinsky et al., 1994a,b).

Although MR images have been used to follow ice nucleation even in single drops of cryoprotective solutions (Hindmarsh et al., 2004), there seems to be no report so far describing cryobiological MRI of cellular structures but since MR images as well as water-suppressed MR spectra can be acquired from subcellular structures in large well-hydrated cells (cf. Chapter 2) and microscopic resolution is feasible in fossil specimens with very low water content (cf. Chapter 4), it appears plausible that brine water or ^{1}H-groups in cryoprotectants can generate a ^{1}H MR signal sufficient for microscopic images of large cells under freezing conditions.

Unfortunately, large cells such as the *Xenopus laevis* oocytes used in Chapters 2 and 3 defy cryopreservation with current protocols because the (molecularly) long time required to freeze large cells generally allows a significant portion of the non-frozen intracellular water to leave the cell, and this dehydration causing irreversible cell damage (Dumont et al., 2004).

An alternative cellular model system close in size to *Xenopus* oocytes and thus in reach of MR microimaging are three-dimensional cell cultures, namely tumor spheroids. Since cell growth under natural conditions is a three-dimensional process, such spheroids allow, at least in principle, a more realistic three-dimensional assessment of cell and tissue properties than classical two-dimensional cell cultures can provide (Keller et al., 2003; Nelson et al., 2005). From a biomedical perspective, human and rodent cell lines are perhaps the most important ones, and so the human cell line PC3 and the mouse cell line L929 have been chosen because they serve as popular models for prostate cancer (e.g. Sintich et al., 1999; Ornstein et al.) and fibrosarcoma (e.g. Ladner et al., 1988; Penafiel et al., 1997), respectively.

Another cryobiological model system are cold hardy species. From a methodological perspective, it is advantageous to test MRM in model systems that show different cold response but are otherwise comparable. In this respect, the two *Solidago* parasites *Eurosta solidaginis* and *Epiblema scudderiana* (cf. introduction) come in very handy.

Eurosta larvae prepare for diapause – the stage of developmental arrest – in autumn by synthesising large quantities of glycogen which is then partly converted to glycerol when temperatures fall below +15°C, and the remaining portion into sorbitol below +5°C. Though both substances essentially replace water, they take over separate functions: The hydroxy groups of the alcohol help in hydrating cellular molecules, its hydrophobic groups keep the remaining water molecules from forming nucleation clusters (cf. Fig. 5.1, and sorbitol helps to maintain the phospholipid structure of the cellular membranes. Prepared this way, the cytoplasm stays supercooled even when extracellular ice formation starts at about -8°C.
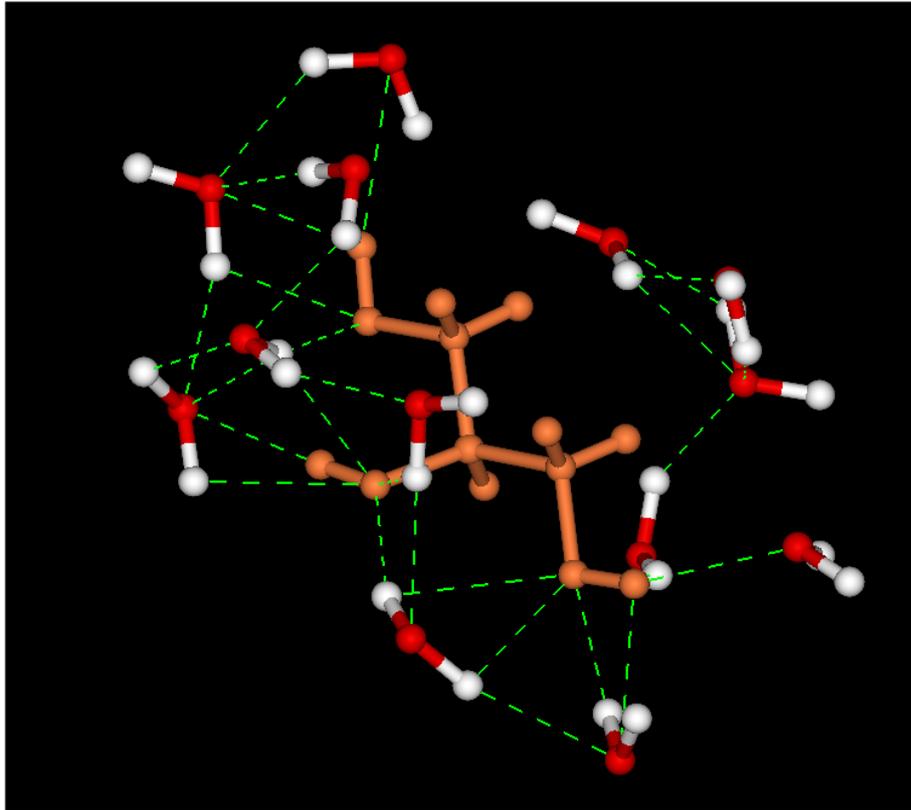
Figure 5.1.: Molecular modeling of the hydrogen bonding of glycerol surrounded by water molecules. Simulation performed with ViewerPro 5.0 (Accelrys Inc., www.accelrys.com).

Epiblema larvae use just the glycerol strategy of supercooling but they do so extensively, by accumulating glycerol up to 20% of their (wet!) body mass. This has the effect that the supercooling point of their cytoplasm and extracellular fluids is always about 15 K to 20 K below the mean daily temperature, thereby avoiding freezing and the associated cellular damage.

5.3. Experimental approach

5.3.1. Biological samples and solutions

Culture media

The following culture media were used in this study:

- Medium I was assayed in quantities of 1 l and composed of 90% Dulbecco/Vogt's Modified Eagle's Medium (DMEM; all chemicals in this Chapter were from PAN Biotech, Aidenbach, Germany, if not mentioned otherwise), 10% Foetal Bovine Serum (FBS or FCS), and 1 ml (50 mg/ml) gentamycin sulphate.

- Medium II was assayed in quantities of 1 l and composed of 285 mM trehalose, 5 mM histidine, and 5 mM KCl.

- Medium III was assayed in quantities of 1 l and composed of 90% RPMI (Roswell Park Memorial Instiue Medium, containing Ham's Nutrient Mixture F-12 with L-glutamine), 10% FCS, and 1 ml (50 mg/ml) gentamycin sulphate.

Tissue model preparation

- L929 spheroids were prepared by depositing 10 ml of a suspension of L929 cells ($2 \cdot 10^4$ cells/ml) in a Petri dish and subsequent cultivation at 37°C and 5% CO_2 for four days under daily optical control of the spheroid size.

- PC3 spheroids were prepared from a suspension of PC3 cells ($4 \cdot 10^7$ cells in 125 ml of Medium III) filled into a spinner flask that was then spun at 50 min^{-1}, 37°C and 5% CO_2 for two weeks under daily size control, with the medium being exchanged twice a week.

Cryo containers

Spheroids and solutions were frozen in 2×2 sections of a 6×5 HDPE microwell plate (Zimmermann et al., 2004, see also Fig. 5.5A).

5.3.2. Temperature control

For temperature control during the MR experiments, a dewar (Bruker, Rheinstetten, Germany) was mounted inside the probe and linked to a cryotank (Air Liquide, Neunkirchen, Germany) with liquid N_2 from which gaseous N_2 could be obtained by heating. Depending on the gas flow rate (determined by the heating rate in the tank), the 26 l in the tank usually lasted for about two days. Another heater was placed inside the dewar so as to heat the gas flowing to the sample, and both heaters were controlled by a PID (Proportional/Integral/Derivative) controller with the input from a thermoelement positioned 4 cm below the centre of the rf coil. Depending on the temperatures and on the gas flow rate, the temperature measured by the thermoelement was usually constant within ±0.2 K. Cooling and warming was performed at a rate of 1 K/min if not mentioned otherwise.

5.3.3. Infrared thermography

To monitor temperature changes occuring in the micro wells while the whole 6×5 micro well plate is subjected to external temperature profiles, an infrared thermography system has been set up at IBMT (Frank Ihmig, PhD Thesis in preparation). It uses a PYROVIEW 256 IR camera (DIAS GmbH, Dresden, Germany) and can deliver images with resolutions of up to 47 μm, 20 ms and 0.1 K in the spatial, temporal and thermal dimensions.

5.3.4. MR parameters

MR imaging and spectroscopy were performed as described in Chapter 4. Some other pulse sequences were also tested and will be mentioned in the figure legends, along with the detailed acquisition parameters. For the experiments with selective excitation of the water and fat resonances, a Bruker sinc3 soft pulse (cf. also Section 1.2) was applied as in the water and lipid suppression experiments in Chapter 2, but this time, the spoiling gradients were omitted in order to capture the signal of the respective water and lipid resonances.

5.4. Results

5.4.1. *In glacie* MRM of aqueous solutions

As previous studies had always employed multislice techniques, a first set of experiments was aimed at testing 3D image sequences on frozen samples. A slice from a 3D microscopic MR image of an aqueous solution at the onset of ice formation is given in Fig. 5.2A which depicts a cross-section through FCS-free Medium I with 10% DMSO at 273 K. At this temperature, the solution is still mainly in a liquid state but the image clearly reveals that ice crystal formation – probably initiated by heteronucleation – has already started. The arrangement of the crystals changed from a bundle-like structure at the edges to rather single units in the centre of the tube, while the ice surface that was in contact with air or the glass tube showed no signs of crystalisation but instead the highest signal intensity.
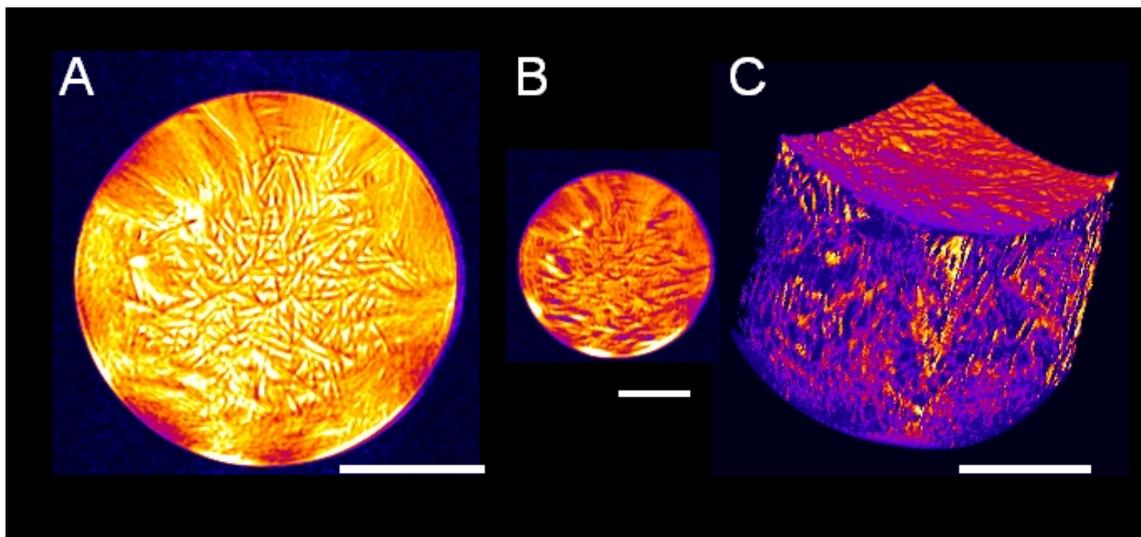
Figure 5.2.: 3D Brine patterns in FCS-free Medium I with 10% DMSO (A) Cross-sectional slice from a 3D image at 273 K. FOV: $15\times15\times20$ mm^3, MTX: $256\times256\times128$ pxl^3, T$_R$: 800 ms, NA: 2, T$_{exp}$: 14 h. As in Chapter 4, the scale bars in Chapter 5 are always 5 mm. The complete 3D image (in steps of 156μm) is provided as Movie 5.2 Ⓜ. (B) Cross-sectional slice from a 3D image at 253 K. MTX: $64\times64\times128$ pxl^3, T$_E$: 0.9 ms, T$_{exp}$: 4 h, otherwise identical conditions as in A. (C) 3D rendering of the image from which the slice depicted in A was taken.

This spatial pattern was stable in time and could also be observed at 253 K (cf. Fig. 5.2B), even though the signal intensity was then reduced by about one order of magnitude. 3D rendering allowed a three-dimensional visualisation of the distribution of the brine pockets under both conditions, and the result for 273 K is shown in Fig. 5.2C.

Pure water often freezes so quickly that crystal formation could not routinely be followed in time by MR imaging. However, occasional variations in the nucleation conditions could sometimes slow down this process sufficiently to allow for MR images to be recorded, as demonstrated by the image depicted in Fig. 5.3A-B which was recorded in a 2D slice-selective spin-echo experiment.
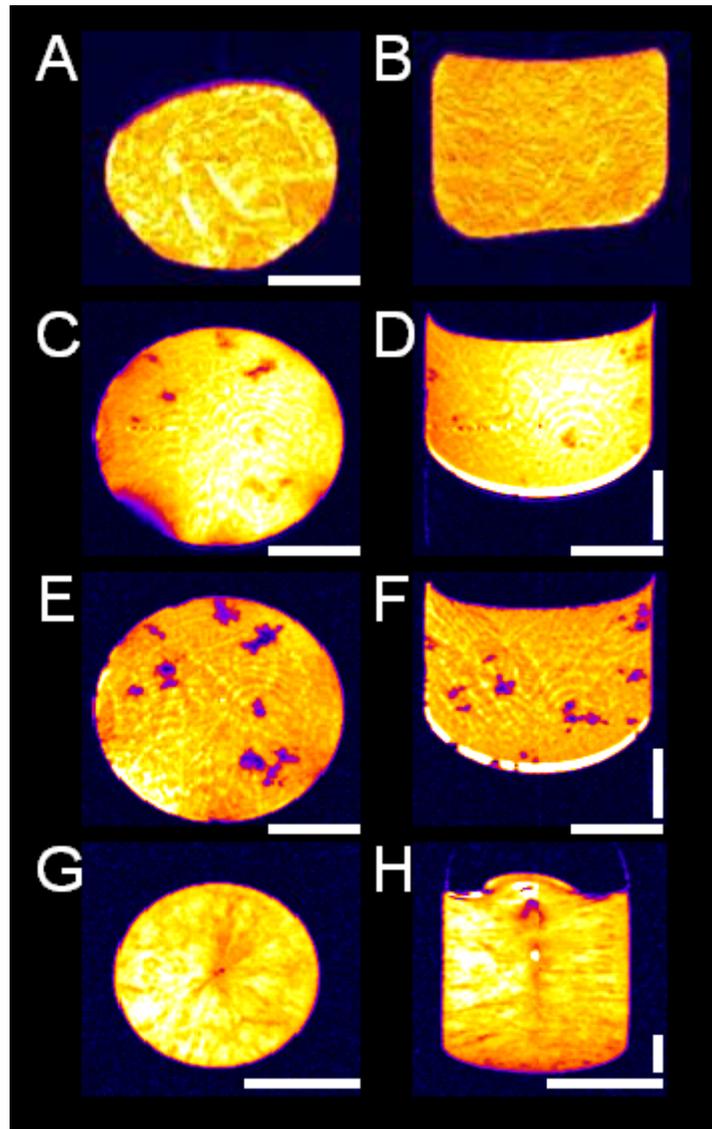
Figure 5.3.: Brine patterns in frozen aqueous solutions. Cross-sections left, corresponding longitudinal sections on the right. (A)-(B) 2D spin echo single-slice image of distilled water at 269 K, cooled from 298 K at a rate of 0.3 K/min. FOV: 15×15 mm^2, MTX: (128 pxl)^2, slice thickness: 500 μm, T$_R$: 1000 ms, T$_E$: 1.9 ms, NA: 1, T$_{exp}$: 2.1 min. (C)-(D) 3D spin echo image of Medium I with 7% DMSO at 253 K, cross-section. FOV: $15 \times 15 \times 20$ mm^3, MTX: (128 pxl)^3, T$_R$: 1000 ms, T$_E$: 1.1 ms, NA: 2, T$_{exp}$: 9 h. (E)-(F) The same sample as in C-D but 3D gradient-echo image, otherwise identical conditions. T$_R$: 50 ms, T$_E$: 1 ms, NA: 2, T$_{exp}$: 28 min. (G)-(H) 3D gradient-echo image of Medium I with 7% DMSO at 253 K, after immersion in liquid N$_2$ (cooling rate: ca. 200 K/min). FOV: $12 \times 12 \times 36$ mm^3, MTX: (128 pxl)^3, T$_R$: 50 ms, NA: 2, T$_{exp}$: 28 min.

Since Fig. 5.2 implied that 3D MR images of aqueous solutions are possible down to at least 253 K, and so different imaging pulse sequences were tested on frozen culture medium at this temperature. As with the oocytes in Chapter 2 and the fossils in Chapter 4, spin-echo sequences gave good results (cf. Fig. 5.3C-D). In contrast to the fossil experiments, however, gradient-echo images yielded results comparable to those of spin-echo images, though the susceptibility gradients introduced by the formation of ice crystals in the solution resulted in a clear signal loss in the areas concerned (cf. Fig. 5.3E-F).

In vitrified samples, on the other hand, these susceptibility effects were mostly negligible (cf. Fig. 5.3G-H). Though promising in the long run, vitrification techniques are only just beginning to find large-scale cryobiotechnological applications (Liebermann et al., 2002; Shaw and Jones, 2003), and so the following experiments will focus on cryoprotocols involving crystalisation and on their three-dimensional investigation via spin-echo imaging techniques.

The next test concerned the characterisation of freezing in different cryo containers. In standard NMR glass tubes of 1 cm diameter (cf. Fig. 5.4A), the brine was usually distributed as already seen in Fig. 5.2, though modulated by the composition of the solution and by the cryoparameters (cf. Fig. 5.3). A notably high signal could always be observed at the bottom of the tube and often at the other surfaces to the glass as well as to the air. The same effects occured in teflon capillaries of about 1 mm inner diameter (cf. Fig. 5.4B).
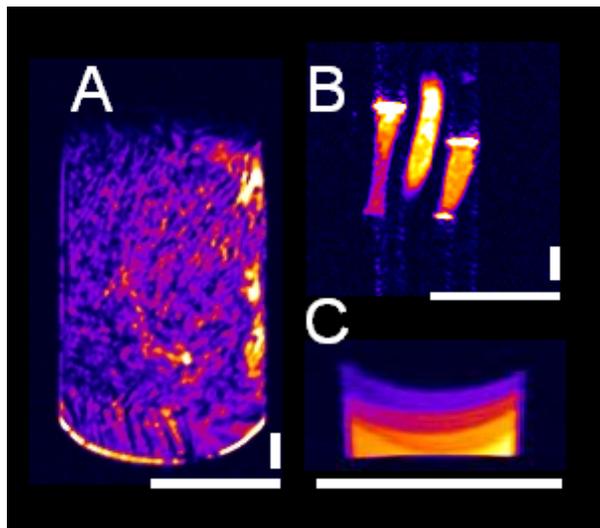
Figure 5.4.: 3D MR images of aqueous solutions frozen in different cryo containers, all recorded at 253 K. (A) NMR glass tube containing isotonic Modified Barth's Medium as used for the experiments in Chapter 3. FOV: $10 \times 10 \times 40$ mm^3, MTX: $128 \times 128 \times 256$ pxl^3, T_R: 830 ms, T_E: 1.3 ms, NA: 2, T_{exp}: 15 h. (B) Tetrafluormethane tubes of 1 mm inner diameter containing pure DMEM (main constituent of Medium I). FOV: $10 \times 10 \times 40$ mm^3, MTX: $128 \times 128 \times 256$ pxl^3, T_R: 900 ms, T_E: 1.1 ms, NA: 2, T_{exp}: 16 h. (C) High-density polyethylene (HDPE) microwell containing DMEM with 5% DMSO and two polystyrene beads of 500 μm diameter (Microparticles GmbH, Berlin, Germany) which are out of the slice plane depicted here. FOV: $11 \times 11 \times 3.2$ mm^3, MTX: $(128$ pxl$)^3$, T_R: 500 ms, T_E: 1.3 ms, NA: 8, T_{exp}: 18 h.

In the micro wells used for cryopreservation at IBMT (see also Fig. 5.5), the very small sample size caused dehydration to become the most dominant effect: The experiment illustrated in Fig. 5.4C was performed with eight-fold averaging – each point was sampled twice in a row during four acquisitions cycles separated by 4.5 h. On the basis of the 25 μl of sample volume at the beginning of the experiment, the water loss was determined as being about 1 μl/h at 253 K for these HDPE microwells if they were left open.

The microwells could be closed in two ways – either via a tailoured removable lid or via heat-sealing with a plastic foil. Both options were tested and found to be well-compatible with MRI but since the heat, even if only applied to the upper part of the containers and only for about one second, can create supplementary stress for the cells, the first option was preferred and used for all of the following experiments if not mentioned otherwise.
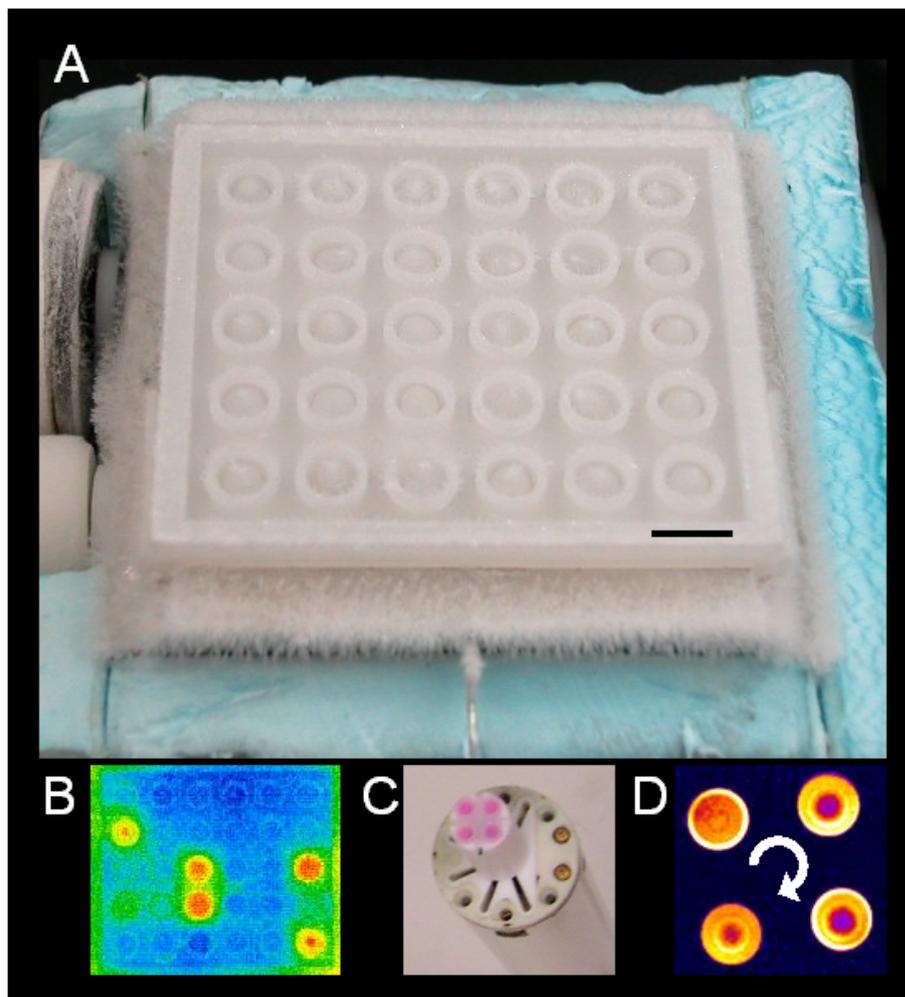
Figure 5.5.: Setup for 3D MRM in microwell plates (A) Overall appearance of a 6×5 HDPE array of microwell cryo containers (without lids), here filled with 25 μl (three leftmost columns) and 15 μl (three rightmost columns) of distilled water. Image taken at a stage temperature of 253 K. (B) Infrared thermographic image of the HDPE microwell array depicted in (A) at 259 K. (C) Positioning of a 2×2-container sample on the probe head (microwell lid and MR probe removed for better visibility). (D) 3D spin-echo image slice of Medium I with different concentrations of DMSO. Here and in the following MR images, the individual cryo containers within this 2×2 arrangement will be referred to by their encircled Arabic numeral in clockwise order, starting at the upper left, as indicated by the arrow: ①: 2.5% DMSO, ②: 5% DMSO, ③: 10% DMSO, ④: no DMSO. FOV: 11.5×11.5×3.2 mm^3, MTX: (128 pxl)^3, T$_R$: 820 ms, T$_E$: 1.3 ms, NA: 4, T$_{exp}$: 15 h.

Another feature of the microwells was that they were rarely planar at the bottom. In Fig. 5.4C, the position of the bottom-most pixels with above-noise MR signal varied by about four pixels (corresponding to 100 μm, the typical dimension of the effect) between the individual columns of the image slice. The shape of the inferred HDPE meniscus was convex here but concave in other instances, and no correlation could be found between the inclination of a container's bottom plane and its position or orientation within the entire 6×5 HDPE microwell array.

An example of these arrays is given in Fig. 5.5A. Here, the lids have been left aside so as to reveal the concentric ice growth pattern that developed after placing distilled water in the cryo containers at freezing temperatures. On the cryostage installed at IBMT (cf. Zimmermann et al., 2004), this growth process could also be monitored in time, as examplified by the thermographic image depicted in Fig. 5.5B in which the radial distribution of crystalisation heat (red) confirms the concentric crystal growth.

Besides, it should perhaps be noted that the thermography system was designed for wells without lids, as they absorb the infrared wavelengths measured by the thermocamera. When experimenting with open microwells, however, the high dehydration rates observed in samples like the one depicted in Fig. 5.4C should be kept in mind. Preliminary tests indicate that polyethylene foil as it is commonly used for food packaging in the household provided an acceptable remedy for that – its low thickness of about 50μm made it almost transparent to IR, while still limiting the water loss almost as effectively as the HDPE lids.

Fig. 5.5B also illustrates that ice crystal formation is a highly stochastic process: even though the 15 microwells on either side of the array had all been filled with the same amount of water (25 μl and 15 μl, respectively) and then treated identically, crystalisation does not occur in all containers at the same time.

The stochastic nature of ice nucleation is not readily accessible to a low-throughput technique like MR microimaging, especially under the additional constraint of signal losses due to freezing. Nonetheless, the measurements presented so far indicate that cryo-processing parameters are at least principally accessible to MR imaging. To this end, the spatial arrangement of the cryo containers subjected to MRI was kept constant for the rest of the experiments described in this section: As illustrated in Fig. 5.5C, a 2×2 microwell array was cut out of the 6×5 matrix, filled with the samples of interest, closed with a corresponding 2×2 lid cut out of a 6×5 template, and positioned in the centre of the MR probe by means of a hollow tetrafluormethane spacer that allowed for equal temperature control across all four microwells by means of the N_2 gas flow described in Section 5.3.2.
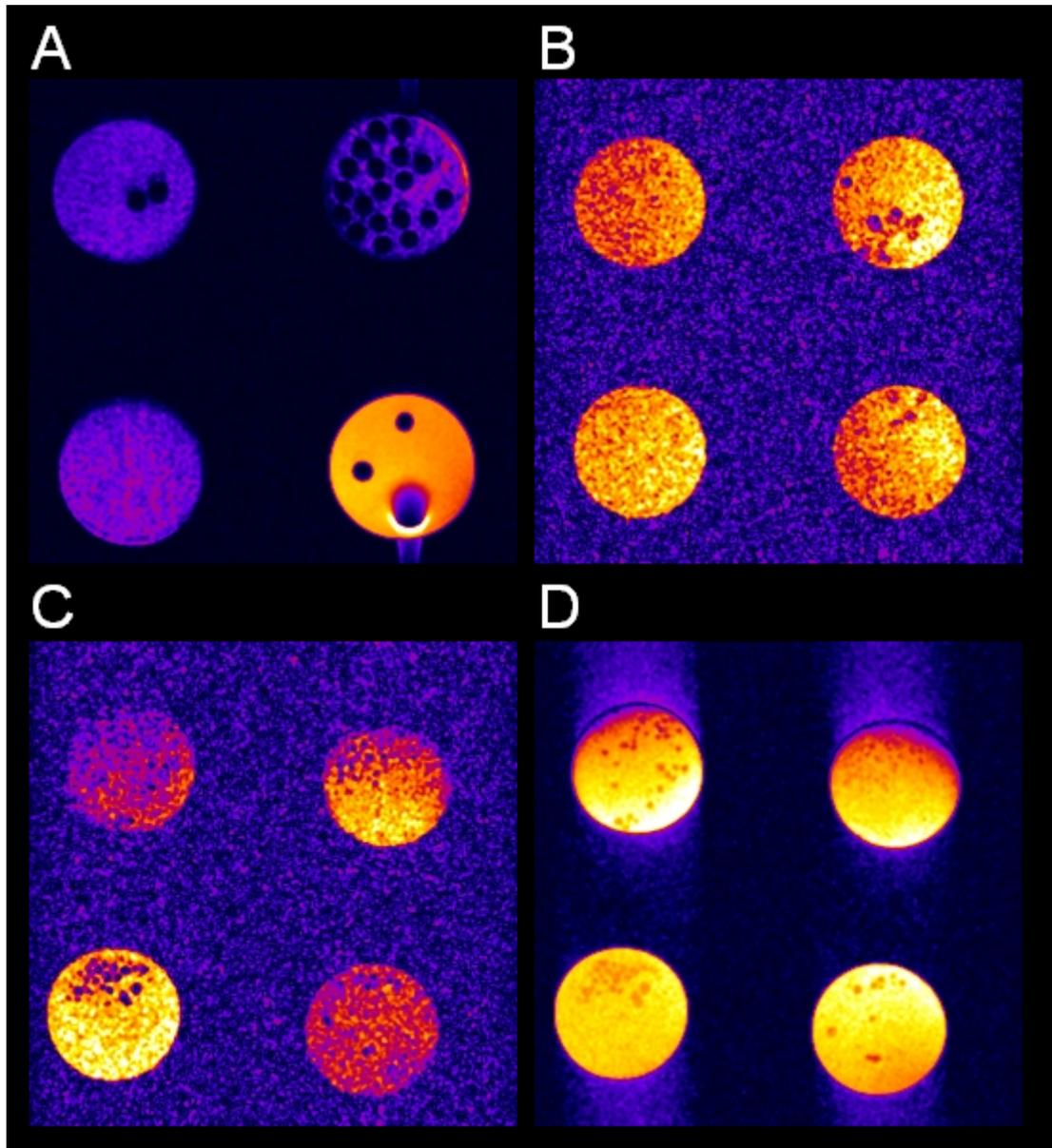
Figure 5.6.: 3D MRM of frozen suspensions. (A) 3D spin-echo image slice of different numbers of poly-methylmethacrylate (PMMA) beads (Microparticles GmbH, Berlin, Germany; charge PMMA-F-L1137) of 500 μm diameter in Medium I with 7% DMSO at 233 K. FOV: $11{\times}11{\times}3$ mm^3, MTX: $256{\times}256{\times}128$ pxl^3, T_R: 1000 ms, T_E: 3 ms, NA: 2, T_{exp}: 18 h. ①: 2 beads, ②: 20 beads (one is out of the image plane), ③: 2 beads, ④: no beads. Note the susceptibility artifact caused by an air bubble in container ④. (B) RARE 3D image of L929 tumor spheroids in Medium II at 290 K, with different cryoprotectants (at isoosmotic concentrations) in the place of trehalose. ①: unspecified cryoprotectant, ②: dextrin, ③: trehalose, ④: 1:1 mixture of the unspecified cryoprotectant and trehalose. FOV: $12{\times}12{\times}4$ mm^3, MTX: $256{\times}256{\times}128$ pxl^3, T_R: 1000 ms, T_E: 6.3 ms, NA: 2, RARE factor = 32, T_{exp}: 41 min. (C) RARE 3D image of a different sample of L929 tumor spheroids in Medium I with or without isoosmotic trehalose at 273 K. ①: trehalose, ②: no trehalose, ③: trehalose, ④: no trehalose. FOV: $12{\times}12{\times}4$ mm^3, MTX: $256{\times}256{\times}128$ pxl^3, T_R: 1000 ms, T_E: 6.3 ms, NA: 2, RARE = 32, T_{exp}: 41 min. (D) RARE 3D image of the L929 sample as in C, at 253 K. FOV: $12{\times}12{\times}4$ mm^3, MTX: $256{\times}256{\times}128$ pxl^3, T_R: 500 ms, T_E: 6.3 ms, NA: 12, RARE = 4, T_{exp}: 15 h.
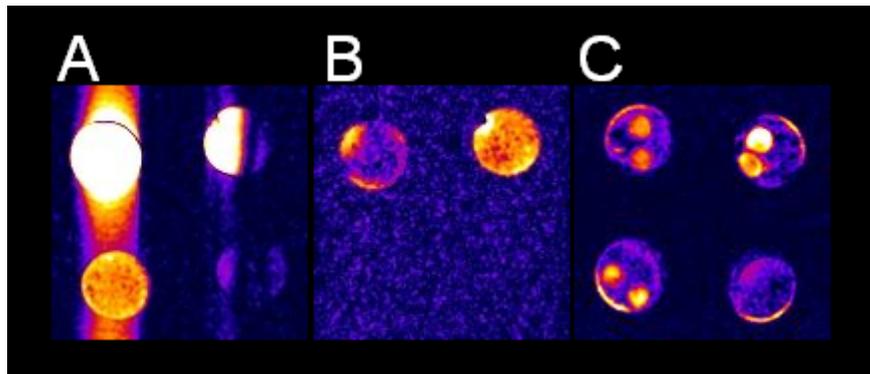
Figure 5.7.: 3D MR image slice of frozen tissue samples. (A) RARE 3D image of PC3 tumor spheroids at 253 K. FOV: $12\times12\times4$ mm^3, MTX: $128\times128\times64$ pxl^3, T_R: 1000 ms, T_E: 2.5 ms, NA: 4, RARE = 32, T_{exp}: 20 min. (B) RARE 3D image of the same sample as in A, at 233 K. FOV: $12\times12\times4$ mm^3, MTX: $128\times128\times64$ pxl^3, T_R: 1000 ms, T_E: 2.5 ms, NA: 2, RARE = 4, T_{exp}: 1.3 h. (C) Spin-echo 3D image of *Xenopus* oocytes at 253 K. FOV: $12\times12\times4.4$ mm^3, MTX: $(128$ pxl$)^3$, T_R: 750 ms, T_E: 1.3 ms, NA: 2, T_{exp}: 7 h. in Barth's medium. ①: 2 out of 2 dejellied oocytes in this micro well, ②: 2 out of 5 undejellied oocytes (the others are out of the image plane), ③: single undejellied oocyte, out of the image plane, ④: 2 out of two dejellied oocytes that had developed a TBE in one of the experiments described in Section 3.4.2. FOV: $12\times12\times4.4$ mm^3, MTX: $128\times128\times128$ pxl^3, T_R: 750 ms, NA: 4, TA: 14 h.

The resulting MR images confirmed the previously observed radial symmetry characteristic of sample solutions frozen in the HDPE microwells, and they allowed the simultaneous characterisation of samples whose cryoprocessing differed only in a small set of preselected parameters, e.g. cryoprotectant concentration in the culture medium (Fig. 5.5D).

5.4.2. *In glacie* **MRM of cells and tissues**

On the way to cell and tissue samples, microbeads of known diameters were tested for visibility in MR images (Fig. 5.6A) and found to be reliably detectable down to about 100μm, which is already below the upper size range of L929 tumor spheroids (cf. Fig. 5.6B-D). However, the information that can be obtained from images like the one depicted in Fig. 5.6A is not limited to pure spatial resolution (which would be $43\times43\times23$ μm in the given case), since they provide sufficient contrast to differentiate between brine, polymer beads and air bubbles. The latter were often found in microwells that had been manually covered with the lids, and they do not only cause susceptibility artifacts but also interfer with the freezing process and thus have to be avoided.

The samples in the previous chapter as well as those presented in this chapter until Fig. 5.6A did not contain living organisms (at least none of interest for this thesis) but cryopreservation is clearly directed towards living samples and keeping them alive, and under such conditions, imaging time becomes relevant. Therefore, faster alternatives to spin-echo sequences were tested on tumor spheroids. One such alternative, already discussed above, are gradient-echo schemes but they did not perform well on frozen samples.
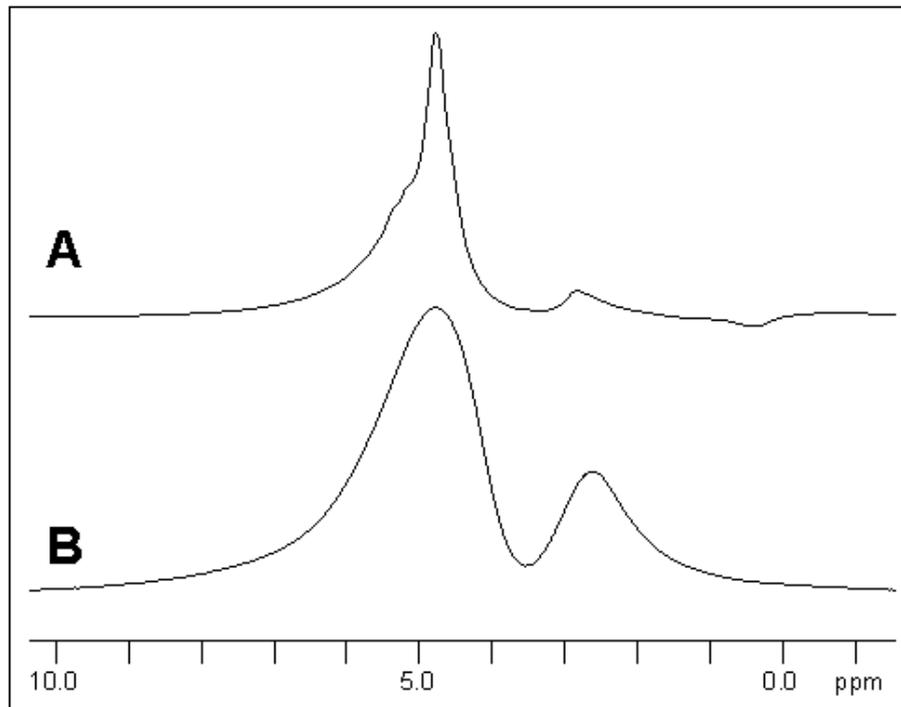
Figure 5.8.: [1]H spectra of an *Epiblema* larva at 233K (A) and 213K (B). The broad peak referenced to 4.7 ppm covers the hydroxyl groups of water and glycerol, the smaller one at about 2.5 ppm the CH and CH_2 groups of glycerol. Original intensity scale in (A) was reduced by a factor of 3.6 to fit that of (B).

Another technique (dubbed Rapid Acquisition with Relaxation Enhancement, or RARE, Hennig et al., 1984) uses multiple refocussing pulses (with a flip angle of $\theta = \pi$) per excitation pulse and phase-encodes the recorded signal such that multiple lines (whose number is commonly referred to as the RARE factor) in $\vec{k}$-space can be scanned simultaneously, thereby economising time to the expense of signal intensity and image details.

This method worked reasonably well with L929 tumor spheroids at different temperatures (cf. Fig. 5.6B-D) but also reached its limits once the samples were completely frozen, as demonstrated with PC3 spheroids in Fig. 5.7A-B. Therefore, from the perspective of MRI, supercooling strategies as they are employed by the cold-hardy insects *Epiblema scudderiana* and *Eurosta solidaginis* (cf. Section 5.2) provide a complementary opportunity to investigate how living tissues can cope with cold stress and why others (e.g. *Xenopus* oocytes, cf. Fig. 5.7C) can not.

5.4.3. *In glacie* **MRM of insects**

Fig. 5.8 shows ^{1}H MR spectra obtained from an *Epiblema* larva at 233 K and 213 K. The spectra contain just two broad peaks which can be associated with hydroxyl groups from both water and glycerol and with methyl groups from the glycerol backbone. Peak broadening with decreasing temperature and temperature-associated shifts of the methyl peak relative to the water resonance can be observed and become even more pronounced when compared to the localised spectra obtained from *Xenopus* oocytes at 294 K (cf. Fig. 2.6B).

Broad peaks in MR spectra result from short T_2 relaxation times, i.e. quick signal decay (cf. 1.5). Nonetheless, MR images could be acquired that provide detailed insights into the morphology of the larva at 233 K (cf. Fig. 5.9), revealing details such as tracheal openings, musculature, visceral organs and the brain. In Fig. 5.9B, the contours of the anterior segments appear slightly blurred due to a movement artifact that testifies to the vitality of the animal.

Images recorded at the same temperature after selective excitation of the hydroxyl and methyl resonances (as determined from the spectra in Fig. 5.8) are given in Fig. 5.9C-D and their almost perfect identity implies that water and glycerol were colocalised throughout the body, at least in terms of the pixel resolution achieved here (which was $25 \times 31 \times 31$ μm^3).

At 213 K, the signal intensity in the image was considerably reduced (cf. Fig. 5.9E-F), since most of the animal was now frozen. Some liquid pockets remained, though, and the water therein was still apparently colocalised with the cryoprotectant (cf. Fig. 5.9G-H). As a typical representative of a freeze-avoiding species, the *Epiblema* larva did not revive after having being frozen.

The situation was different with *Eurosta* (cf. Fig. 5.10): Already at 253 K, the water and lipid images (cf. Fig. 5.10C-D) were very distinct and almost complementary to each other with respect to images recorded after excitation of the whole width of the ^{1}H spectrum (cf. Fig. 5.10E) and which even allowed for individual cells and their nuclei to be identified in the lipid-rich regions. Moreover, the larva was partially frozen at 233 K but only in those areas where a high signal intensity could be observed in the water-selective images, while single non-frozen cells could still be identified in the regions that had appeared bright in the lipid image. *Eurosta* larvae are freeze-tolerant, and so the specimen described here successfully revived after the experiments.

5.5. Discussion

The experiments presented in this chapter have shown that three-dimensional microscopic MR images can be acquired from a variety of specimens under cryobiological conditions. These images reflect intrinsic properties of the samples or characteristics that they acquire or loose upon freezing. These include macroscopic crystal structures of frozen aqueous solutions and freezing homogeneity in different cryo containers, especially in the microwells in use here at IBMT, and even material properties of these containers.
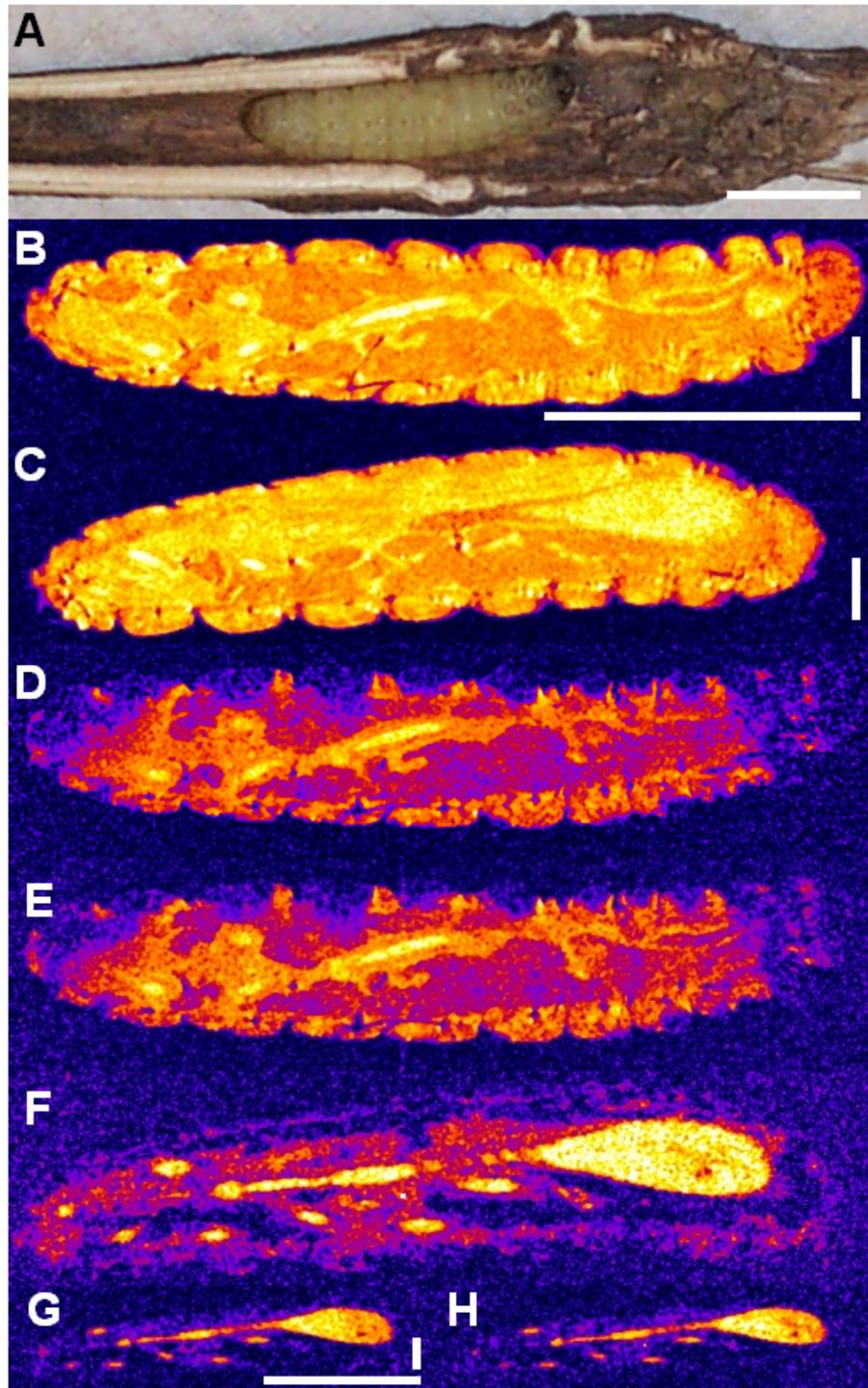
Figure 5.9.: 3D MRM of a supercooled *Epiblema* larva. (A) Photograph indicating the position of the insect (head is right) in the gall. Normal position both in nature and in the magnet is upright. This picture was taken after the experiment. 3D MR microscopic imaging was performed with the larva still positioned in the intact gall. Vertical scale bars in this figure represent 1 mm. (B) Mediolateral longitudinal MR cross-section at 233 K. FOV: $13\times4\times4$ mm^3, MTX: $512\times128\times128$ pxl^3, T_R: 1000 ms, T_E: 3.9 ms, NA: 2, T_{exp}: 9 h. The complete 3D image (in steps of 31μm) is provided as Movie 5.9 Ⓜ. (C) Dorsoventral longitudinal slice from the same 3D MR image. (D) The same slice position as in (B), imaged with selective excitation of the water resonances (cf. 5.8). T_R: 500 ms, T_E: 8.3 ms, NA: 2, T_{exp}: 4.5 h. (E) The same slice position as in (B), imaged with selective excitation of the lipid resonances (cf. 5.8). (F) Mediolateral longitudinal MRM cross-section at 213 K, acquired with the same MR parameters as in (B). (G) The same image slice as in (B), with selective excitation of the water resonances (cf. 5.8). FOV: $13\times4\times4$ mm^3, MTX: $256\times64\times64$ pxl^3, T_R: 1000 ms, T_E: 6.5 ms, NA: 2, T_{exp}: 2.3 h. (H) The same image slice as in (B), with selective excitation of the lipid resonances (cf. 5.8). FOV: $13\times4\times4$ mm^3, MTX: $256\times64\times64$ pxl^3, T_R: 1000 ms, T_E: 6.5 ms, NA: 2, T_{exp}: 2.3 h. The larva did not survive the experiment.

Furthermore, multicellular tissue samples could be detected in frozen or supercooled solutions and single cells within frozen organisms. Many of the tumor spheroids were found to float in their solution (data not shown), which will affect their freezing, and the same applies to air bubbles that are often present in lid-covered microwell samples and can not easily be detected otherwise.

The effects of cryoprocessing parameters (e.g. cryoprotectant concentration) on the freezing of aqueous solutions was also investigated but although MR imaging proved useful for such investigations in principle, it suffered from the stochastic nature of the freezing process. Freezing speed of distilled water has previously been reported to vary by as much as 5 orders of magnitude (Tabazadeh et al., 2002) under identical conditions.

Thermoimaging experiments with identical solutions under identical conditions also point into the same direction (cf. Fig. 5.5B), and so it has to be kept in mind that all the MR experiments – at least those without living tissue which might somehow control nucleation – were affected by mechanisms causing similar scatter.

Under these circumstances, the concentration on four-well arrays has to be regarded as preliminary: Even though the approach has its merit in terms of the feasibility study presented in here, it would have to receive significant modification – and perhaps support from other methodologies – in order to reach a state where different cryoprocessing schemes can be reliably evaluated for their efficiency in controlling parameters like nucleation speed, nucleation cluster size or the extent of vitrification. However, the foundations have been laid.

Besides, it would be desirable to have a wider range of cellular or cell-like model systems still in reach of routine pixel resolutions. Apart from the tumor spheroids described in here, encapsulation of tissue samples originating from humans or from biomedical model organisms represent such an option. The first steps in this direction have already been taken by MR studies of alginate microcapsules (Zimmermann et al., 2003), and the first MR experiments with rat pancreatic islets encapsulated this way and then frozen show that they can be detected as well.

One of the next steps then has to be the correlation of MR studies with viability tests of the biological materials, and given the zoo of parameters accessible to MR techniques, it would not be surprising to find MR proxies for viability before, during or after cryopreservation. Spin-echo sequences surely provide a good starter but gradient-echo techniques should perhaps receive another evaluation once vitrified biological samples become more readily available.
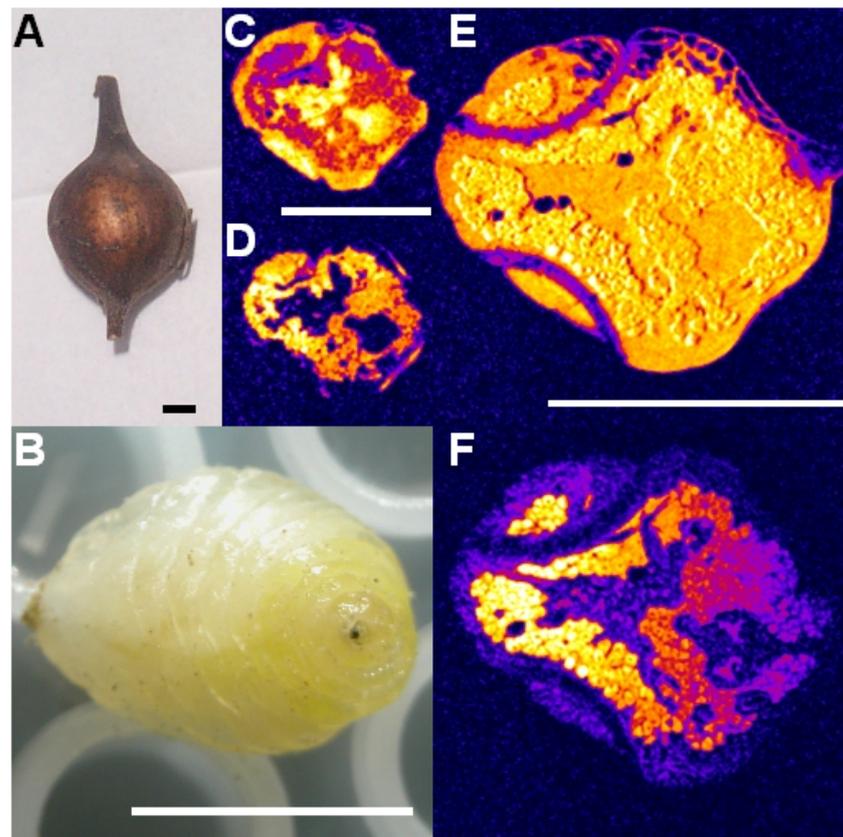
Figure 5.10.: 3D MRM of a *Eurosta* larva at different temperatures. (A) Photograph of the gall before the start of the experiment. The insect was removed from the gall for the sake of spatial resolution. (B) Photograph taken after the experiment, indicating the positioning on the microwell plate. Note the yellowish appearance due to glycerol. (C) Mediolateral cross-section at 253 K, with selective excitation of the water resonances. (C)–(E) at 253 K. FOV: $7 \times 7 \times 3.5$ mm^3, MTX: $128 \times 128 \times 64$ pxl^3, T_R: 500 ms, T_E: 5.1 ms, NA: 2, T_{exp}: 2.3 h. (D) The same image slice as in (C), with selective excitation of the lipid resonances. (E) Corresponding image slice as in (C) at 243 K, with double resolution and excitation of the entire spectrum. FOV: $7 \times 7 \times 3.5$ mm^3, MTX: $256 \times 256 \times 128$ pxl^3, T_R: 1000 ms, T_E: 2.2 ms, NA: 2, T_{exp}: 18 h. The complete 3D image (in steps of 27μm and in an orientation perpendicular to the image slice depicted here) is provided as Movie 5.10 (M). (F) The same imaging conditions as in (E) but at 233 K. The larva did survive the experiment.

It should be kept in mind, however, that the multiparametric nature of MR can also easily complicate data analysis, as examplified by Fig. 5.6 where the higher signal intensity obtained with the cryoprotectant might seem counterintuitive but can be understood in terms of the sensitivity of RARE sequences to the reduction of T_2 due to the vitrifying activity of trehalose in the sample.

The situation is different with experiments involving cold-hardy organisms – as their evolution has already generated viable solutions to many of the technical problems related to cryopreservation approaches, they can serve as cryobiological model systems and already do so in many cases. Yet most of the insights gathered so far were obtained by invasive means, and so MR studies of species like *Epiblema scudderiana*, *Eurosta solidaginis* or *Polypedilum vanderplanki* might provide an interesting complement.

5.6. Outlook

To be of use in comparative studies, the image data resulting from three-dimensional investigations, have to be comparable themselves, i.e. they should fit into a common framework allowing to integratively store and link – in three spatial and perhaps additional dimensions – morphological, functional, developmental, pathological, evolutionary, genetic, cryobiological and other data acquired by different methods or under different conditions in the same model system as well as data obtained from comparisons across cryoprotocols, image acquisition protocols, or species.

The latter type of investigations, along with biodiversity studies, will increasingly profit from cryotechniques as a means of preservation, since the growing number of cryobanks and the improving quality of the preserved samples will eventually lead to cryobanks taking over museal functions for molecular, cellular and tissue samples.

Comparative data can also be obtained by parallel investigation of several specimens under identical or controllably varied conditions. For technical reasons, this has not yet become routine in MRM studies but the first steps in this direction have already been taken (Purea et al., 2004; Lazovic et al., 2005). With such systems in place, the increased throughput would soon bring about further applications in many fields, not only but especially in the life sciences.

Experiments at higher magnetic fields, with stronger gradients, more sophisticated electronic periphery or new pulse sequences can be expected to further stimulate investigations into the dynamics of biological systems. MR microimaging studies of frozen or fossilised samples, single cells or developing embryos are still limited in number and

scope but since the necessary equipment is being installed in more and more laboratories, such *in vivo* investigations will certainly contribute significantly to the understanding of, e.g., anhydrobiosis, biomineralisation, developmental biomechanics, or pathology.

Finally, since MR emphasises different characteristics of a sample under investigation than other imaging or spectroscopic modalities do, its combination with complementary approaches – namely with optical (Keller, 1978; Boppart et al., 1996; Concha and Adams, 1998; Wind et al., 2000; Huisken et al., 2004) and ultrasound microscopy (Foster et al., 1993; Lemor et al., 2004) or chromatographic techniques (Lacey et al., 2001) – harbours considerable promise.

Such methodological hybrids might even trigger off the development of entirely new tools that rely on the detection or manipulation of optical or acoustical parameters by means of the static field of the MR magnet or the transient fields associated with MR pulse sequences (or *vice versa*). Along with other ongoing developments in the MR field (reviewed in Glover and Mansfield, 2002; Ciobanu et al., 2003; Darrasse and Ginefri, 2003; Webb, 2005), this creates a promising environment for further applications in previously neglected branches of the life sciences.

Chapter 6. Conclusion of thesis

The work presented in this thesis was focused on the applicability of microscopic MR imaging to dehydrated biological specimens. To this end, the current limits of spatial and temporal resolution of MRM were tested in hydrated and dehydrated biological systems.

Starting off from the well-known capability of MRI to visualise structures within living tissues, it was demonstrated that miniaturised coils allow to acquire water images as well as localised water-suppressed spectra from subcellular compartments of the large *Xenopus laevis* oocytes. Developmental processes can likewise be followed conveniently in microscopic MR imaging series of *Xenopus* embryos.

An abnormal cleavage plane was observed in *Xenopus* during the third embryonic cell division. In contrast to earlier reports, the alteration was not found to be related to the magnetic field but, rather, to the removal of the jelly coat shortly after fertilisation. The presence of jelly coat was also the main determinant of whether the cortical pigmentation pattern of unfertilised eggs would show an influence exerted by the magnetic field.

Though fossils represent an extreme example of dehydration in biological systems, the small amount of residual water often allows the recording of microscopic MR images from invertebrate, vertebrate and plant fossils. This is of particular interest for studies of palaeopathological specimens whose rareness renders them especially precious, such that invasive analyses are not desirable.

Dehydration of biological specimens in response to cooling below the freezing point of water at 273 K can effectively be monitored by MRM down to about 200 K. Consequently, the method provides for very interesting possibilities to investigate cryoadaptations of cold-hardy species and to optimise cryobiotechnological procedures, even under the constraints of miniaturisation.

Taken together, these results demonstrate that the non-invasiveness of MR techniques, along with the achievable spatial, temporal and spectral resolutions, renders them a very versatile tool for the study of cellular, fossil and crybiological systems, provided that they are not entirely devoid of the major constituent of living beings – liquid water.

Bibliography

Abel, O.: Paläobiologie der Cephalopoden aus der Gruppe der Dibranchiaten, Gustav Fischer Verlag, Jena, 1916.

Aberhan, M., Bussert, R., Heinrich, W.-D., Schrank, E., Schultka, S., Sames, B., Kriwet, J., and Kapilima, S.: Palaeoecology and depositional environments of the Tendaguru Beds (Late Jurassic to Early Cretaceous, Tanzania), Mitt. Mus. f. Naturk. Berl. Geowiss. Reihe, 5, 19–44, 2002.

Abragam, A.: The Principles of Nuclear Magnetism, Clarendon, Oxford, 1961.

Acker, J. P. and McGann, L. E.: Protective effect of intracellular ice during freezing?, Cryobiology, 46, 197–200, 2003.

Aguayo, J. B., Blackband, S. J., Schoeniger, J., Mattingly, M. A., and Hinterman, M.: Nuclear magnetic resonance imaging of a single cell, Nature, 322, 190–191, 1986.

Ahrens, E. T., Rothbacher, U., Jacobs, R. E., and Fraser, S. E.: A model for MRI contrast enhancement using T_1 agents, Proc. Natl. Acad. Sci. USA, 95, 8443–8448, 1998.

Alarcón, V. B. and Elinson, R. P.: RNA anchoring in the vegetal cortex of the *Xenopus* oocyte, J. Cell Sci., 114, 1731–1741, 2001.

Albrecht, P. and Ourisson, G.: Biogenic substances in sediments and fossils, Angew. Chem. Int. Ed. Engl., 10, 209–225, 1971.

Alcaraz, J., Nelson, C. M., and Bissell, M. J.: Biomechanical approaches for studying integration of tissue structure and function in mammary epithelia, J. Mammary Gland. Biol. Neoplasia, 9, 361–374, 2004.

Allen, M. J., MacBenaris, K. W., Venkatasubramanian, P. N., and Meade, T. J.: Cellular delivery of MRI contrast agents, Chem. Biol., 11, 301–3–7, 2004.

Almendros, G., Zancada, M. C., González-Vila, F. J., Lesiak, M. A., and Álvarez-Ramis, C.: Molecular features of fossil organic matter in remains of the Lower Cretaceous fern *Weichselia reticulata* from Przenosza basement (Poland), Org. Geochem., 36, 1108–1115, 2005.

Alpert, P.: The discovery, scope, and puzzle of desiccation tolerance in plants, Plant Ecol., 151, 5–17, 2000.

Ambrosi, D. and Mollica, F.: On the mechanics of a growing tumor, Int. J. Eng. Sci., 40, 1297–1316, 2002.

Andrew, E. R.: Magic Angle Spinning in Solid State n. m. r. Spectroscopy, Phil. Trans. R. Soc. Lond. A, 299, 505–520, 1981.

Arendt, D. and Nübler-Jung, K.: Rearranging gastrulation in the name of yolk: evolution of gastrulation in yolk-rich amniote eggs, Mech. Dev., 81, 3–22, 1999.

Bada, J. L.: How life began on Earth: a status report, Earth Planet. Sci. Lett., 226, 1–15, 2004.

Baguñà, J. and Garcia-Fernàndez, J.: *Evo-Devo*: the Long and Winding Road, Int. J. Dev. Biol., 47, 705–713, 2003.

Ball, P.: H_2O — A biography of water, Phoenix, London, 2000.

Bandel, K. and Spaeth, C.: Structural differences in the ontogeny of some belemnite rostra, in Cephalopods present and past, edited by J. Wiedmann and J. Kullmann, pp. 247–271, Schweizerbart, Stuttgart, 1988.

Barnes, L. G.: The late Miocene dolphin *Pithanodelphis* Abel, 1905 (Cetacea: Kentriodontidae) from California, Contr. Sci. Nat. Hist. Mus. Los Angeles Co., 367, 1–27, 1985.

Bashirullah, A., Cooperstock, R. L., and Lipshitz, H. D.: RNA localization in development, Annu. Rev. Biochem., 67, 335–394, 1998.

Basu, S., Gerchman, Y., Collins, C. H., Arnold, F. H., and Weiss, R.: A synthetic multicellular system for programmed pattern formation, Nature, 434, 1130–1134, 2005.

Bates, A. L. and Hatcher, P. G.: Solid-state ^{13}C NMR studies of a large fossil gymnosperm from the Yallourn Open Cut, Latrobe Valley, Org. Geochem., 14, 609–617, 1989.

Beckenbach, A. T.: Age of Bacteria from Amber, Science, 270, 2015–2016, 1995.

Beemster, G. T., Fiorani, F., and Inze, D.: Cell cycle: the key to plant growth control?, Trends Plant Sci., 8, 154–158, 2003.

Behrensmeyer, A. K., Kidwell, S. M., and Gastaldo, R. A.: Taphonomy and paleobiology, Paleobiol., 26, 103–147, 2000.

Bell, J. D. and Taylor-Robinson, S. D.: Assessing gene expression in vivo: magnetic resonance imaging and spectroscopy, Gene Ther., 7, 1259–1264, 2000.

Black, S. D. and Vincent, J. P.: The first cleavage plane and the embryonic axis are determined by separate mechanisms in *Xenopus laevis*. II. Experimental dissociation by lateral compression of the egg, Dev. Biol., 128, 65–71, 1988.

Blair, J. E., Shah, P., and Hedges, S. B.: Evolutionary sequence analysis of complete eukaryote genomes, BMC Bioinformatics, 6, 53, 2005.

Bloembergen, N., Purcell, E. M., and Pound, R. V.: Relaxation Effects in Nuclear Magnetic Resonance Absorption, Phys. Rev., 73, 679–712, 1948.

Blumer, M.: Organic pigments: their long-term fate, Science, 149, 722–726, 1965.

Blümich, B. and Kuhn, W., eds.: Magnetic resonance microscopy: methods and applications in materials science, agriculture and biomedicine, VCH, Weinheim, Basel, Cambridge, New York, 1992.

Boppart, S. A., Brezinski, M. E., Bouma, B. E., Teamey, G. J., and Fujimoto, J. G.: Investigation of developing embryonic morphology by using optical coherence tomography, Dev. Biol., 177, 54–63, 1996.

Borah, B., Gross, G. J., Dufresne, T. E., Smith, T. S., Cockman, M. D., Chmielewski, P. A., Lundy, M. W., Hartke, J. R., and Sod, E. W.: Three-dimensional microimaging (MRmicroI and microCT), finite element modeling, and rapid prototyping provide unique insights into bone architecture in osteoporosis, Anat. Rec., 265, 2001.

Borgia, G. C., Camaiti, M., Cerri, F., Fantazzini, P., and Piacenti, F.: Study of water penetration in rock materials by Nuclear Magnetic Resonance Tomography: hydrophobic treatment effects, J. Cult. Heritage, 1, 127–132, 2000.

Bottomley, P. A.: Spatial localization in NMR spectroscopy in vivo, Ann. N. Y. Acad. Sci., 508, 333–348, 1987.

Boyce, C. K., Hazen, R. M., and Knoll, A. H.: Nondestructive, in situ, cellular-scale mapping of elemental abundances including organic carbon in permineralized fossils, Proc. Natl. Acad. Sci. USA, 98, 2001.

Briggs, D. E. G.: The role of decay and mineralization in the preservation of soft-bodied fossils, Annu. Rev. Earth Planet. Sci., 31, 2003.

Brocks, J. J., Logan, G. A., Buick, R., and Summons, R. E.: Archean Molecular Fossils and the Early Rise of Eukaryotes, Science, 285, 1033–1036, 1999.

Brodland, G. W. and Veldhuis, J. H.: Computer simulations of mitosis and interdependencies between mitosis orientation, cell shape and epithelia reshaping, J. Biomech., 35, 673–681, 2002.

Bursac, P., Lenormand, G., Fabry, B., Oliver, M., Weitz, D. A., Viasnoff, V., Butler, J. P., and Fredberg, J. J.: Cytoskeletal remodelling and slow dynamics in the living cell, Nat. Mater., 4, 557–561, 2005.

Byers, T. J. and Armstrong, P. B.: Membrane protein redistribution during *Xenopus* first cleavage, J. Cell Biol., 102, 2176–2184, 1986.

Calder, M. G.: A coniferous petrified forest in Patagonia, Bull. Brit. Mus. (Nat. Hist.) Geology, 2, 99–138, 1953.

Callaghan, P. T.: Principles of Nuclear Magnetic Resonance Microscopy, Oxford University Press, Clarendon, 1991.

Callaghan, P. T. and Eccles, C.: NMR Studies on Antarctic Sea Ice, Bull. Magn. Reson., 18, 62–64, 1996.

Callaghan, P. T., Eccles, C. D., and Seymour, J. D.: An earth's field nuclear magnetic resonance apparatus suitable for pulsed gradient spin echo measurements of self-diffusion under Antarctic conditions, Rev. Sci. Instr., 68, 4263–4270, 1997.

Cano, R. J.: Age of Bacteria from Amber, Science, 270, 2016–2017, 1995.

Cano, R. J. and Borucki, M. K.: Revival and Identification of Bacterial Spores in 25- to 40-Million-Year-Old Dominican Amber, Science, 268, 1060–1064, 1995.

Chakeres, D. W., Bornstein, R., and Kangarlu, A.: Randomized Comparison of Cognitive Function in Humans at 0 and 8 Tesla, J. Magn. Reson. Imag., 18, 342–345, 2003.

Chalmers, A. D., Welchman, D., and Papalopulu, N.: Intrinsic differences between the superficial and deep layers of the *Xenopus* ectoderm control primary neuronal differen-

tiation, Dev. Cell, 2, 171–182, 2002.

Chalmers, A. D., Strauss, B., and Papalopulu, N.: Oriented cell divisions asymmetrically segregate aPKC and generate cell fate diversity in the early *Xenopus* embryo, Development, 130, 2657–2668, 2003.

Cherry, S. R.: In vivo molecular and genomic imaging: new challenges for imaging physics, Phys. Med. Biol., 49, R13–R48, 2004.

Ciobanu, L., Webb, A. G., and Pennington, C. H.: Magnetic resonance imaging of biological cells, Progr. NMR Spectr., 42, 69–93, 2003.

Clark, N. D., Adams, C., Lawton, T., Cruickshank, A. R., and Woods, K.: The Elgin marvel: using magnetic resonance imaging to look at a mouldic fossil from the Permian of Elgin, Scotland, UK, Magn. Reson. Imaging, 22, 2004.

Clarke, J. D. and Tickle, C.: Fate maps old and new, Nat. Cell Biol., 1, E103–E109, 1999.

Clegg, J. S.: Cryptobiosis – a peculiar state of biological organization, Comp. Biochem. Physiol. B, 128, 613–624, 2001.

Concha, M. L. and Adams, R. J.: Oriented cell divisions and cellular morphogenesis in the zebrafish gastrula and neurula: a time-lapse analysis, Development, 125, 983–994, 1998.

Crowe, J. H., Hoekstra, F. A., and Crowe, L. M.: Anhydrobiosis, Annu. Rev. Physiol., 54, 579–599, 1992.

Crowe, J. H., Carpenter, J. F., and Crowe, L. M.: The role of vitrification in anhydrobiosis, Annu. Rev. Physiol., 60, 73–103, 1998.

Dabos, K. J., Parkinson, J. A., Hewage, C., Nelson, L. J., Sadler, I. H., Hayes, P. C., and Plevris, J. N.: ^{1}H NMR spectroscopy as a tool to evaluate key metabolic functions of primary porcine hepatocytes after cryopreservation, NMR Biomed., 15, 241–250, 2002.

Daniel, B. L., Butts, K., and Block, W. F.: Magnetic Resonance Imaging of Frozen Tissues: Temperature-Dependent MR Signal Characteristics and Relevance for MR Monitoring of Cryosurgery, Magn. Reson. Med., 41, 627–630, 1999.

Danilchik, M. V. and Denegre, J. M.: Deep cytoplasmic rearrangements during early development in *Xenopus laevis*, Development, 111, 845–856, 1991.

Danilchik, M. V. and Gerhart, J. C.: Differentiation of the animal-vegetal axis in *Xenopus laevis* oocytes. I. Polarized intracellular translocation of platelets establishes the yolk gradient, Dev. Biol., 122, 101–112, 1987.

Darrasse, L. and Ginefri, J.-C.: Perspectives with cryogenic RF probes in biomedical MRI, Biochimie, 85, 915–937, 2003.

Darrow, B. S.: A fossil araucarian embryo from the Cerro Cuadrado of Patagonia, Bot. Gaz., 98, 328–337, 1936.

Dascal, N.: The use of *Xenopus oocytes* for the study of ion channels, CRC Crit. Rev. Biochem., 22, 317–387, 1987.

de Muizon, C.: Les vertébrés fossiles de la formation Pisco (Perou) III. Troisième partie:

Les Odontocètes (Cetacea, Mammalia) du Miocène, Inst. Fr. Ètud. And. Mèm., 78, 1–240, 1988.

De Robertis, E. M. and Sasai, Y.: A common plan for dorsoventral patterning in Bilateria, Nature, 380, 37–40, 1996.

de Swiet, T. M., Tomaselli, M., Hürlimann, M. D., and Pines, A.: In Situ NMR Analysis of Fluids Contained in Sedimentary Rock, J. Magn. Reson., 133, 385–387, 1998.

Deflandre, G.: Sur les microfossiles d'origine planctonique conservés à l'état de matière organique dans les silex de la craie, C. R. Acad. Sci., 199, 966–968, 1934.

Denegre, J. M., Valles, J. M., Lin, K., Jordan, W. B., and Mowry, K. L.: Cleavage planes in frog eggs are altered by strong magnetic fields, Proc. Natl. Acad. Sci. USA, 95, 14 729–14 732, 1998.

Dernbach, U., Jung, W., Selmeier, A., Götz, K., and Fine, H.: *Araucaria*. The petrified Araucarias from the Cerro Cuadrado, Argentina, D'Oro Verlag, Lorsch, 1992.

Dhenain, M., Ruffins, S. W., and Jacobs, R.: Three-dimensional digital mouse atlas using high-resolution MRI, Dev. Biol., 232, 458–470, 2001.

Dietrich, W.: Zur Stratigraphie und Palaeontologie der Tendaguruschichten, Palaeontographica, II (Suppl. VII, part 2), 1–86, 1933.

Dria, K. J., Sachleben, J. R., and Hatcher, P. G.: Solid-State Carbon-13 Nuclear Magnetic Resonance of Humic Acids at High Magnetic Field Strengths, J. Environ. Qual., 31, 393–401, 2002.

Dumont, F., Marechal, P.-A., and Gervais, P.: Cell Size and Water Permeability as Determining Factors for Cell Viability after Freezing at Different Cooling Rates, Appl. Environ. Microbiol., 70, 268–272, 2004.

Duval-Jouve, J.: Bélemnites des terraines inférieures des environs de Castellane, Basses Alpes, Paris, 1841.

Edelstein, W. A. and Schulson, E. M.: NMR imaging of salt-water ice, J. Glaciol., 37, 177–180, 1991.

Eglinton, G. and Logan, G. A.: Molecular preservation, Philos. Trans. R. Soc. Lond. B Biol. Sci., 333, 315–327, 1991.

Ehrenberg, C. G.: Mikrogeologie: Das Erden und Felsen schaffende Wirken des unsichtbar kleinen selbständigen Lebens auf der Erde, Leopold Voss, Leipzig, 1854.

Eicken, H., Bock, C., Wittig, R., Miller, H., and Poertner, H.-O.: Magnetic resonance imaging of sea-ice pore fluids: methods and thermal evolution of pore microstructure, Cold Regions Sci. Technol., 31, 207–225, 2000.

Elinson, R. P.: Amphibians, in Embryology: Constructing the Organism, edited by S. F. Gilbert and A. M. Raunio, pp. 436–439, Sinauer, Sunderland, Massachusetts, 1997.

Elinson, R. P. and Rowning, B.: A transient array of parallel microtubules in frog eggs: potential tracks for a cytoplasmic rotation that specifies the dorso-ventral axis, Dev. Biol., 128, 185–197, 1988.

Engel, M. H., Goodfriend, G. A., Qian, Y., and Macko, S. A.: Indigeneity of organic

matter in fossils: a test using stable isotope analysis of amino acid enantiomers in Quaternary mollusk shells, Proc. Natl. Acad. Sci. U S A, 91, 10 475–10 478, 1994.

Ernst, R. R., Bodenhausen, G., and Wokaun, A.: Principles of Nuclear Magnetic Resonance in One and Two Dimensions, Oxford University Press, Clarendon, 1997.

Erwin, D. H. and Davidson, E. H.: The last common bilaterian ancestor, Development, 129, 3021–3032, 2002.

Feng, Q. L., Li, H. B., Cui, F. Z., Li, H. D., and Kim, T. N.: Crystal orientation domains found in the single lamina in nacre of the *Mytilus edulis* shell, J. Mat. Sci. Lett., 18, 1547–1549, 1999.

Feng, Q. L., Li, H. B., Pu, G., Zhang, D. M., Cui, F. Z., Li, H. D., and Kim, T. N.: Crystallographic alignment of calcite prisms in the oblique prismatic layer of *Mytilus edulis* shell, J. Mat. Sci., 35, 3337–3340, 2000.

Feofilova, E. P.: Deceleration of Vital Activity as a Universal Biochemical Mechanism Ensuring Adaptation of Microorganisms to Stress Factors, Appl. Biochem. Microbiol., 39, 1–18, 2003.

Fernández-Jalvo, Y., King, T., Andrews, P., Moloney, N., Ditchfield, P., Yepiskoposyan, L., Safarian, V., Nieto Díaz, M., and Melkonyan, A.: Azokh Cave and Northern Armenia, in Miscelánea en Homenaje a Emiliano Aguirre, Volumen IV: Arqueología, edited by E. Baquedano and S. R. Jara, pp. 158–168, Museo Arqueológico Regional, Alcalá de Henares, 2004.

Fischman, J.: Have 25-Million-Year-Old Bacteria Returned to Life?, Science, 268, 977, 1995.

Fisher, P. E., Russell, D. A., Stoskopf, M. K., Barrick, R. E., Hammer, M., and Kuzmitz, A. A.: Cardiovascular Evidence for an Intermediate or Higher Metabolic Rate in an Ornithischian Dinosaur, Science, 288, 2000.

Florek, M., Youn, H. S., Ro, C.-U., Wierzbowski, H., Osán, J., Kazimierczak, W., and Kuczumow, A.: Investigation of chemical composition of belemnite rostra by synchrotron-based X-ray microfluorescence and diffraction and electron microprobe, J. Alloys Comp., 362, 2004.

Foster, F. S., Pavlin, C. J., Lockwood, G. R., Ryan, L. K., Harasiewicz, K. A., Berube, L., and Rauth, A. M.: Principles and applications of ultrasound backscatter microscopy, IEEE Trans. UFFC, 40, 608–617, 1993.

Freeman, S. B.: A study of the jelly envelopes surrounding the egg of the amphibian *Xenopus laevis*, Biol. Bull., 135, 501–513, 1968.

Freitas, C., Rodrigues, S., Saúde, L., and Palmeirim, I.: Running after the clock, Int. J. Dev. Biol., 49, 317–324, 2005.

Gabel, F., Bicout, D., Lehnert, U., Tehei, M., Weik, M., and Zaccai, G.: Protein dynamics studied by neutron scattering, Quart. Rev. Biophys., 35, 327–367, 2002.

Gerhart, J.: Evolution of the Organizer and the chordate body plan, Int. J. Dev. Biol., 45, 133–153, 2001.

Gerhart, J.: Changing the axis changes the perspective, Dev. Dyn., 225, 380–383, 2002.

Ghisalberti, E. L. and Godfrey, I. M.: Application of nuclear magnetic resonance spectroscopy to the analysis of organic archaeological materials, Stud. Conserv., 43, 215–230, 1998.

Gilbert, J. C., Rubinsky, B., Wong, S. T. S., Brennan, K. M., Pease, G. R., and Leung, P. P.: Temperature determination in the frozen region during cryosurgery of rabbit liver using MR image analysis, Magn. Reson. Imag., 15, 657–667, 1997.

Gilbert, S. F.: Developmental Biology, Sinauer Associates, Sunderland, Massachusets, 6th ed., 2000.

Gilbert, S. F.: The morphogenesis of evolutionary developmental biology, Int. J. Dev. Biol., 47, 467–477, 2003.

Gingras, M. K., MacMillan, B., Balcom, B. J., Saunders, T., and Pemberton, S. G.: Using Magnetic Resonance Imaging and Petrographic Techniques to Understand the Textural Attributes and Porosity Distribution in *Macaronichnus*-Burrowed Sandstone, J. Sedim. Res., 72, 552–558, 2002.

Glover, P. and Mansfield, P.: Limits to magnetic resonance microscopy, Rep. Prog. Phys., 65, 2002.

Gothan, W.: Sobre Restos de Plantas fosíles procedentes de la Patagonia, Bol. Acad. Nac. Cienc. Cordóba, 28, 197–212, 1925.

Götting, K.-J.: Malakozoologie, Gustav Fischer Verlag, Stuttgart, 1974.

Grant, S. C., Aiken, N. R., Plant, H. D., Gibbs, S., Mareci, T. H., Webb, A. G., and Blackband, S. J.: NMR spectroscopy of single neurons, Magn. Reson. Med., 44, 19–22, 2000.

Gripp, K.: Erdgeschichte von Schleswig-Holstein, Wachholtz, Neumünster, 1964.

Gruetter, R., Adriany, G., Merkle, H., and Anderson, P. M.: Broadband decoupled, ^{1}H localized ^{13}C MRS of the human brain at 4 tesla, Magn. Reson. Med., 36, 659–664, 1996.

Gusseck, D. J. and Hedrick, J. L.: A molecular approach to fertilization. I. Disulfide bonds in *Xenopus laevis* jelly coat and a molecular hypothesis for fertilization, Dev. Biol., 25, 337–347, 1971.

Hakumäki, J. M. and Kauppinen, R. A.: 1H NMR visible lipids in the life and death of cells, Trends Biochem. Sci., 25, 357–362, 2000.

Hampe, O.: Bestandsaufnahme der Walfauna (Mammalia: Cetacea) aus dem untersten Obermiozän (oberes Langenfeldium) von Groß Pampau (Schleswig-Holstein), Ber. Ver. "Nat. Heimat" Naturhist. Mus. Lübeck, 25/26, 87–107, 1999.

Hansch, C. and Leo, A. J.: Exploring QSAR: Fundamentals and applications in chemistry and biology, American Chemical Society, Washington, 1995.

Hausen, P. and Riebesell, M.: The Early Development of *Xenopus Laevis*: an atlas of histology, Springer, Berlin, 1991.

Hedrick, J. L. and Nishihara, T.: Structure and function of the extracellular matrix of

anuran eggs, J. Electron Microsc. Tech., 17, 319–335, 1991.

Hennig, J., Nauerth, A., Friedburg, H., and Ratzel, D.: Ein neues Schnellbildverfahren für die Kernspintomographie, Radiologe, 24, 579–580, 1984.

Hindmarsh, J. P., Buckley, C., Russell, A. B., Chen, X. D., Gladden, L., Wilson, D. I., and Johns, M. L.: Imaging droplet freezing using MRI, Chem. Engin. Sci., 59, 2113–2122, 2004.

Hinsch, W.: Biostratigraphy of Reinbekian/ Levensauian/ Lüneburgian/ Langenfeldian boundary stratotypes in Pampau area (SE-Holstein), Veröff. Übersee-Mus. Bremen R. A, 10, 55–79, 1990.

Hinton, H. E.: A Fly Larva that tolerates Dehydration and Temperatures from -270°C to +102°C, Nature, 188, 336–337, 1960.

Hinton, H. E.: Reversible suspension of metabolism and the origin of life, Proc. Roy. Soc. Lond. B, 171, 43–57, 1968.

Höpfner, G.: Wale und Haie - aus der Urzeit aufgetaucht, Z. Nat. Landeskd. S-H u.Hambg., 98, 245–253, 1991.

Horowitz, S. B.: The permeability of the amphibian oocyte nucleus, *in situ*, J. Cell. Biol., 54, 609–625, 1972.

Horowitz, S. B. and Pearson, T. W.: Intracellular Monosaccharide and Amino Acid Concentrations and Activities and the Mechanism of Insulin Action, Mol. Cell. Biol., 1, 769–784, 1981.

Hoult, D. I. and Richards, R. E.: Signal-to-noise ratio of nuclear magnetic resonance experiment, J. Magn. Reson., 24, 71–85, 1976.

Hughes, N. C.: Trilobite body patterning and the evolution of arthropod tagmosis, Bioessays, 25, 386–395, 2003.

Huisken, J., Swoger, J., Del Bene, F., Wittbrodt, J., and Stelzer, E. H. K.: Optical sectioning deep inside live embryos by selective plane illumination microscopy, Science, 305, 1007–1009, 2004.

Ingber, D. E.: Tensegrity II. How structural networks influence cellular information processing networks, J. Cell Sci., 116, 1397–1408, 2003.

Iwasaka, M., Ueno, S., and Shiokawa, K.: Cleavage pattern modulation of frog's egg under magnetic fields of 10 tesla order, Int. J. Appl. Electromagn. Mech., 14, 327–330, 2001.

Jackson, A. P., Vincent, J. F. V., and Turner, R. M.: The Mechanical Design of Nacre, Phil. Trans. R. Soc. Lond. B, 234, 415–440, 1988.

Jacobs, R. E. and Fraser, S. E.: Magnetic resonance microscopy of embryonic cell lineages and movements, Science, 263, 681–684, 1994.

Janensch, W.: Die Gliederung der Tendaguru-Schichten im Tendaguru-Gebiet und die Entstehung der Saurier-Lagerstätten, Archiv Biontol., 3, 227–261, 1914.

Kasimova, R. M.: Anthropological research of Azykh Man osseous remains, Human Evol., 16, 37–44, 2001.

Kay, B. K. and Peng, H. B.: *Xenopus laevis*: Practical uses in cell and molecular biology, Academic Press, New York, in: Methods in Cell Biology, vol 36, 1991.

Kay, H. H., Herfkens, R. J., and Kay, B. K.: Effect of Magnetic Resonance Imaging on *Xenopus laevis* embryogenesis, Magn. Reson. Imaging, 6, 501–506, 1988.

Keating, T. J. and Cork, R. J.: Intracellular free calcium oscillations in normal and cleavage-blocked embryos and artificially activated eggs of *Xenopus laevis*, J. Cell Sci., 107, 2229–2237, 1994.

Keilin, D.: The Leeuwenhoek Lecture: The problem of anabiosis or latent life: history and current concept, Proc. Roy. Soc. Lond. B, 150, 149–191, 1959.

Keller, R.: Time-lapse cinemicrographic analysis of superficial cell behavior during and prior to gastrulation in *Xenopus laevis*, J. Morph., 157, 223–248, 1978.

Keller, R.: Early embryonic development of *Xenopus laevis*, in *Xenopus laevis*: Practical uses in cell and molecular biology, edited by B. K. Kay and H. B. Peng, Academic Press, New York, in: Methods in Cell Biology, vol 36, 1991.

Keller, R., Davidson, L. A., and Shook, D. R.: How we are shaped: the biomechanics of gastrulation, Differentiation, 71, 171–205, 2003.

Kerr, W. L., Kauten, R. J., McCarthy, M. J., and Reid, D. S.: Monitoring the Formation of Ice During Food Freezing by Magnetic Resonance Imaging, Lebensm.-Wiss. u.-Technol., 31, 215–220, 1998.

Keupp, H.: Pathologische Ammoniten, Kuriositäten oder paläobiologische Dokumente. Teil 1, Fossilien, 6, 258–262, 1984.

Keupp, H.: Pathologische Ammoniten, Kuriositäten oder paläobiologische Dokumente. Teil 2, Fossilien, 1, 23–35, 1985.

Keupp, H.: Perlen (Schalenkonkretionen) bei Dactylioceraten aus dem fränkischen Lias, Jahresmitt. Naturhistor. Ges. Nürnberg 1986, pp. 97–102, 1987.

Keupp, H.: Pathologische Belemniten — Schein und Wirklichkeit, Fossilien, 2, 85–92, 2002.

Keupp, H. and Mita, V. V.: Septenbildung bei *Quenstedtoceras* (Ammonoidea) von Saratov (Russland) unter anomalen Kammerdruckbedingungen, Mitt. Geol.-Paläontol. Inst. Univ. Hamburg, 88, 51–62, 2004.

Kidwell, S. M. and Holland, S. M.: The quality of the fossil record: Implications for evolutionary analyses, Annu. Rev. Ecol. Syst., 33, 2002.

Koop, T.: Homogeneous Ice Nucleation in Water and Aqueous Solutions, Z. Phys. Chem., 218, 1231–1258, 2004.

Kusano, K., Miledi, R., and Stinnakre, J.: Acetylcholine receptors in the oocyte membrane, Nature, 270, 739–741, 1977.

Kwiatkowska, D.: Structural integration at the shoot apical meristem: models, measurements and experiments, Am. J. Bot., 91, 1277–1293, 2004.

Lacey, M. E., Tan, Z. J., Webb, A. G., and Sweedler, J. V.: Union of capillary high-performance liquid chromatography and microcoil nuclear magnetic resonance spec-

troscopy applied to the separation and identification of terpenoids, J. Chromatogr. A, 922, 139–149, 2001.

Ladner, M. B., Martin, G. A., Noble, J. A., Wittman, V. P., Kim Warren, M., McGrogan, M., and Stanley, E. R.: cDNA cloning and expression of murine macrophage colony-stimulating factor from L929 cells, Proc. Natl. Acad. Sci. USA, 85, 6706–6710, 1988.

Lall, S. and Patel, N. H.: Conservation and divergence in molecular mechanisms of axis formation, Annu. Rev. Genet., 35, 407–437, 2001.

Lambert, J. B., Shawl, C. E., and Stearns, J. A.: Nuclear magnetic resonance in archaeology, Chem. Soc. Rev., 29, 175–182, 2000.

Lambert, J. S. and Frye, J. S.: Carbon Functionalities in Amber, Science, 217, 55–57, 1982.

Lancaster, J. L., Woldorff, M. G., Parsons, L. M., Liotti, M., Freitas, C. S., Rainey, L., Kochunov, P. V., Nickerson, D., Mikiten, S. A., and Fox, P. T.: Automated Talairach atlas labels for functional brain mapping, Hum. Brain Map., 10, 120–131, 2000.

Larabell, C. A. and Le Gros, M. A.: X-ray tomography generates 3-D reconstructions of the yeast, *Saccharomyces cerevisiae*, at 60-nm resolution, Mol. Biol. Cell, 15, 957–962, 2004.

Lazovic, J., Stojkovic, D. S., Collins, C. M., Yang, Q. X., Vaughan, J. T., and Smith, M. B.: Hexagonal Zero Mode TEM coil: a single-channel coil design for imaging multiple small animals, Magn. Reson. Med., 53, 1150–1157, 2005.

Lee, A. P., Klinowski, J., and Marseglia, E. A.: Application of Nuclear Magnetic Resonance Spectroscopy To Bone Diagenesis, J. Archaeol. Sci., 22, 257–262, 1995.

Lee, C.-L., Linton, J., Soughayer, J. S., Sims, C. E., and Albritton, N. L.: Localized measurement of kinase activation in oocytes of *Xenopus laevis*, Nat. Biotechnol., 17, 759–762, 1999.

Lee, R. B. and Ratcliffe, R. G.: Observations on the subcellular distribution of the ammonium ion in maize root tissue using *in-vivo* ^{14}N-nuclear magnetic resonance spectroscopy, Planta, 183, 359–367, 1991.

Lee, R. B., Ratcliffe, R. G., and Southon, T. E.: ^{31}P-NMR measurements of the cytoplasmic and vacuolar P_i content of mature maize roots: relationship with phosphorus status and phosphate fluxes, J. Exp. Bot., 41, 1063–1078, 1990.

Lee, S.-C., Kim, K., Kim, J., Lee, S., Yi, J. H., Kim, S. W., Ha, K. S., and Cheong, C.: One micrometer resolution NMR microscopy, J. Magn. Reson., 150, 207–213, 2001.

Lemor, R., Pilarczyk, G., Westphal, I., and Weiss, E. C.: Combination of acoustic and optical microscopy for investigation of biological cell properties, in Acoustical Imaging Vol. 27, edited by W. Arnold and S. Hirsekorn, pp. 563–572, Kluwer, Dordrecht, New York, 2004.

Lens, P. N. L. and Hemminga, M. A.: Nuclear magnetic resonance in environmental engineering: Principles and applications, Biodegradation, 9, 393–409, 1998.

Levin, M.: Bioelectromagnetics in Morphogenesis, Bioelectromagnetics, 24, 2003.

Liebermann, J., Nawroth, F., Isachenko, V., Isachenko, E., Rahimi, G., and Tucker, M. J.: Potential Importance of Vitrification in Reproductive Medicine, Biol. Reprod., 67, 1671–1680, 2002.

Lodish, H., Berk, A., Zipursky, L. S., Matsudaira, P., Baltimore, D., and Darnell, J.: Molecular Cell Biology, Freeman, New York, 4th ed., 2000.

Longo, D., Peirce, S. M., Skalak, T. C., Davidson, L., Marsden, M., Dzamba, B., and DeSimone, D. W.: Multicellular computer simulation of morphogenesis: blastocoel roof thinning and matrix assembly in *Xenopus laevis*, Dev. Biol., 271, 210–222, 2004.

Louie, A. Y., Huber, M. M., Ahrens, E. T., Rothbacher, U., Moats, R., Jacobs, R. E., Fraser, S. E., and Meade, T. J.: *In vivo* visualization of gene expression using magnetic resonance imaging, Nat. Biotechnol., 18, 321–325, 2000.

Lucchetta, E. M., Lee, J. H., Fu, L. A., Patel, N. H., and Ismagilov, R. F.: Dynamics of *Drosophila* embryonic patterning network perturbed in space and time using microfluidics, Nature, 434, 1134–1138, 2005.

Luo, Z. and Eastman, E. R.: Petrosal and inner ear of a squalodontid whale: implications for evolution of hearing in odontocetes, J. Vert. Paleont., 15, 431–442, 1995.

Luo, Z. and Marsh, K.: Petrosal (periotic) and inner ear of a Pliocene kogiine whale (Kogiinae, Odontoceti): implications on relationships and hearing evolution of toothed whales, J. Vert. Paleont., 16, 328–348, 1996.

Lyons, P. D., Rioux, M., and Patterson, R. T.: Application of a Three-Dimensional Color Laser Scanner to Paleontology: an Interactive Model of a Juvenile *Tylosaurus* sp. Basisphenoid-Basioccipital, Palaeontol. Electron., 3, 4, 2002.

Malet-Martino, M. C. and Martino, R.: Magnetic resonance spectroscopy: a powerful tool for drug metabolism studies, Biochimie, 74, 785–800, 1992.

Mamman, M., Aliu, Y. O., and Peregrine, A. S.: Comparative pharmacokinetics of diminazene in noninfected Boran (*Bos indicus*) cattle and Boran cattle infected with *Trypanosoma congolense*, Antimicrob. Agents Chemother., 37, 1050–1055, 1993.

Manz, B., Volke, F., Goll, D., and Horn, H.: Measuring local flow velocities and biofilm structure in biofilm systems with magnetic resonance imaging (MRI), Biotechnol. Bioengin., 84, 424–432, 2003.

Mariette, F. and Lucas, T.: NMR Signal Analysis To Attribute the Components to the Solid/Liquid Phases Present in Mixes and Ice Creams, J. Agric. Food Chem., 53, 1317–1327, 2005.

Mathur, J.: Conservation of boundary extension mechanisms between plants and animals, J. Cell Biol., 168, 679–682, 2005.

McCoy, C. L., Parkins, C. S., Chaplin, D. J., Griffiths, J. R., Rodrigues, L. M., and Stubbs, M.: The effect of blood flow modification on intra- and extracellular pH measured by ^{31}P magnetic resonance spectroscopy in murine tumours, Br. J. Cancer, 72, 905–911, 1995.

Meinhardt, H.: Organizer and axes formation as a self-organizing process, Int. J. Dev.

Biol., 45, 177–188, 2001.

Melnichenko, N. A., Mikhaylov, V. I., and Chizik, V. I.: Izuchenie temperaturnoy za-visimosti otnositel'nogo soderzhaniya zhidkoy fazy v zamorozhennoy morskoy vode impul'snym metodom YaMR, Okeanologiya, 19, 535–537, 1979.

Menéndez, C. A.: Cono masculine de una conífera fósil del Bosque Petrificado de Santa Cruz, Ameghiniana, 2, 11–17, 1960.

Menzel, M. I., Han, S., Stapf, S., and Blümich, B.: NMR characterization of the pore structure and anisotropic self-diffusion in salt water ice, J. Magn. Reson., 143, 376–381, 2000.

Merriam, R. W., Sauterer, R. A., and Christensen, K.: A Subcortical, Pigment-Containing Structure in *Xenopus* Eggs with Contractile Properties, Dev. Biol., 95, 439–446, 1983.

Meyerowitz, E. M.: Plants compared to animals: the broadest comparative study of development, Science, 295, 1482–1485, 2002.

Meylan, W. M. and Howard, P. H.: Atom/fragment contribution method for estimating octanol-water partition coefficients, J. Pharm. Sci., 84, 83–92, 1995.

Mild, K. H., Sandstrom, M., and Lovtrup, S.: Development of *Xenopus laevis* embryos in a static magnetic field, Bioelectromagnetics, 2, 199–201, 1981.

Minard, K. R. and Wind, R. A.: Picoliter ^{1}H NMR spectroscopy, J. Magn. Reson., 154, 336–343, 2002.

Moore, S. W.: A fiber optic system for measuring dynamic mechanical properties of embryonic tissues, IEEE Trans. Biomed. Eng., 41, 45–50, 1994.

Mueller-Klieser, W.: Three-dimensional cell cultures: from molecular mechanisms to clinical applications, Am. J. Physiol., 273, C1109–C1123, 1997.

Naef, A.: Die fossilen Tintenfische, Gustav Fischer Verlag, Jena, 1922.

Nakashima, Y., Nakashima, S., Gross, D., Weiss, K., and Yamauchi, K.: NMR imaging of ^{1}H in hydrous minerals, Geothermics, 27, 43–53, 1998.

Nelson, C. M., Jean, R. P., Tan, J. L., Liu, W. F., Sniadecki, N. J., Spector, A. A., and Chen, C. S.: Emergent patterns of growth controlled by multicellular form and mechanics, Proc. Natl. Acad. Sci. USA, 102, 11 594–11 599, 2005.

Neubert, J., Schatz, A., Bromeis, B., and Linke-Hommes, A.: Effects of gravity on early development, Adv. Space Res., 22, 265–211, 1998.

Neurath, P. W.: High gradient magnetic field inhibits embryonic development of frogs, Nature, 219, 1358–1359, 1968.

Nieuwkoop, P. D. and Faber, J.: Normal Table of *Xenopus laevis* (Daudin): A Systematical and Chronological Survey of the Development from the Fertilized Egg till the End of Metamorphosis, North-Holland, Amsterdam, 1956.

Niklas, K. J. and Gensel, P. G.: Chemotaxonomy of some Paleozoic vascular plants. Part I: chemical compositions and preliminary cluster analyses, Brittonia, 28, 353–378, 1976.

Notman, D. N. H., Tashjian, J., Aufderheide, A. C., Cass, O. W., Shane III, O. C., Berquist, T. H., Gray, J. E., and Gedgaudas, E.: Modern Imaging and Endoscopic Biopsy

Techniques in Egyptian Mummies, Am. J. Radiol, 146, 93–96, 1986.

Orive, G., Hernandez, R. M., Gascon, A. R., Dominguez-Gil, A., and Pedraz, J. L.: Drug delivery in biotechnology: present and future, Curr. Opin. Biotechnol., 14, 659–664, 2003.

Ornstein, D. K., Gillespie, J. W., Paweletz, C. P., Duray, P. H., Herring, J., Vocke, C. D., Topalian, S. L., Bostwick, D. G., Linehan, W. M., Petricoin III, E. F., and Emmert-Buck, M. R.: .

Ourisson, G. and Nakatani, Y.: The terpenoid theory of the origin of cellular life: the evolution of terpenoids to cholesterol, Chem. Biol., 1, 11–23, 1994.

Pääbo, S., Poinar, H., Serre, D., Jaenicke-Després, V., Hebler, J., Rohland, N., Kuch, M., Krause, J., Vigilant, L., and Hofreiter, M.: Genetic analyses from ancient DNA, Annu. Rev. Gen., 38, 645–679, 2004.

Patel, N. H. and Lall, S.: Precision patterning, Nature, 415, 748–749, 2002.

Päuser, S., Keller, K., Zschunke, A., and Mügge, C.: Study of the membrane permeability of a paramagnetic complex on single cells by NMR microscopy, Magn. Reson. Imag., 11, 419–427, 1993.

Peck, T. L., Magin, R. L., and Lauterbur, P. C.: Design and Analysis of Microcoils for NMR Microscopy, J. Magn. Reson. B, 108, 114–124, 1995.

Penafiel, L. M., Litovitz, T., Krause, D., Desta, A., and Mullins, J. M.: Role of Modulation on the Effect of Microwaves on Ornithine Decarboxylase Activity in L929 Cells, Bioelectromagnetics, 18, 132–141, 1997.

Pfeuffer, J., Tkáč, I., and Gruetter, R.: Extracellular-intracellular distribution of glucose and lactate in the rat brain assessed noninvasively by diffusion weighted 1H nuclear magnetic resonance spectroscopy *in vivo*, J. Cereb. Blood Flow Metab., 20, 736–746, 2000.

Pfretzschner, H.-U.: Pyrite formation in Pleistocene bones - a case of very early mineral formation during diagenesis, N. Jb. Geol. Paläont. Abh., 217, 143–160, 2000.

Pilch, D. S., Kirolos, M. A., Liu, X., Plum, G. E., and Breslauer, K. J.: Berenil [1,3-bis(4'-amidinophenyl)triazene] binding to DNA duplexes and to a RNA duplex: evidence for both intercalative and minor groove binding properties, Biochemistry, 34, 9962–9976, 1995.

Pilleri, G., Gihr, M., and Kraus, C.: The organ of hearing in Cetaceans. 1. Recent species, Invest. Cetacea, 20, 43–125, 1987.

Podolsky, R. D.: Fertilization ecology of egg coats: physical *versus* chemical contributions to fertilization success of free-spawned eggs, J. Exp. Biol., 205, 1657–1668, 2002.

Poinar, G. O., Waggoner, B. M., and Bauer, U.-C.: Terrestrial soft-bodied protists and other microorganisms in Triassic amber, Science, 259, 222–224, 1993.

Poinar Jr., G. and Poinar, R.: The Amber Forest, Princeton University Press, Princeton, New Jersey, 1999.

Posse, S. and Aue, W. P.: Spectroscopic imaging and gradient-echo microscopy on a single cell, J. Magn. Reson., 83, 620–625, 1989.

Potts, M.: Mechanisms of desiccation tolerance in cyanobacteria, Eur. J. Physiol., 34, 319–328, 1999.

Pourquié, O.: The Segmentation Clock: Converting Embryonic Time into Spatial Pattern, Science, 301, 328–330, 2003.

Price, W. S., Ide, H., Arata, Y., and Ishikawa, M.: Visualisation of Freezing Behaviours in Flower Bud Tissues of Cold-hardy *Rhododendron japonicum* by Nuclear Magnetic Resonance Micro-Imaging, Aust. J. Plant Physiol., 24, 599–605, 1997.

Priest, F. G.: Age of Bacteria from Amber, Science, 270, 2015–2016, 1995.

Prusinkiewicz, P.: Modeling plant growth and development, Curr. Opin. Plant Biol., 7, 79–83, 2004.

Purea, A., Neuberger, T., and Webb, A. G.: Simultaneous NMR Microimaging of Multiple Single-Cell Samples, Conc. Magn. Reson. B, 22, 7–14, 2004.

Radwánska, U. and Radwánski, A.: Disease and trauma in Jurassic invertebrate aminals of Poland — an updated review, Tomy Jurajskie (Warszawa), 2, 99–111, 2004.

Richardson, C. and Keller, E. E.: The brine content of sea ice measured with a nuclear magnetic resonance spectrometer, J. Glaciol., 6, 89–100, 1966.

Richter, H.-P. and Bauer, A.: Ferromagnetic isolation of endosomes involved in vitellogenin transfer into *Xenopus* oocytes, Eur. J. Cell Biol., 51, 53–60, 1990.

Ritz, T., Adem, S., and Schulten, K.: A Model for Photoreceptor-Based Magnetoreception in Birds, Biophys. J., 78, 707–718, 2000.

Rogaev, E. I., Moliaka, Y. K., Malyarchuk, B. A., Kondrashov, F. A., Derenko, M. V., Chumakov, I., and Grigorenko, A. P.: Complete Mitochondrial Genome and Phylogeny of Pleistocene Mammoth *Mammuthus primigenus*, PLOS Biol., 4, e73, 2006.

Rosello, C., Ballet, P., Planus, E., and Tracqui, P.: Model driven quantification of individual and collective cell migration, Acta Biotheor, 52, 343–363, 2004.

Rosen, A. D.: Mechanism of action of moderate-intensity static magnetic fields on biological systems, Cell Biochem. Biophys., 39, 163–73, 2003.

Rothwell, W. and Vinegar, H.: Petrophysical applications of NMR imaging, Appl. Opt., 24, 3969–3972, 1985.

Rubinsky, B., Hong, J.-S., and Storey, K. B.: Freeze tolerance in turtles: visual analysis by microscopy and magnetic resonance imaging, Am. J. Physiol., 267, R1078–R1088, 1994a.

Rubinsky, B., Wong, S. T. S., Hong, J.-S, Gilbert, J., Roos, M., and Storey, K. B.: [1]H magnetic resonance imaging of freezing and thawing in freeze-tolerant frogs, Am. J. Physiol., 266, R1771–R1777, 1994b.

Sælen, G.: Diagenesis and construction of the belemnite rostrum, Palaeontol., 32, 765–798, 1989.

Sangster, J.: Octanol-water partition coefficients: fundamentals and physical chemistry,

Wiley, Chichester, 1997.

Sardet, C., Prodon, F., Dumollard, R., Chang, P., and Chênevert, J.: Structure and Function of the Egg Cortex from Oogenesis through Fertilization, Dev. Biol., 241, 1–23, 2002.

Sassen, K., Liou, K. N., Kinne, S., and Griffin, M.: Highly Supercooled Cirrus Cloud Water: Confirmation and Climatic Implications, Science, 227, 411–413, 1985.

Sattler, B., Puxbaum, H., and Psenner, R.: Bacterial growth in supercooled cloud droplets, Geophys. Res. Lett., 28, 239–242, 2001.

Schatten, G. and Donovan, P.: Embryology: plane talk, Nature, 430, 301–302, 2004.

Schenck, J. F.: Physical interactions of static magnetic fields with living tissues, Prog. Biophys. Mol. Biol., 87(2-3), 185–204, 2005.

Schmitt, S.: From eggs to fossils: epigenesis and transformation of species in Pander's biology, Int. J. Dev. Biol., 49, 1–8, 2005.

Schreiber, W. G., Teichmann, E. M., Schiffer, I., Hast, J., Akbari, W., Georgi, H., Graf, R., Hehn, M., Spiebeta, H. W., Thelen, M., Oesch, F., and Hengstler, J. G.: Lack of mutagenic and co-mutagenic effects of magnetic fields during magnetic resonance imaging, J. Magn. Reson. Imaging, 14, 779–788, 2001.

Schwarz, D., Vontobel, P., Lehmann, E. H., Meyer, C. A., and Bongartz, G.: Neutron Tomography of Internal Structures of Vertebrate Remains: A Comparison with X-ray Computed Tomography, Palaeontol. Electron., 8, 30A, 2005.

Schweitzer, M. H.: The Future of Molecular Biology, Palaeontol. Electron., 5, 2, 2003.

Schweitzer, M. H., Wittmeyer, J. L., Horner, J. R., and Toporski, J. K.: Soft-tissue vessels and cellular preservation in *Tyrannosaurus rex*, Science, 307, 2005.

Sebes, J. I., Langston, J. W., Gavant, M. L., and Rothschild, B. M.: Magnetic resonance imaging of growth recovery lines in fossil vertebrae, Amer. J. Roentgenol., 157, 415–416, 1991.

Sehy, J. V., Ackerman, J. J., and Neil, J. J.: Water and lipid MRI of the *Xenopus* oocyte, Magn. Reson. Med., 46, 900–906, 2001.

Sehy, J. V., Ackerman, J. J., and Neil, J. J.: Apparent diffusion of water, ions, and small molecules in the *Xenopus* oocyte is consistent with Brownian displacement, Magn. Reson. Med., 48, 42–51, 2002.

Sepich, D. S., Calmelet, C., Kiskowski, M., and Solnica-Krezel, L.: Initiation of convergence and extension movements of lateral mesoderm during zebrafish gastrulation, Dev. Dyn., 234, 279–292, 2005.

Shaw, J. M. and Jones, G. M.: Terminology associated with vitrification and other cryopreservation procedures for oocytes and embryos, Human Reprod. Update, 9, 583–605, 2003.

Shen, E. L. and Bogenhagen, D. F.: Developmentally-regulated packaging of mitochondrial DNA by the HMG-box protein mtTFA during *Xenopus* oogenesis, Nucleic Acids Res., 29, 2822–2828, 2001.

Shook, D. R. and Keller, R.: Mechanisms, mechanics and function of epithelial mesenchymal transitions in early development, Mech. Dev., 120, 1351–1383, 2003.

Shuster, C. B. and Burgess, D. R.: Targeted new membrane addition in the cleavage furrow is a late, separate event in cytokinesis, Proc. Natl. Acad. Sci. USA, 99, 3633–3638, 2002.

Sintich, S. M., Steinberg, J., Kozlowski, J. M., Lee, C., Pruden, S., Sayeed, S., and Sensibar, J. A.: Cytotoxic Sensitivity to Tumor Necrosis Factor-α in PC3 and LNCaP Prostatic Cancer Cells Is Regulated by Extracellular Levels of SGP-2 (Clustrin), The Prostate, 39, 87–93, 1999.

Siurek, J., Chevallier, P., Ro, C.-U., Chun, H. Y., Youn, H. S., Zięba, E., and a. Kuczumov: Studies on the wood tissue substitution by silica and calcites during the preservation of fossil wood, Journ. Alloys Compounds, 362, 107–115, 2004.

Sive, H. L., Grainger, R. M., and Harland, R. M.: Early Development of *Xenopus Laevis*: A laboratory manual, Cold Spring Harbor, New York, 2000.

Siveter, D. J., Sutton, M. D., Briggs, D. E. G., and Siveter, D. J.: A Silurian sea spider, Nature, 431, 978–980, 10.1038/nature02928, 2004.

Slichter, C. P.: Principles of Magnetic Resonance, Springer-Verlag, Berlin, Heidelberg, New York, 1978.

Smith, B. R.: Visualizing human embryos, Sci. Am., 280, 76–81, 1999.

Smith, B. R., Johnson, G. A., Groman, E. V., and E, E. L.: Magnetic resonance microsocopy of mouse embryos, Proc. Natl. Acad. Sci. USA, 91, 3530–3533, 1994.

Smith, K. K.: Time's arrow: heterochrony and the evolution of development, Int. J. Dev. Biol., 47, 613–621, 2003.

Smith, M. E. and Strange, J. H.: NMR techniques in materials physics: a review, Meas. Sci. Technol., 7, 449–475, 1996.

Solnica-Krezel, L.: Conserved patterns of cell movements during vertebrate gastrulation, Curr. Biol., 15, R213–R228, 2005.

Song, J. L. and Wessel, G. M.: How to make an egg: transcriptional regulation in oocytes, Differentiation, 73, 1–17, 2005.

Song, Y.-Q., Ryu, S., and Sen, P. N.: Determining multiple length scales in rocks, Nature, 406, 178–181, 2000.

Spegazzini, C.: Coniferales fósiles patagónicas, Ann. Soc. Cient. Argent. Buenos Aires, 98, 125–139, 1924.

Spiegler, D. and Gürs, K.: Der miozäne Glimmerton von Groß Pampau, Schleswig-Holstein (Mollusken, Foraminiferen und Bolboformen), Meyniana, 48, 135–164, 1996.

Spoor, F., Jeffery, N., and Zonneveld, F.: Imaging skeletal growth and evolution, in Development, Growth and Evolution: Implications for the Study of the Hominid Skeleton, edited by P. O'Higgins and M. Cohn, pp. 123–161, Academic Press, London, 2000.

Stockey, R. A.: Seeds and embryos of *Araucaria mirabilis*, Am. J. Bot., 62, 856–868, 1975.

Stockey, R. A.: Reproductive biology of the Cerro Cuadrado (Jurassic) fossil conifers: *Pararaucaria patagonica*, Am. J. Bot., 64, 733–744, 1977.

Stockey, R. A.: Reproductive biology of Cerro Cuadrado fossil conifers: ontogeny and reproductive strategies in *Araucaria mirabilis* (Spegazzini) Windhausen, Palaeontographica B, 166, 1–15, 1978.

Storey, J. M. and Storey, K. B.: Cold Hardiness and Freeze Tolerance, in Functional Metabolism: Regulation and Adaptation, edited by K. B. Storey, Wiley, Chichester, 2004a.

Storey, K. B. and Storey, J. M.: Metabolic depression in animals: transcriptional and translational control, Biol. Rev., 79, 207–233, 2004b.

Storey, K. B., Miceli, M., Butler, K. W., Smith, I. C. P., and Deslauriers, R.: ^{31}P NMR studies of the freeze-tolerant larvae of the gall fly, *Eurosta solidaginis*, Eur. J. Biochem., 142, 591–595, 1984.

Sutton, M. D., Briggs, D. E. G., Siveter, D. J., and Siveter, D. J.: Methodologies for the Visualization and Reconstruction of Three-dimensional Fossils from the Silurian Herefordshire Lagerstätte, Palaeontol. Electron., 4, 1, 2001.

Sutton, M. D., Briggs, D. E. G., Siveter, D. J., and Siveter, D. J.: Silurian brachiopods with soft-tissue preservation, Nature, 436, 1013–1015, 2005.

Szczepaniak, L. S., Babcock, E. E., Schick, F., Dobbins, R. L., Garg, A., Burns, J. D., McGarry, D. K., and Stein, D. T.: Measurement of intracellular triglyceride stores by ^{1}H spectroscopy: validation *in vivo*, Am. J. Physiol., 276, E977–E989, 1999.

Tabazadeh, A., Djikaev, Y. S., and Reiss, H.: Surface crystallization of supercooled water in clouds, Proc. Natl. Acad. Sci. USA, 99, 15 873–15 878, 2002.

Tasnádi-Kubacska, A.: Paläopathologie, VEB Gustav Fischer Verlag, Jena, 1962.

Territo, P. R. and Smits, A. W.: Whole-body composition of *Xenopus laevis* larvae: implications for lean body mass during development, J. Exp. Biol., 201, 1013–1022, 1998.

Thielecke, H., Impidjati, Zimmermann, H., and Fuhr, G. R.: Gentle cell handling with an ultra-slow Instrument: creep manipulation of cells, Microsyst. Technol., 11, 1230–1241, 2005.

Thompson, D. W.: On Growth and Form, Cambridge University Press, Cambridge, 1966 edition, 1917.

Tourte, M., Mignotte, F., and Mounolou, J. C.: Heterogeneous distribution and replication activity of mitochondria in *Xenopus laevis* oocytes, Eur. J. Cell Biol., 34, 171–178, 1984.

Tyszka, J. M., Ewald, A. J., Wallingford, J. B., and Fraser, S. E.: New tools for visualization and analysis of morphogenesis in spherical embryos, Dev. Dyn., 234, 974–983, 2005.

Ubbels, G. A., Hara, K., Koster, C. H., and Kirschner, M. W.: Evidence for a functional role of the cytoskeleton in determination of the dorsoventral axis in *Xenopus laevis* eggs, J. Embryol. Exp. Morphol., 77, 15–37, 1983.

Ueno, S., Harada, K., and Shiokawa, K.: The embryonic development of frogs under strong DC magnetic fields, IEEE Trans. Magn., 20, 1663–1665, 1984.

Ueno, S., Shiokawa, K., and Iwamoto, M.: Embryonic development of *Xenopus laevis* under static magnetic fields up to 6.34 T, J. Appl. Phys., 67, 5841–5843, 1990.

Ueno, S., Iwasaka, M., and Shiokawa, K.: Early embryonic development of frogs under intense magnetic fields up to 8 T, J. Appl. Phys., 75, 7165–7167, 1994.

Valentine, J. W. and Jablonski, D.: Morphological and developmental macroevolution: a paleontological perspective, Int. J. Dev. Biol., 47, 517–522, 2003.

Valentine, J. W., Jablonski, D., and Erwin, D. H.: Fossils, molecules and embryos: new perspectives on the Cambrian explosion, Development, 126, 851–859, 1999.

Valles Jr., J. M.: Model of magnetic field-induced mitotic apparatus reorientation in frog eggs, Biophys. J., 82, 1260–1265, 2002.

Valles Jr., J. M., Wasserman, S. R., Schweidenback, C., Edwardson, J., Denegre, J. M., and Mowry, K. L.: Processes that occur before second cleavage determine third cleavage orientation in *Xenopus*, Exp. Cell Res., 274, 112–118, 2002.

van Zijl, P. C., Moonen, C. T., Faustino, P., Pekar, J., J., Kaplan, O., and Cohen, J. S.: Complete separation of intracellular and extracellular information in NMR spectra of perfused cells by diffusion-weighted spectroscopy, Proc. Natl. Acad. Sci. USA, 88, 3228–3232, 1991.

Vandenbroucke, M.: Kerogen: from Types to Models of Chemical Structure, Oil Gas Sci. Technol. (Rev. IFP), 58, 243–269, 2003.

Vanni, S., Lagerholm, B. C., Otey, C., Taylor, D. L., and Lanni, F.: Internet-based image analysis quantifies contractile behavior of individual fibroblasts inside model tissue, Biophys. J., 84, 2715–2727, 2003.

Veizer, J.: Chemical diagenesis of belemnite shells and possible consequences of paleotemperature determinations, N. Jb. Geol. Paläont. Abh., 147, 91–111, 1974.

Verdier, C.: Rheological properties of living materials: from cells to tissues, J. Theor. Medicine, 5, 67–91, 2003.

Volke, F., Pampel, A., Hänsler, M., and Ullmann, G.: Proton MAS-NMR of a protein in a frozen aqueous solution, Chem. Phys. Lett., 262, 374–378, 1996.

Volodina, N., Denegre, J. M., and Mowry, K. L.: Apparent mitochondrial asymmetry in *Xenopus* eggs, Dev. Dyn., 226, 654–662, 2003.

von Boletzky, S. and Overath, H.: Shell fracture and repair in the cuttlefish *Sepia officinalis*, in La seiche, the cuttlefish, edited by E. Boucaud-Camou, pp. 69–78, Centre de Publications, Universit'e de Caen, Caen, 1989.

Waggoner, B.: Molecular palaeontology, Encycl. Life Sci., 12, 227–232, 2002.

Wang, F., Weaver, V. M., Petersen, O. W., Larabell, C. A., Dedhar, S., Briand, P., Lupu, R., and Bissell, M. J.: Reciprocal interactions between β1-integrin and epidermal growth factor receptor in three-dimensional basement membrane breast cultures: a different perspective in epithelial biology, Proc. Natl. Acad. Sci. USA, 95, 14 821–14 826, 1998.

Webb, A. G.: Microcoil nuclear magnetic resonance spectroscopy, J. Pharm. Biomed. Anal., 38, 892–903, 2005.

Weiner, S. and Dove, P. M.: An overview of biomineralization processes and the problem of the vital effect, in Biomineralization, edited by P. M. Dove, J. J. DeYoreo, and S. Weiner, pp. 1–29, Min. Soc. Am., Washington, 2003.

Weiner, S., Lowenstam, H. A., and Hood, L.: Characterization of 80-million-year-old mollusk shell proteins, Proc. Natl. Acad. Sci. U S A, 73, 2541–2545, 1976.

Wellard, R. M., Shehan, B. P., Craik, D. J., and Adam, W. R.: Factors affecting ^{133}Cs chemical shifts in erythrocytes from cesium-fed rats, J. Magn. Reson. B, 104, 276–279, 1994.

Westbroek, P., van der Meide, P. H., Wey-Kloppers, J. S. v., Sluis, R. J. v., de Leeuw, J. W., and de Jong, E. W.: Fossil macromolecules from cephalopod shells: characterization, immunological response and diagenesis, Paleobiol., 5, 151–167, 1979.

Westphal, H., Surholt, I., Kiesl, C., Thern, H. F., and Kruspe, T.: NMR Measurements in Carbonate Rocks: Problems and an Approach to a Solution, Pure Appl. Geophys., 162, 549–570, 2005.

Wettlaufer, J. S.: Ice surfaces: macroscopic effects of microscopic structure, Phil. Trans. R. Soc. Lond. A, 357, 3403–3425, 1999.

Weybright, P., Mills, K., Campbell, N., Cory, D. G., and Singers, S.: Gradient, high-resolution, magic angle spinning ^{1}H nuclear magnetic resonance spectroscopy of intact cells, Magn. Reson. Med., 39, 337–345, 1998.

Wieland, G. R.: The Cerro Cuadrado petrified forest, Publ. Carnegie Inst. Washington, 449, 180p., 1935.

Wignall, S. M., Deehan, R., Maresca, T. J., and Heald, R.: The condensin complex is required for proper spindle assembly and chromosome segregation in *Xenopus* egg extracts, J. Cell Biol., 161, 1041–1051, 2003.

Wind, R. A., Minard, K. R., Holtom, G. R., Majors, P. D., Ackerman, E. J., Colson, S. D., Cory, D. G., Daly, D. S., Ellis, P. D., Metting, N. F., Parkinson, C. I., Price, J. M., and Tang, X. W.: An integrated confocal and magnetic resonance microscope for cellular research, J. Magn. Reson., 147, 371–377, 2000.

Wolf, D. P., Nishihara, T., West, D. M., Wyrick, R. E., and Hedrick, J. L.: Isolation, physico-chemical properties, and macromolecular composition of the vitelline and fertilization envelopes from *Xenopus leavis* eggs, Biochemistry, 15, 3671–3678, 1976.

Xiao, S.: Mitotic topologies and mechanics of Neoproterozoic algae, Paleobiology, 28, 244–250, 2002.

Yurewicz, E. D., Oliphant, G., and Hedrick, J. L.: The macromolecular composition of *Xenopus laevis* egg jelly coat, Biochemistry, 14, 3101–3107, 1975.

Zachariassen, K. E. and Kristiansen, E.: Ice Nucleation and Antinucleation in Nature, Cryobiology, 41, 257–279, 2000.

Zelenka, P. S.: Regulation of cell adhesion and migration in lens development, Int. J. Dev.

Biol., 48, 857–865, 2004.

Zimmermann, H., Hillgärtner, M., Manz, B., Feilen, P., Brunnenmeier, F., Leinfelder, U., Weber, M., Cramer, H., Schneider, S., Hendrich, C., Volke, F., and Zimmermann, U.: Fabrication of homogeneously cross-linked, functional alginate microcapsules validated by NMR-, CLSM- and AFM-imaging, Biomaterials, 24, 2083–2096, 2003.

Zimmermann, H., Katsen, A. D., Ihmig, F. R., Durst, C. H. P., Shirley, S. G., and Fuhr, G. R.: First steps of an interdisciplinary approach towards miniaturised cryopreservation for cellular nanobiotechnology, IEEE Proc. Nanobiotechnol., 151, 134–138, 2004.

Zollikofer, C. P. E. and Ponce de Léon, M. S.: Tools for rapid prototyping in the biosciences, IEEE Comp. Graph. Appl., 15, 48–55, 1995.

Zollikofer, C. P. E. and Ponce de Léon, M. S.: Virtual Reconstruction: A Primer in Computer-Assisted Paleontology and Biomedicine, Wiley, New York, 2005.

Zollikofer, C. P. E., Ponce De León, M. S., Vandermeersch, B., and Lévêque, F.: Evidence for interpersonal violence in the St. Césaire Neanderthal, Proc. Natl. Acad. Sci. USA, 99, 6444–6448, 2002.

Appendix A. Publications related to this thesis

The work presented in this thesis has in part been described in research articles or manuscripts whose bibliographic data and abstracts will be given below. Asterisks indicate equal contributions.

Chapter 2

- Seung-Cheol Lee*, Jee-Hyun Cho*, Daniel Mietchen*, Young-Sook Kim, Kwan Soo Hong, Chulhyun Lee, Dongmin Kang, Ki Deok Park, Byong-Seok Choi & Chaejoon Cheong (2006), "Subcellular *in vivo* [1]H MR spectroscopy of *Xenopus laevis* oocytes", *Biophys. J.* **90**:1797-1803.

Abstract   In vivo magnetic resonance (MR) spectra are typically obtained from voxels whose spatial dimensions far exceed those of the cells they contain. This study was designed to evaluate the potential of localized MR spectroscopy to investigate subcellular phenomena. Using a high magnetic field and a home-built microscopy probe with large gradient field strengths, we achieved voxel sizes of $(180~\mu m)^3$. In the large oocytes of the frog *Xenopus laevis*, this was small enough to allow the recording of the first compartment-selective in vivo MR spectra from the animal and vegetal cytoplasm as well as the nucleus. The two cytoplasmic regions differed in their lipid contents and NMR lineshape characteristics – differences that are not detectable with whole-cell NMR techniques. In the nucleus, the signal appeared to be dominated by water, whereas other contributions were negligible. We also used localized spectroscopy to monitor the uptake of diminazene acturate, an antitrypanosomal agent, into compartments of a single living oocyte. The resulting spectra from the nucleus and cytoplasm revealed different uptake kinetics for the two components of the drug and demonstrate that MR technology is on the verge of becoming a tool for cell biology.
The article is available online via http://dx.doi.org/10.1529/biophysj.105.073502 .

- Seung-Cheol Lee*, Daniel Mietchen*, Jee-Hyun Cho, Cheol-Su Kim, Kwan Soo Hong, Chulhyun Lee, Dongmin Kang, Wontae Lee & Chaejoon Cheong (2006), "Longitudinal *in vivo* imaging studies of cell division and embryonic development in *Xenopus laevis* by MR microscopy" (submitted)

Abstract Magnetic Resonance Imaging (MRI) at microscopic resolution is demonstrated here as capable of monitoring developmental processes in dividing cells and embryos. Image series covering the entire embryonic development of *Xenopus laevis* from a zygote up to an early tadpole were obtained in vivo, providing the first completely non-invasive longitudinal imaging study of the entire embryonic development in individual frogs. The images clearly reveal internal details of cell cleavage until blastulation, of germ layer formation, of cell migration during gastrulation and of tissue formation during neurulation, thereby largely confirming previous histological and in vitro investigations of this model system and opening up the possibility to construct fate maps non-invasively. Furthermore, biomechanical parameters – such as nuclear separation velocity during cell division and acceleration of epibolic movement during gastrulation – were derived directly from MRI scans. These experiments demonstrate that the non-invasive MRI technique provides a unique opportunity for studying three-dimensional developmental dynamics in vivo.

Chapter 3

- Daniel Mietchen, Jörg Jakobi & Hans-Peter Richter (2005), "Cortex reorganization of *Xenopus laevis* eggs in strong static magnetic fields", *Biomagn. Res. Technol.* **3**: 2.

Abstract Observations of magnetic field effects on biological systems have often been contradictory. For amphibian eggs, a review of the available literature suggests that part of the discrepancies might be resolved by considering a previously neglected parameter for morphological alterations induced by magnetic fields – the jelly layers that normally surround the egg and are often removed in laboratory studies for easier cell handling. To experimentally test this hypothesis, we observed the morphology of fertilizable *Xenopus laevis* eggs with and without jelly coat that were subjected to static magnetic fields of up to 9.4 T for different periods of time. A complex reorganization of cortical pigmentation was found in dejellied eggs as a function of the magnetic field and the field exposure time. Initial pigment rearrangements could be observed at about 0.5 T, and less than 3 T are required for the effects to fully develop within two hours. No effect was observed when the jelly layers of the eggs were left intact. These results suggest that the action of magnetic fields

might involve cortical pigments or associated cytoskeletal structures normally held in place by the jelly layers and that the presence of the jelly layer should indeed be included in further studies of magnetic field effects in this system.

The article is available online via http://dx.doi.org/10.1186/1477-044X-3-2 .

- Daniel Mietchen, Jörg Jakobi & Hans-Peter Richter (2006), "Cleavage plane reorientation in *Xenopus laevis* oocytes – the jelly coat's perspective" (in preparation)

Abstract   Many magnetic field effects on many biological systems have been described. In amphibian eggs, these include cleavage plane alterations in embryos and pigment reorganization in unfertilized eggs. The latter, however, was found to occur exclusively if the jelly coat normally surounding the eggs had been removed. Here, we investigated whether the jelly plays a similar role in mediating magnetic field effects on fertilized *Xenopus* eggs and developing embryos subjected to static magnetic fields of up to 9.4 T during their first cleavage cycles. The previously reported cleavage plane orientation effect could successfully be reproduced in the magnet but also in controls only exposed to the geomagnetic field. Moreover, the effect could entirely be avoided if the jelly coat surrounding eggs and embryos was left intact, suggesting that the jelly coat is indirectly involved in cleavage plane determination by stabilizing cytoplasmic structures that govern the positioning of the mitotic apparatus, independent of magnetic fields up to 9.4 T.

Chapter 4

- Daniel Mietchen, Helmut Keupp, Bertram Manz & Frank Volke (2005), "Non-invasive diagnostics in fossils – Magnetic Resonance Imaging of pathological belemnites", *Biogeosciences* **2**:133-140.

Abstract   For more than a decade, Magnetic Resonance Imaging (MRI) has been routinely employed in clinical diagnostics because it allows non-invasive studies of anatomical structures and physiological processes *in vivo* and to differentiate between healthy and pathological states, particularly of soft tissue. Here, we demonstrate that MRI can likewise be applied to fossilized biological samples and help in elucidating paleopathological and paleoecological questions: Five anomalous guards of Jurassic and Cretaceous belemnites are presented along with putative paleopathological diagnoses directly derived from 3D MR images with microscopic resolution. *Syn vivo* deformities of both the mineralized internal rostrum and the surrounding former soft tissue can be traced back in part to traumatic events of predator-prey-interactions, and partly to parasitism. Besides, evidence is presented

that the frequently observed anomalous apical collar might be indicative of an inflammatory disease. These findings highlight the potential of Magnetic Resonance techniques for further paleontological applications.

The article is available online via http://direct.sref.org/1726-4189/bg/2005-2-133 .

- Daniel Mietchen, Martin Aberhan, Bertram Manz, Oliver Hampe, Barbara Mohr, Christian Neumann & Frank Volke (2006), "Three-dimensional Magnetic Resonance Imaging of fossils across taxa", (in preparation)

Abstract   The extent to which an organism is mineralised during its life time largely determines the visibility of its species in the fossil record. In addition to mineral structures, many fossils nonetheless contain residual water and traces of organic molecules, the analysis of which has become an integral part of current paleontological research. The methods available for such investigations, though, typically require dissolution or ionisation of the fossil sample or parts thereof, which is an issue with rare specimens. In such cases, a non-destructive technique like Magnetic Resonance Imaging (MRI) could, in principle, be very helpful but its potential for paleontological applications has never been systematically investigated. This study was thus undertaken to test whether ^{1}H MRI can be employed to generate three-dimensional representations of fossils of different taxonomic and diagenetic backgrounds non-invasively. MR image series were acquired from intact invertebrate, vertebrate and plant fossils from different deposits at pixel resolutions around 100 μm. They routinely reveal anatomical details and demonstrate that MRI can effectively complement existing approaches for paleontological investigations. Supplementary ^{1}H and ^{13}C Magnetic Resonance spectra acquired with the Magic Angle Spinning technique indicate that water accounts for most of the signal in the MR images.

Further publications

- The MRI part of another article was inspired by the work presented in Chapter 4 but not included there:

  Werner E. G. Müller, Oxana V. Kaluzhnaya, Sergey I. Belikov, Matthias Rothenberger, Heinz C. Schröder, Andreas Reiber, Jaap A. Kaandorp, Bertram Manz, Daniel Mietchen & Frank Volke (2006), "Magnetic Resonance Imaging of the siliceous skeleton of the demosponge *Lubomirskia baicalensis*", *J. Struct. Biol.* **153**: 31-41.

Abstract   The skeletal elements (spicules) of the demosponge *Lubomirskia baicalensis* were analyzed; they are composed of amorphous, noncrystalline silica, and contain in a central axial canal the axial filament which consists of the enzyme silicatein. The axial filament, that orients the spicule in its longitudinal axis exists also in the center of the spines which decorate the spicule. During growth of the sponge, new serially arranged modules which are formed from longitudinally arranged spicule bundles are added at the tip of the branches. X-ray analysis revealed that these serial modules are separated from each other by septate zones (annuli). We describe that the longitudinal bundles of spicules of a new module originate from the apex of the earlier module from where they protrude. A cross section through the oscular/apical-basal axis shows that the bundle rays are organized in a concentric and radiate pattern. High resolution magnetic resonance microimaging studies showed that the silica spheres of the spicules in the cone region contain high amounts of 'mobile' water. We conclude that the radiate accretive growth pattern of sponges is initiated in the apical region (cones) by newly growing spicules which are characterized by high amounts of 'mobile' water; subsequently spicule bundles are formed laterally around the cones.
The article is available online via http://dx.doi.org/10.1016/j.jsb.2005.09.008 .

- An article about the results of my diploma (M. Sc.) thesis was written up in part during my time at IBMT:
Daniel Mietchen*, Thomas Schnelle*, Torsten Müller, Rolf Hagedorn & Günter Fuhr (2002), "Automated dielectric single cell spectroscopy – temperature dependence of electrorotation", *J. Phys. D: Appl. Phys.* **35**:1258-1270.

Abstract   A theoretical framework is presented which allows, for the first time, quantitative statements about the temperature dependence of electrorotation (ER): while temperature changes in physiological ranges do not significantly alter the overall shape of the spectrum, all of the characteristic points of the spectra do shift, to varying extends, in both their field frequency and amplitude of rotation. To experimentally verify these predictions, we developed a device which allows for autonomous detection of rotation speed. It is based on the pinhole technique known as MOSPAD [1] but differs in its higher degree of automation, more robust algorithms for signal analysis, and the possible use of an adaptable virtual mask in the video-RAM instead of the solid one in the optical path. Our results are in good agreement with theory and suggest previous ER data without temperature control should be reconsidered. We describe conditions under which physical and physiological effects of temperature in and on cells can be distinguished. Moreover, we broaden the applications of ER from the traditional determination of (rather static)

cellular properties to kinetics of cellular processes, to the impact of optical tweezers on the temperature of cells in their focus, or to resonance characteristics of electrode chambers.

The article is available online via http://dx.doi.org/10.1088/0022-3727/35/11/324 .